PNNL-25537

Pacific Northwest
NATIONAL LABORATORY
Proudly Operated by Battelle Since 1965

CASS Ferrite and Grain Structure Relationship

July 2016

CO Ruud
P Ramuhalli
RM Meyer
AA Diaz
MT Anderson

Prepared for the U.S. Nuclear Regulatory Commission
under a Related Services Agreement with the U.S. Department of Energy
CONTRACT DE-AC05-76RL01830

U.S. DEPARTMENT OF ENERGY

DISCLAIMER

PACIFIC NORTHWEST NATIONAL LABORATORY
operated by
BATTELLE
for the
UNITED STATES DEPARTMENT OF ENERGY
under Contract DE-AC05-76RL01830

Printed in the United States of America

Available to DOE and DOE contractors from the
Office of Scientific and Technical Information,
P.O. Box 62, Oak Ridge, TN 37831-0062;
ph: (865) 576-8401
fax: (865) 576-5728
email: reports@adonis.osti.gov

Available to the public from the National Technical Information Service,
U.S. Department of Commerce, 5285 Port Royal Rd., Springfield, VA 22161
ph: (800) 553-6847
fax: (703) 605-6900
email: orders@ntis.fedworld.gov
online ordering: http://www.ntis.gov/ordering.htm


This document was printed on recycled paper.
(9/2003)

PNNL-25537

CASS Ferrite and Grain Structure Relationship

CO Ruud
P Ramuhalli
RM Meyer
AA Diaz
MT Anderson

July 2016

Prepared for
U.S. Nuclear Regulatory Commission
under a Related Services Agreement
with the U.S. Department of Energy
Contract DE-AC05-76RL01830

Pacific Northwest National Laboratory
Richland, Washington 99352

Summary

This document summarizes the results of research conducted at Pacific Northwest National Laboratory (PNNL) to determine whether, based on experimental measurements, a correlation existed between grain structure in cast austenitic stainless steel (CASS) piping and ferrite content of the casting alloy. The motivation for this research lies in the fact that ultrasonic testing (UT) is strongly influenced by CASS grain structure; knowledge of this grain structure may help improve the ability to interpret UT responses, thereby improving the overall reliability of UT inspections of CASS components.

UT inspection is commonly applied for in-service inspection of piping welds in the primary pressure boundary of light-water reactors, in line with the rules contained within the American Society of Mechanical Engineers Boiler and Pressure Vessel Code, Section XI. The purpose of the inspection is reliable detection and accurate sizing of service-induced degradation and/or material flaws introduced during fabrication.

However, the varied metallurgical microstructures of CASS piping and fittings, including statically cast stainless steel and centrifugally cast stainless steel, introduce significant variations in the propagation and attenuation of ultrasonic sound fields, which can impact the reliability of the inspection.

Previous review of the literature indicated that a correlation may exist between CASS microstructures and ferrite concentrations (delta ferrite content of the casting alloy). Ferrite can be measured in situ, nondestructively using electromagnetic induction technology. Also, x-ray fluorescence (XRF) may be used to nondestructively measure the elemental content of the pipe in situ; the measured elemental content may be applied to a mathematical model to calculate the ferrite content of the alloy. An electromagnetic induction–based instrument called a Feritscope and an XRF analyzer were used to conduct these tests.

At PNNL, a number of CASS specimens were readily available for these studies where grain structure had been characterized. Ferrite and elemental analysis were conducted on the outer diameter (OD) surface, inner diameter (ID) surface, and accessible through-wall sections of these specimens. The resulting data sets were analyzed to determine the correlation between ferrite content (measured and calculated) and CASS grain structure. The grain structure was quantified in terms of the percentage of columnar grains, and the sensitivity of any perceived correlation to a number of variables (such as changes in ferrite over the OD, ID, or through-thickness) examined. The analysis also incorporated the estimated measurement variability.

It was concluded that electromagnetic induction–based ferrite measurements were too sensitive to post-casting processing to reflect the as-cast ferrite content, and thus the grain structure of the CASS pipe. However, the elemental content of the pipe was not affected by post-casting processing and the ferrite content calculated from XRF elemental content showed a fair correlation to grain structure.

The correlations between grain structure as defined by percent columnar grains and ferrite content as calculated from XRF measurements of elemental content are just a first step towards the ultimate goal of improving the reliability of UT. The use of measurements on additional specimens is necessary to improve these correlations. Additionally, the metric used (percent columnar grains) does not adequately capture the volumetric variation of grain structure. Volumetric characterization approaches for grain structure (some of which may incorporate various ultrasonic measurements) will likely be necessary before the information on grain structure can be applied to improving the reliability of ultrasonic inspection methods.

Acknowledgments

The work described in this technical letter report was performed with funding from the U.S. Nuclear Regulatory Commission under U.S. Nuclear Regulatory Commission (NRC) Job Code Number V6323. Mr. Wallace Norris was the NRC Program Monitor at the time this work was conducted. The Pacific Northwest National Laboratory (PNNL) would like to thank Mr. Norris for his guidance and technical direction during this time. Ms. Carol Nove is the present Contracting Officer Representative for this Program, at the time of submission of this technical letter report and the authors would like to thank her for reviewing the technical content. The support of Ms. Kay Hass at PNNL for the final preparation of this report, as well as the thoughtful comments from the peer reviewers, is gratefully acknowledged. Finally, the authors would like to thank Bruker AXS for their support in performing the x-ray fluorescence measurements.

Acronyms and Abbreviations

ANL	Argonne National Laboratory
ASM	ASM International (formerly American Society for Materials)
ASME	American Society of Mechanical Engineers
CASS	cast austenitic stainless steel
CCSS	centrifugally cast stainless steel
HAZ	heat-affected zone
ID	inner diameter
ISI	in-service inspection
LWR	light-water reactor
MFC	mechanical fatigue crack
OD	outer diameter
PISC	Programme for the Inspection of Steel Components
PNNL	Pacific Northwest National Laboratory
PWR	pressurized water reactor
PWROG	Pressurized Water Reactor Owners Group
RT	radiographic testing
SAFT	Synthetic Aperture Focusing Technique
SCSS	statically cast stainless steel
S.D.	standard deviation
SFM	Sandusky Foundry and Machine
TFC	thermal fatigue crack
USP	U.S. Pipe
UT	ultrasonic
W_{CL}	weld centerline
WRSS	wrought stainless steel
XRF	x-ray fluorescence

Contents

Figures

Tables

1.0 Introduction

In-service inspection (ISI) requirements dictate that piping welds in the primary pressure boundary of light-water reactors (LWRs) be subject to a volumetric examination based on the rules contained within the American Society of Mechanical Engineers (ASME) Boiler and Pressure Vessel Code, Section XI. The volumetric examination may include radiographic testing (RT) or ultrasonic testing (UT), but local radiation environments and access limitations may prevent the use of the former. The purpose of the inspection is the reliable detection and accurate sizing of service-induced degradation and/or material flaws introduced during fabrication. However, the characteristic and varied metallurgical microstructures of cast austenitic stainless steel (CASS) piping and fittings, including statically cast stainless steel (SCSS) and centrifugally cast stainless steel (CCSS), introduce significant variations in the propagation and attenuation of ultrasonic sound fields. These variations complicate interpretation of the UT responses and compromise the reliability of UT inspection.

In an attempt to develop more accurate procedures for the UT inspection of primary pressure boundary LWR welds in CASS pipe, the Pacific Northwest National Laboratory (PNNL) investigated casting processes used by various foundries to produce piping and fittings (e.g., elbows) and compared the processes to grain structures. PNNL concluded that the grain structures in CCSS pipe and SCSS fittings cast by an individual foundry varied significantly in terms of grain type, grain size, and number of bands. More importantly, significant variation can also be found within a single heat. Thus, PNNL determined that no correlation between foundry, past foundry practice, or heat number and the grain structure could be established (Ruud et al. 2009).

However, a review of the literature indicated that a correlation may exist between the CASS microstructures and their associated ferrite concentrations, as delta ferrite content of the casting alloy. In particular, the propensity for the development of columnar grains in CASS pipe and components may be enhanced by low ferrite content of the casting alloy (Temple and Ogilvy 1992). Further, Chopra and Sather (1990) noted that the ferrite content is always lower toward the inner surface of CCSS pipe, apparently related to the higher nickel content of the existing liquidus and this may give rise to columnar grains.

An investigation was therefore undertaken to test these hypotheses, based on experimental measurements of ferrite and elemental content in CASS specimens with known microstructures. This report presents the results of this investigation, and is organized as follows:

- Section 2 presents background information on casting of CASS components, CASS inspection concerns, the objective of this investigation, grain structure of CASS components used in the current fleet of LWRs, and nondestructive examination techniques for the measurement of ferrite and elemental composition.
- Section 3 describes the specimen sets, experimental procedures, and the resulting measurements.
- Section 4 discusses the results from these experiments.
- Section 5 draws conclusions based on these results.
- Section 6 identifies potential areas for further investigation.

2.0 Background and Objective

2.1 Delta Ferrite in CASS

The use of UT for ISI of CASS components in operating nuclear power plants is difficult, primarily due to the adverse impact of the complex microstructure on the propagating ultrasonic wave. The acoustically anisotropic, coarse-grained microstructure in most CASS materials results in phenomena such as beam redirection and splitting, and attenuation due to scattering at the grain boundaries. It has been hypothesized that knowledge of the grain structure can potentially be used to optimize the ultrasonic inspection properties (such as phased-array focusing laws) to improve detection of flaws.

A potential approach to characterizing the grain structure is through measurements of ferrite content in the CASS. Elemental iron crystallizes in two types of ferrite phases and both are body-centered-cubic and ferromagnetic below 1418°F (Figure 2.1). Delta-ferrite crystallizes from molten iron and under slow cooling transforms to face-centered-cubic austenite beginning at 2541°F. Then the austenite transforms to alpha ferrite beginning at 1674°F and is stable at lower temperatures. Delta and alpha ferrite are indistinguishable by magnetic measurements, thus they are referred to as ferrite in this report. These phase designations are also used for alloyed iron; that is, steel, even though alloying elements such as nickel and chromium can significantly change the temperature range of stability of the ferrite and austenite phases. For example, nickel can stabilize austenite to well below ambient temperature so that it does not transform to alpha ferrite. Thus, the delta ferrite that is referred to in CASS is that ferrite formed from the molten metal upon solidification. Due to the nickel content of CASS, it is not likely that any alpha ferrite will be present in these alloys.

Temple and Ogilvy (1992) implied that low ferrite content would promote columnar grains while high ferrite content would promote equiaxed structure (Ruud et al. 2009). Massoud et al. (1998) wrote that slow cooling after casting promoted transformation of delta ferrite to gamma austenite. Because CASS products have a relatively low dislocation density, heat treatment will have little or no effect on the grain structure.

According to Hammar and Svensson (1979), “Austenitic stainless steels often have a duplex as-cast structure incorporating a greater or lesser amount of delta-ferrite. The proportion of delta-ferrite is primarily determined by segregation of the alloying elements during solidification and cooling.” Further, “In austenitic weld deposits a certain ferrite content, between 0 and 6%, depending on grade, can help to prevent hot cracking.” Also, “Austenitic stainless steels can freeze with primary precipitation of ferrite or austenite. These steels can be given a full austenitic structure after a homogenization annealing in the 1000–1300C range.” They concluded the mode of solidification of austenitic stainless steels can be predicted by calculating the Cr and Ni equivalents according to a method they describe, and if the function (Ni equivalent − 0.75 Cr equivalent + 0.257) is less than zero the steel will solidify ferritically, if equal to zero, ferrite and austenite will be simultaneously solidified, and if greater than zero, the steel will solidify austenitically. Hammar and Svensson calculated the Ni equivalent as 22C+0.31Mn−0.75Cr+1.0Ni−1.03Mo+14.2N, and the Cr equivalent as 1.0Cr+1.37Mo. Figure 2.1 shows a portion of the phase diagram of the very low carbon Fe-Cr-Ni diagram of 18% Cr illustrating the phases which may develop in the 200 to 1800°C temperature range.

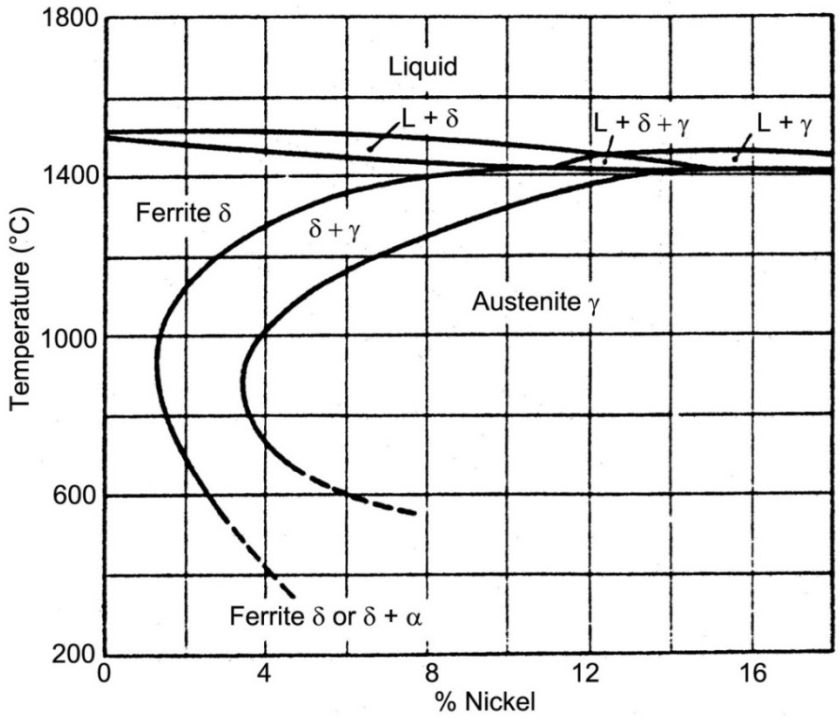

Figure 2.1. Vertical Section of Very Low Carbon Fe-Cr-Ni Diagram at 18% Chromium (Lundin and Chou 1983). Copyrighted image reprinted with the permission of The Welding Research Council, Inc., www.forengineers.org.

Temple and Ogilvy (1992) hypothesized a correlation between ferrite content and grain structure in dual-phase austenitic stainless steel pipe and components. In their Introduction under A1.1 Sizewell pressurized water reactor (PWR) pump bowl, they provided an example of a casting and described its grain structure as follows:

> "The pump bowls for the Sizewell B PWR are made from ASME SA351 Grade CF3 stainless steel with the specifications that the castings should contain between 12% and 25% delta ferrite. At the higher ferrite content, a pump bowl casting is likely to consist of an outer layer columnar region and an inner region of equiaxed grains whereas the lower ferrite content is likely to yield a totally columnar grain structure. The grain size increased with a slower rate of cooling. It is the ratio of nickel equivalent to chromium equivalent which controls the grain structure-in the case of low nickel content the delta ferrite solidifies from the molten material and there is a solid state transformation to austenite at a relative low temperature. In the case of higher nickel content, the austenite solidifies at a high temperature and the large columnar grains grow along the direction of the heat flow."

Further, according to ASM (ASM 1992, p. 298), "In the case of steels (including CASS) that solidify as ferrite, the columnar areas (structure) may be non-existent if superheat and mold wash thickness are low. In steels that solidify as austenite, it is relatively easy to obtain well-oriented 100% columnar structures (grains)."

In the Ruud et al. (2009) investigation, two CASS heats were identified from which the ferrite content was calculated using the elemental composition obtained from the ladle analysis; these were PWR Owner's Group (PWROG) heat number 156529 (CCSS) by Sandusky and PWROG heat number 28594-3 (SCSS) by ESCO (Diaz et al. 2007). Also, the composition and ferrite content for one SCSS and four

CCSS Argonne National Laboratory (ANL) specimens, as well as a description of the grain structure (but no photo micrographs), were reported by Chopra and Chung (1985) and Chopra (1991). These data seemed to support the opinion of Temple and Ogilvy (1992); that is, the ferrite content and grain structure in the observed (PWROG) or described (ANL) specimens showed that as the ferrite content (calculated from ladle analysis) increased, there was a reduced tendency toward columnar grains. Nevertheless, data from seven specimens (PWROG and ANL) are not statistically sufficient to support the hypothesis.

2.2 Objective

The objective of this investigation was to (1) measure the ferrite content on the outer diameter (OD), inner diameter (ID), and accessible through-wall cross-section surfaces on CASS pipe specimens (primarily CCSS) available at PNNL for which grain structure information was available in the form of micrographs; and (2) determine if a correlation between ferrite content and grain structure could be established. The ferrite content was determined by electromagnetic induction–based measurements and calculations using x-ray fluorescence (XRF) elemental analysis.

As discussed in Ruud et al. (2009), the casting process for CASS materials results in a range of microstructures, with differing levels of ferrite content. Based on other studies (Temple and Ogilvy 1992), the hypothesis is that equiaxed microstructures will, in general, have higher ferrite content, though the ferrite content may vary somewhat over the thickness of the specimen.

In addition to the ferrite measurements, determination of the elemental composition of these same specimens can provide an additional parameter, because this composition can be used to calculate the ferrite level. Further, according to ASM (ASM 1992, p. 298), "The as-cast structures obtained in horizontal centrifugal casting of steels vary according to composition." Thus, elemental composition of the surface of an as-cast structure, in itself, may provide a clue to the grain structure. Note that CASS structures are initially in an as-cast condition and have typically not been subjected to plastic deformation; therefore, their grain structure cannot generally be changed by thermal treatments. However, their phase structure, for example ferrite and austenite content, can be modified by thermal treatments. Thus, several parameters can potentially be obtained from each CASS specimen—delta ferrite (measured), elemental composition, delta ferrite (calculated from the elemental composition), and microstructure and grain size. These parameters can then be used to test the hypothesis posited by Temple and Ogilvy (1992), Chopra (1991), and Chopra and Chung (1985), and perhaps lead to a technique to predict the grain structure in existing LWR piping that might provide for improved UT inspection of welds.

At PNNL, a number of CASS specimens were readily available for these studies where grain structure had been characterized. The ferrite content of these specimens may be measured using instruments such as the Feritscope, and compared with the grain structure. XRF methods offer a relatively simple way of measuring the elemental composition. The principles behind these methods are described in the next section.

2.3 Electromagnetic Measurements

The Feritscope measures magnetic permeability, which is defined as the ratio of magnetic induction to magnetic field strength. Ferrite measurements using this technique require that a magnetic field be induced in the specimen and the resulting field strength be measured to establish the permeability. This may be accomplished by using a coil, such as that shown in Figure 2.2. The coil, excited with an alternating current at a specific frequency, is used to induce eddy currents, in accordance with Lenz's law (ASNT 2004), in the specimen under test. The corresponding induced magnetic flux density changes the net magnetic flux linked with the coil, resulting in a change in its inductance. At the same time, losses due

to the induced currents in the specimen manifest themselves as an increase in the resistance of the coil. Thus, the coil will present a change in electrical impedance (relative to its impedance in air) when placed near a conducting specimen.

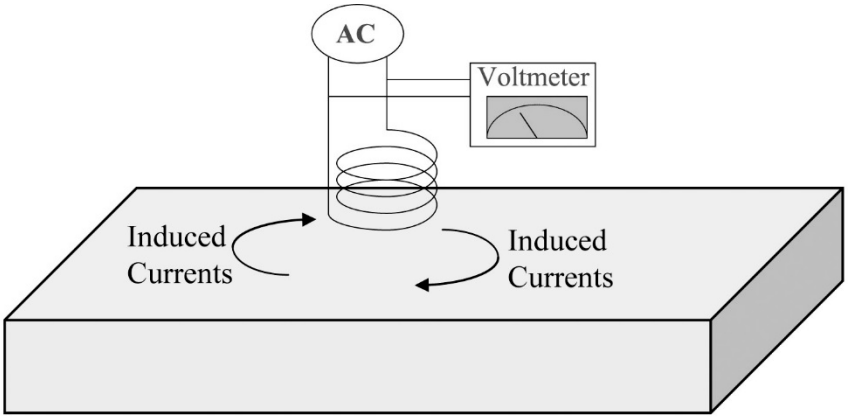

Figure 2.2. Schematic Illustrating Electromagnetic Measurement of Ferrite Content in CASS Specimens

Differences arise between the impedance measurements over ferromagnetic and non-ferromagnetic specimens. In the case of non-ferromagnetic specimens, the presence of the specimen (and therefore the induced currents) results in a decrease in the inductance with an increase in the resistance. However, for ferromagnetic specimens, the inductance typically increases as well (ASNT 2004). In particular, the increase is mostly linear with an increase in magnetic permeability. This forms the basis for most permeability measurement systems as well as for instruments that measure ferrite levels using magnetic permeability variations.

Three other factors (besides the permeability) also play a role in determining the impedance response in ferromagnetic specimens. These factors are the conductivity, probe liftoff, and frequency. Figure 2.3 shows the direction of change in the impedance due to increasing liftoff. For ferromagnetic specimens, this is seen to be in the direction opposite that of increasing permeability. Increasing conductivity also generally results in an increase in the response. Finally, for constant permeability, liftoff, and conductivity, the effect of changing frequency is to rotate the signal.

As the excitation frequency increases, the skin depth (or standard depth of penetration of the induced eddy currents) decreases (ASNT 2004). The standard depth of penetration is defined as

$$\delta = \sqrt{\frac{1}{\pi f \mu \sigma}} \tag{2.1}$$

where f is the excitation frequency, μ is the permeability of the material and σ is the conductivity. For non-ferritic steel, the skin depth at 1 kHz is about 13.1 mm (0.52 in.). In CASS materials, the ferrite content may vary somewhat over the thickness of the specimen. Thus, the permeability will also vary, according to microstructure and casting processes, with location within the specimen, and in general, is not known a priori. Thus, quantifying the exact skin depth in CASS components is difficult.

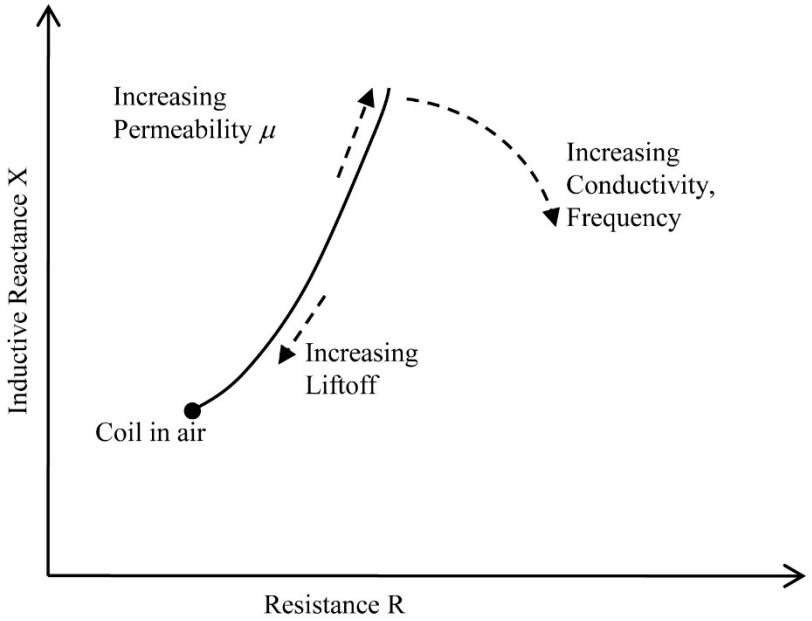

Figure 2.3. Impedance Trajectory Changes in Ferromagnetic Materials as a Function of Permeability Liftoff, Conductivity, and Frequency

2.4 Elemental Composition Using X-ray Fluorescence Spectroscopy

XRF spectroscopy makes use of the characteristic radiation fluoresced from each element to determine elemental composition of materials. Incident radiation, if it contains sufficient energy, results in the ejection of electrons from their orbital shells (Verma 2007). Typically, high energy x-rays are used for incident radiation, although gamma rays may also be used. Electrons in other orbital shells move to fill the resulting vacancy, and in the process, produce secondary x-ray radiation (x-ray fluorescence). The energy in this secondary (or characteristic) radiation varies depending on the element. For instance, carbon has lower secondary emission energy than chromium. By measuring the energy in the secondary radiation, the elements making up the material can be identified. Figure 2.4 shows an example of the XRF spectrum for a stainless steel specimen, and clearly shows the energy peaks corresponding to chromium, iron, and nickel.

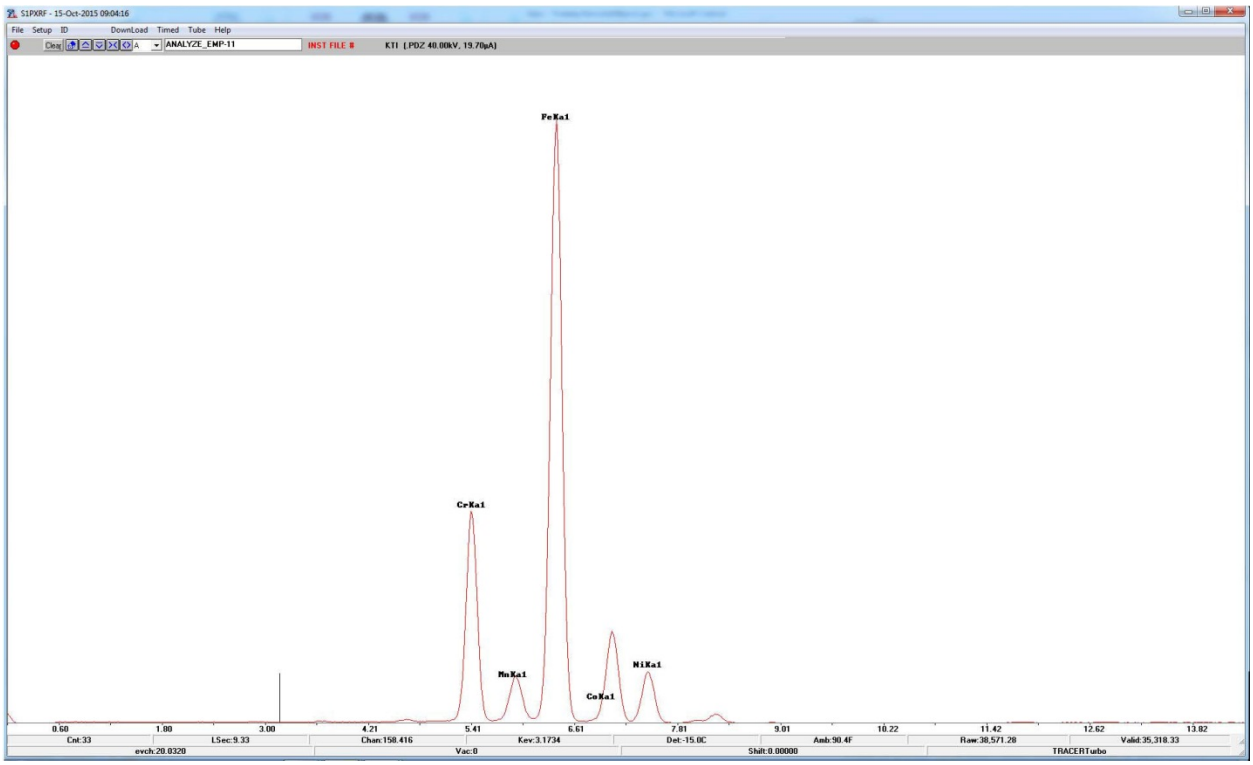

Figure 2.4. X-ray Fluorescence Spectrum for Stainless Steel Specimen

3.0 Specimens, Experimental Procedures and Results

3.1 Specimens

Seventeen different specimens of centrifugally cast stainless steel (CCSS) were identified from an assortment of CASS specimens available at PNNL. Three specimens, B-510, B-516, and B-527, had been previously used in PNNL studies as well as for Action 4 of the Programme for the Inspection of Steel Components III (PISC-III). In addition, CCSS piping sections that were part of eight PWROG specimens were included in the studies. These specimens were designated as APE-1, MPE-06, OPE-2, ONP-D-5, ONP-D-2, ONP-3-5, ONP-3-8, and OPE-5. Six other CCSS specimens were included in the studies. These specimens were a spool-piece each from IHI Southwest, a spool-piece from Westinghouse, a ring specimen cast by Manoir foundry in France, and three legacy specimens used in Synthetic Aperture Focusing Technique [SAFT] developmental studies at the University of Michigan. In this report, the three legacy specimens are labeled UMich-1, UMich-2, and UMich-3.

3.1.1 PWR Owners Group Specimens

A set of eight specimens were selected from the PWROG traveling specimen set (Anderson et al. 2007). Each specimen consists of a CCSS pipe section welded to a statically cast (SCSS) or wrought stainless steel (WRSS) section. Specimen dimensions vary, but were typically between 6 cm and 8 cm (2.4 in. and 3.2 in., respectively) thick and were nominally 260 mm (10.2 in.) circumferential segments with 610 mm (24 in.) axial extents. Circumferentially oriented surface-breaking thermal and mechanical fatigue cracks (TFC or MFC, respectively) were located in the weld region near the weld root with reported depths of 13 to 42 percent through-wall. In addition, inside/outside surface geometrical conditions, such as a counterbore at the ID and OD mismatch, were also present to represent typical primary piping configurations in PWR nuclear power plants. However, for the purposes of microstructure characterization, measurements were made on the CCSS base material, far from the weld to avoid having the weld microstructure and implanted flaws impact the measurements.

The CCSS pipe used in specimens APE-1 and MPE-6 was from heat Sandusky Foundry and Machine (SFM) 156527 and the CCSS pipe in specimens ONP-D-2, ONP-D-5, ONP-3-5, and ONP-3-8 were from heat SFM 156361. The CCSS pipe in specimens OPE-2 and OPE-5 was from U. S. Pipe (USP) heat number C2291A. The microstructural data are listed in Ruud et al. (2009, Table 4.4). The ladle elemental chemistry of SFM 156529 is shown in Ruud et al. (2009, page J.3); that of USP C2291A was not available.

The microstructure of these specimens varied. All CCSS sections were coarse-grained, with mixed or banded microstructures. The SCSS sections had generally coarse-grained mixed microstructures as well, while the WRSS sections were fine-grained. Average grain sizes varied with specimen, although 1 to 6 mm (0.04 to 0.24 in.) grains are typical for equiaxed grains in the CCSS sections (Ruud et al. 2009). Figure 3.1 shows an example of the coarse-grained microstructure of a PWROG specimen, where an attempt has been made to color-highlight various bands of grains/orientations for easier visual discrimination.

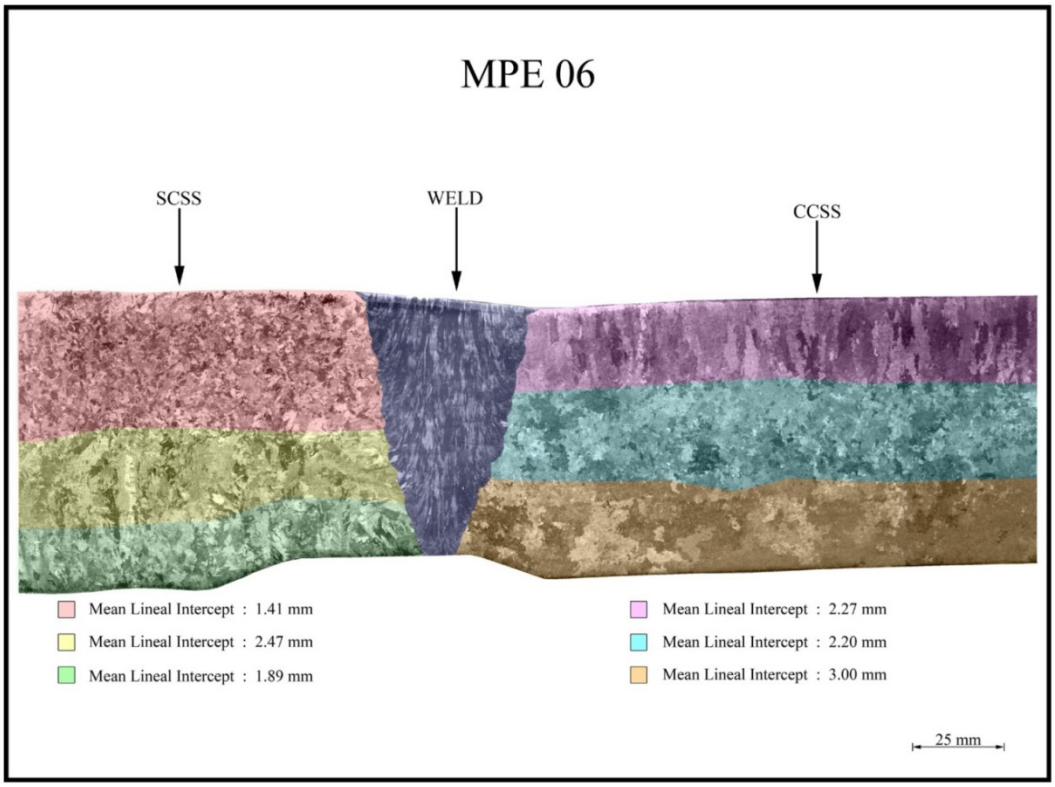

Figure 3.1. Example of Microstructure of a PWROG Specimen

3.1.2 PISC-III Specimens

The three PISC-III specimens consisted of two pipe sections, one of equiaxed-grain and the other columnar-grain material (Figure 3.2) joined with a circumferential girth weld. A stamped label of B-510, B-516, or B-527 uniquely identified each specimen. Typical axial, radial, and circumferential arc length dimensions of a specimen were 40 cm (1.6 in.), 5.9 cm (0.23 in.), and 18 cm (0.7 in.), respectively. Pipe wall thickness of the columnar material typically ranged between 59.9 mm (2.4 in.) and 60.5 mm (2.4 in.), while that of the equiaxed material typically ranged between 57.7 mm (2.3 in.) and 57.9 mm (2.3 in.). Figure 3.2 shows an example of the microstructure from one PISC-III specimen. The equiaxed CCSS grains on the left have a mean lineal intercept of 2.34 mm (0.09 in.) and the columnar CCSS grains on the right have a mean lineal intercept of 2.48 mm (0.097 in.) in the short dimension of the column. The mean lineal intercept is the average length of a line segment that crosses a sufficiently large number of grains. It is proportional to the equivalent diameter of a spherical grain (Steele and McCall 1984).

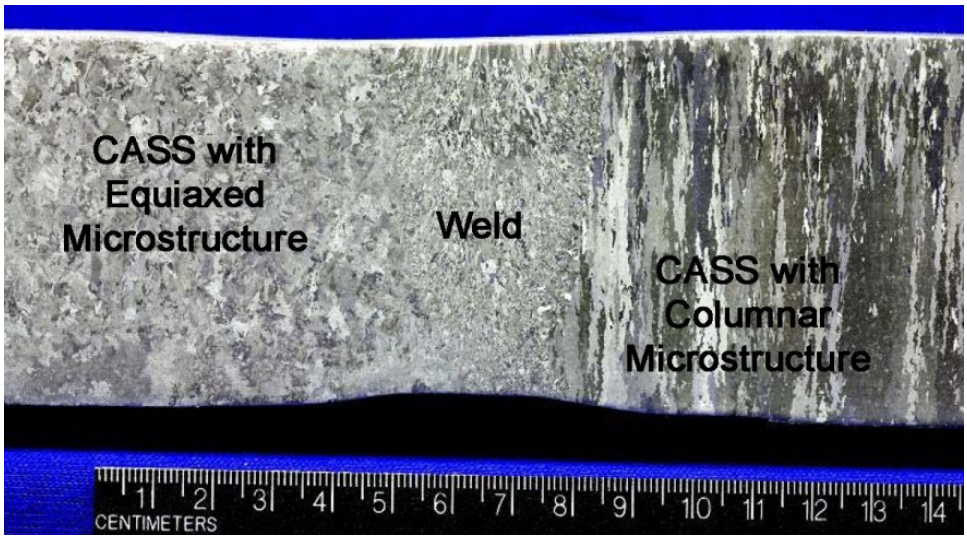

Figure 3.2. A Representative Axial-Radial Cross Section of a PISC-III CCSS Specimen, Showing Typical Outside and Inside Diameter Geometry, and Microstructure of a Specimen

3.1.3 Other/Miscellaneous Specimens

A number of other specimens were also used for the measurements obtained in this study, and are described in this section. The first of these was a piping segment loaned to PNNL by IHI Southwest Technologies. This piping segment is 15.24 cm (6 in.) in axial extent by 127 cm (50 in.) in circumferential extent. The segment has an 8.4 cm (3.3 in.) wall thickness and is approximately 91 cm (36 in.) in outside diameter. It consists of a coarse-grained, mixed, and banded microstructure and had some surface defects, sawcuts, and notches machined into the specimen but no fabricated or implanted cracks. This material contains a wide range of grain sizes and structures, with significant banding (Anderson et al. 2007) and variation of grain types as a function of circumferential location.

The next specimen is on loan from Westinghouse, Inc. The Westinghouse segment is 25.4 cm (10 in.) in axial extent by 130 cm (51 in.) in circumferential length, with a 6.4 cm (2.5 in.) wall thickness and an approximately 71 cm (28 in.) outside diameter. This specimen exhibits a coarse-grained, dendritic (columnar) microstructure with a banding condition evident as well (Anderson et al. 2007). The specimen contains some minor surface defects, sawcuts, and small notches machined into the surface but no fabricated or implanted cracks.

Another set of specimens labeled University of Michigan or UMich-1, -2 and -3 in this report are also welded legacy CCSS piping sections. These specimens were likely part of a set of specimens that were used in the early 1980s to develop SAFT signal processing algorithms for post-processing of ultrasonic inspection data on cast specimens. The specimens are 45.5 cm (17.9 in.) in axial extent, with a wall thickness of 6.1 cm (2.4 in.). The outside diameter for the three specimens varies, from about 60 cm (24 in.) for UMich-1 to about 36 cm (14 in.) for the other two specimens. The circumferential arc length of the specimens also varies from about 30 cm (12 in.) (UMich-3) to about 48 cm (19 in.) (UMich-1).

The last specimen was a CASS pipe section obtained from Manoir foundry in France. The outer and inner surfaces of this Manoir ring have been machined smooth leaving the ring with OD and ID dimensions of 93.7 cm by 78.7 cm (36.9 in. by 31 in.), respectively. Thus, the wall thickness of this specimen is 7.5 cm (2.94 in.).

3.1.4 Casting Processes, Elemental Composition and Delta Ferrite

As described previously, elemental composition, used in calculation of delta ferrite levels in CASS steels, may be estimated using ladle analysis, which is typically available as part of the heat number documentation. Given the vintage nature of the specimens used in this study, only three foundries and heat numbers, excluding SFM 144179, of CCSS pipe could be associated specifically with the CCSS specimens previously mentioned (Table 3.1). In addition, two foundries/heat numbers for SCSS elbows could be associated with some of these specimens. These were: ESCO elbow heat number 28594-3 incorporated in specimens APE-1 and MPE-6, and ESCO heat number 72176-1 incorporated as the elbow in OPE-2. Note that heat number SFM 144179 was incorporated in either the columnar or equiaxed side of the PISC-III specimens B-510, B-516, and B-527. However, documentation as to which side was lacking.

Table 3.1. Foundry and Heat Number for CCSS Pipe Sections Used in Delta Ferrite Study

Foundry/Heat	Heat Number	Specimens
SFM	156529	APE-1, MPE-6
SFM	156361	ONP-D-2, ONP-D-5, ONP-3-5, ONP-3-8
US Pipe	C2291A	OPE-2, OPE-5
SFM	144179[(a)]	B-510, B-516, B-527
Unknown		IHI Southwest (formerly Southwest Research Institute, SwRI) spool piece
Unknown		Westinghouse spool piece
Unknown[(b)]		UMich-1, UMich-2, UMich-3
Manoir Industries		Manoir piping section (MCC1)

(a) SFM heat number 144179 was incorporated in specimens B-510, B-516, and B-527 as either the equiaxed or columnar grain CCSS pipe but documentation clearly identifying the grain structure of the heat was not found (Ruud et al. 2009, page 4.37, paragraph 3).
(b) The specimens are most likely from SFM, with a heat number 152165, based on stamped markings on the specimens.

Calculations based on Hammar and Svensson (1979) for heats SFM 156529 and 144179 as well as ESCO 28594-3 (associated with the SCSS elbow sections on the PWROG specimens) show that the specimens associated with these heats would be predicted to freeze (solidify) ferritically. Note that specimens studied herein likely received a post-casting heat treatment to restore some of the delta ferrite that had transformed during slow cooling after solidification.

While not all of these specimens have available elemental composition documented (ladle analysis), those that are available are documented in Table 3.2 (Ruud et al. 2009, Table J.1). Also included are specimens that are important in the literature but not available at PNNL for this study.

Table 3.2. Ferrite Calculations from Ladle Analysis of Selected Specimens from Table 4.4 of Ruud et al. (2009)

Specimen	C	Mn	Si	P	S	Cr	Ni	Mo[(a)]	N[(a)]	Cr_e	Ni_e	Cr_e/Ni_e	$\%Fe_1$	$\%Fe_2$	%Fe Rprt[(b)]
APE-1, MPE-6 CCSS	0.05	0.66	1.1	0.032	0.02	20.0	8.3	0.5	0.04	16.14	13.10	1.257	18.1		
side (PWROG) -	0.05	0.66	1.1	0.032	0.02	20.0	8.3	0.5	0.04	16.66	12.38	1.35		18.3	
Ht.156529 by SFM															
APE-1, MPE-6 SCSS	0.03	0.86	1.2	0.02	0.007	20.03	8.66	0.5	0.04	15.62	12.25	1.27	19.6		
side (PWROG) -	0.03	0.86	1.2	0.02	0.007	20.03	8.66	0.5	0.04	16.84	12.24	1.38		19.6	
Ht.28594-3 by ESCO															
#23 ANL C1 by ESCO	0.039	1.22	1.18	0.033	0.008	19.0	9.37	0.65	0.04	15.36	13.95	1.10	7.84		7.8
	0.039	1.22	1.18	0.033	0.008	19.0	9.37	0.65	0.04	16.69	14.44	1.16		8.43	2.2
#24 ANL P1 by ESCO	0.036	0.59	1.12	0.026	0.013	20.49	8.1	0.04	0.036	16.09	12.48	1.29	20.8		17.7
	0.036	0.59	1.12	0.026	0.013	20.49	8.1	0.04	0.036	17.24	12.66	1.36		19.2	24.1
#25 ANL P2 by FAM	0.019	0.74	0.94	0.019	0.005	20.20	9.38	0.16	0.04	15.85	13.43	1.18	12.5		12.5
	0.019	0.74	0.94	0.019	0.005	20.20	9.38	0.16	0.04	16.84	13.61	1.24		12.1	15.6
#26 ANL P3 by SFM	0.021	1.06	0.88	0.017	0.014	18.89	8.45	0.01	0.168	14.33	14.93	0.96	2.76		2.8
	0.021	1.06	0.88	0.017	0.014	18.89	8.45	0.01	0.168	15.23	16.23	0.94		2.1	1.9
#27 ANL P4 by SFM	0.04	1.07	1.02	0.019	0.015	19.64	10.0	2.05	0.151	17.62	16.64	1.06	5.92		5.9
	0.04	1.07	1.02	0.019	0.015	19.64	10.0	2.05	0.151	19.05	17.91	1.06		5.1	10.0
PNNL CCSS-RRT	0.06	0.68	1.17	0.02	0.02	20.42	8.58	0.5	0.04	15.99	12.89	1.24	16.8		
(PISC-III Specimens)	0.60	0.68	1.17	0.02	0.02	20.42	8.58	0.5	0.04	17.19	12.97	1.33		17	17.4
Ht 144179 by SFM															

NOTE: The top set of numbers in each "row" indicates results for Model #1; the bottom set of numbers in each "row" indicates Model #2 results.

#1 Model for predicting ferrite content according to Aubrey et al. (1982): Cr equivalent = Cr_e = %Cr + 1.21 %Mo + 0.48 %Si - 4.99 and Ni equivalent = Ni_e = %Ni + 0.11 %Mn - 0.0086 $\%Mn^2$ + 18.4 %N + 24.5 %C + 2.77. Ferrite Content = $\%Fe_1 = 100.3 \times (Cr_e/Ni_e)^2 - 170.72\ (Cr_e/Ni_e) + 74.22$. Note these equations are based upon Hull's equivalent factors (Aubrey et al. 1982).

#2 Model for predicting ferrite content according to Aubrey et al. (1982): Cr equivalent = Cr_e= %Cr + 1.4 %Mo + 1.5 %Si - 4.99 and Ni equivalent = Ni_e = %Ni + 30 %C + 0.5%Mn + 26(%N - 0.02) + 2.77. Ferrite Content = $\%Fe_2 = 55.84 \times (Cr_e/Ni_e)^2 - 87.87\ (Cr_e/Ni_e) + 35.39$.

(a) Values of Mo and N were assumed to be 0.5 and 0.04 where chemistry data for these elements were not available (EPRI 1991).

(b) The top row of numbers in % Fe Rprt is the percent ferrite calculated and reported in Chopra et al. (1991). The bottom row of numbers in % Fe Rprt is the measured percent ferrite reported by the foundry. For Specimens #23 through #27, the measured values are also reported in Chopra et al. (1991).

NOTE: Chemistry from Chopra et al. (1991).

Table 3.2 also shows the reported and calculated levels of delta ferrite. The calculated levels are based on statistical models developed by Aubrey et al. (1982) to compute the ferrite content in CF-type stainless steels based upon elemental content. Their model (#1) for predicting ferrite content is:

$$\text{Cr equivalent} = Cr_e = \%Cr + 1.21\ \%Mo + 0.48\ \%Si - 4.99$$

$$\text{Ni equivalent} = Ni_e = \%Ni + 0.11\ \%Mn - 0.0086\ \%Mn^2 + 18.4\ \%N + 24.5\ \%C + 2.77$$

$$\text{Ferrite Content} = \%Fe_1 = 100.3 \times (Cr_e/Ni_e)^2 - 170.72\ (Cr_e/Ni_e) + 74.22$$

Note these equations are based upon Hull's equivalent factors (Aubrey et al. 1982). Further, the calculations are based on the assumption that the CASS has undergone post-casting heat treatment around 1000°C (1850°F) followed by a rapid cooling (Massoud et al. 1998). Such heat treatment is in consideration that the cooling rate between 900°C and 600°C (1650°F and 1110°F) during the casting process may have been sufficiently slow that some delta ferrite transformed to austenite as well as a brittle sigma phase (sigma phase not shown in phase diagram). The sigma phase may result in a degradation of mechanical properties and M23C6 carbides precipitated at the delta/gamma interfaces.

3.2 Ferrite Measurements Using Feritscope FMP30

A Fischer Technologies Inc. Feritscope (Model Number FMP30) was used to conduct screening studies of CASS ferrite levels. The FMP30 (Figure 3.3) uses a pair of coils, with one coil acting as the primary coil that induces currents in the specimen and measures the resulting change in induced current in the secondary coil.

The instrument has a measurement range from 0.1 to 80% Fe. Calculations based on preliminary measurements indicated that the standard uncertainty (a measure of the repeatability) was about 1%, but was a function of liftoff, probe canting angle, and the proximity to an edge. The FMP30 uses a vendor-provided set of ferrite calibration standards that are traceable to TWI secondary standards that fulfil ISO 8249 and AWS A4.2M requirements. While several standards (covering different ranges of percent ferrite) are available from the manufacturer of the instrument, the standards used for the studies documented in this report covered the range from 0-33.75% (Figure 3.4) as this was the expected range of ferrite levels in the CASS specimens being studied. The calibration of the instrument followed the manufacturer-recommended procedure, wherein the instrument is used to take multiple measurements on each of the standards. The instrument averages the measured values and uses the true value of percent ferrite on the standards to generate an internally stored mapping from measurement to ferrite reading.

Figure 3.3. FMP30 Feritscope

Figure 3.4. Ferrite Calibration Standard. The base standard (left) has a ferrite content of 104%, while the other three have ferrite levels of 2.87%, 10.7%, and 33.5%.

Preliminary measurements were taken with the FMP30 to determine a measurement protocol and factors impacting the measurements. The data indicated that probe liftoff and proximity to the specimen edge resulted in erroneous measurements. As a result, all subsequent measurements were made with the probe in contact with the specimen surface, and at least 0.51 cm (0.2 in.) away from the specimen edge (based on the instrument manufacturer's recommendation). Some of the specimens had a clear-coat spray-on finish to protect etched microstructure; when measurements were required on these surfaces, the clear-coat finish was removed prior to making the measurement to avoid errors due to probe lift-off.

Two sets of ferrite measurements were taken. During the first phase, measurements were made on a subset of the specimens, over a 5.1 cm (2 in.) square area with a grid spacing of 0.51 cm (0.2 in.) (referred to hereafter as the fine-grid scans), with measurements taken at the grid points. The fine-grid scan measurements were taken on the OD surface as well as on the through-thickness cross-sections. The through-thickness cross-sections included either the axial-radial cross section (i.e., the cross section transverse to weld or the "side-view" of the pipe segment), the circumferential-radial cross section (i.e., cross section parallel to weld or the "end-view" of the pipe segment), or both.

Figure 3.5 shows the sample geometry with the different measurement fine-grid scan grids marked on specimen B-516. A close-up view of a single OD grid is shown in Figure 3.6. Specimens examined in these initial scans included both CCSS pipe and SCSS components (such as elbows).

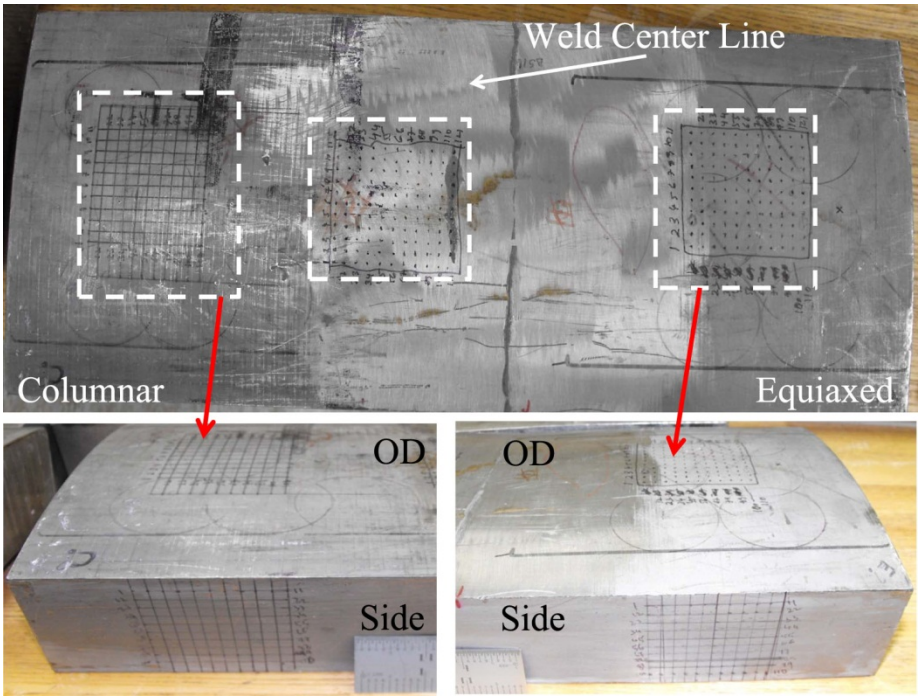

Figure 3.5. B-516 Measurement Grids. The figure shows the fine-grid scans on the OD surface and the side (axial-radial cross section) surfaces for the columnar and equiaxed grain sections.

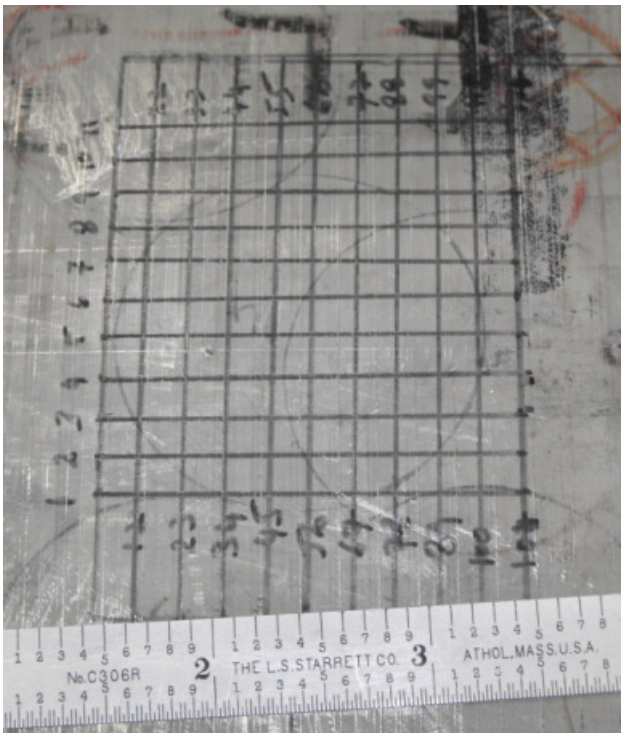

Figure 3.6. Close-up View of a Fine-Grid OD Surface Measurement Grid for Columnar Microstructure Region on B-516-C

The second phase of measurements consisted of measurements made on the OD and ID surfaces of the CCSS pipe across all specimens. Based on the data from the fine-grid scans, these measurements were made on a grid covering the entire surface of the pipe section, with the grid spacing varying between 2.54 cm (1 in.) and 7.6 cm (3 in.) depending on the specimen (referred to hereafter as the "coarse grid"). Measurements on the ID and OD surfaces were made along the same radial line. At each position, five measurements of the ferrite content were taken and averaged to reduce the effect of noise and variability due to manual positioning of the probe. Figure 3.7 shows the sample geometry with the larger, 2.54 cm (1 in.), grids marked on APE-1, a PWROG specimen.

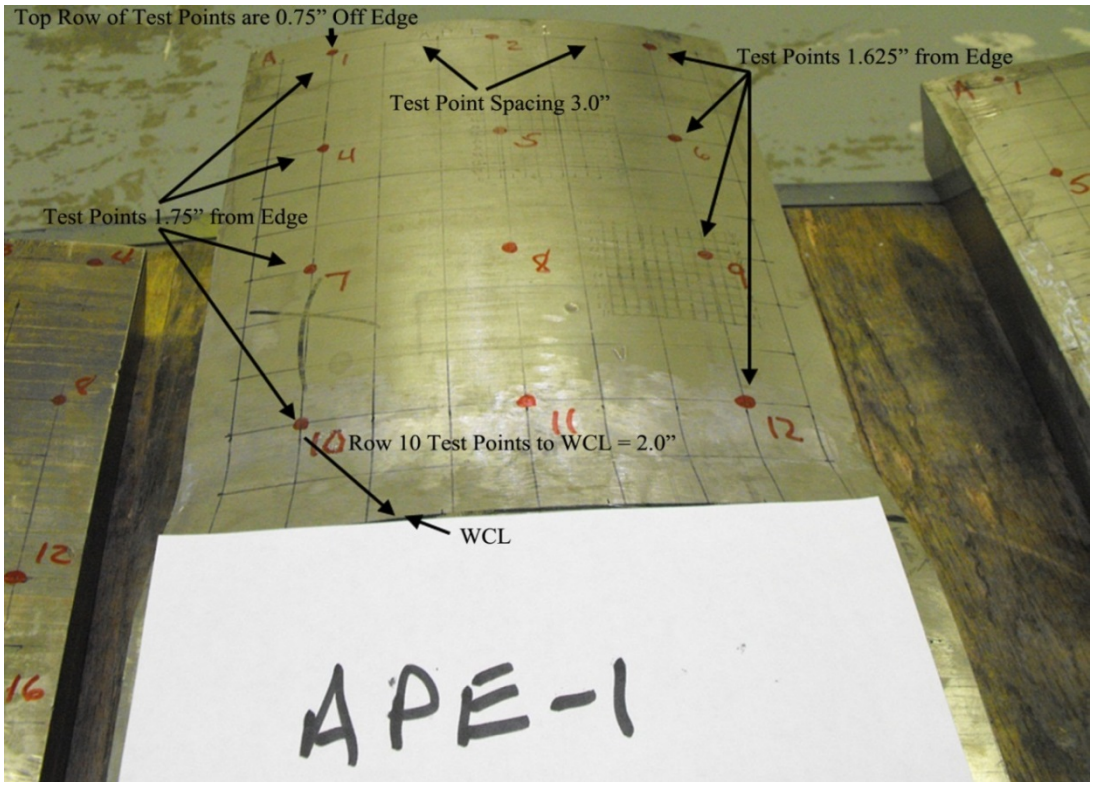

Figure 3.7. Overview of APE-1 Specimen Geometry. The 2.54 cm (1 in.) grid corresponds to the locations where the ferrite measurements were taken. The numbered locations (in red) refer to the locations where XRF measurements were taken (Section 3.3).

In both sizes of scans, the probe was moved from one grid location to the next manually, and all measurements were taken with zero liftoff. The surface was cleaned with acetone prior to taking the measurements.

Figures 3.8 through 3.10 present examples of the fine-grid ferrite measurements from the FMP30 Feritscope.

Figure 3.8 presents the OD surface scans for purely columnar, purely equiaxed, and weld regions of CCSS piping sections (B-516), while Figure 3.9 shows the axial-radial cross section scans of the same specimen. The figures present the data as color-coded images, with black corresponding to 0% ferrite and light yellow corresponding to 30% ferrite. Figure 3.10(a)–(c) presents similar measurements for PWROG specimen APE-1. The data presented are the OD surface scans for an SCSS elbow, region overlapping with SCSS elbow and weld, and CCSS piping, while Figure 3.10(d) shows the end-surface, or the circumferential-radial cross section, scans on the CCSS piping. Both the SCSS and CCSS sections of this specimen have mixed and banded microstructures.

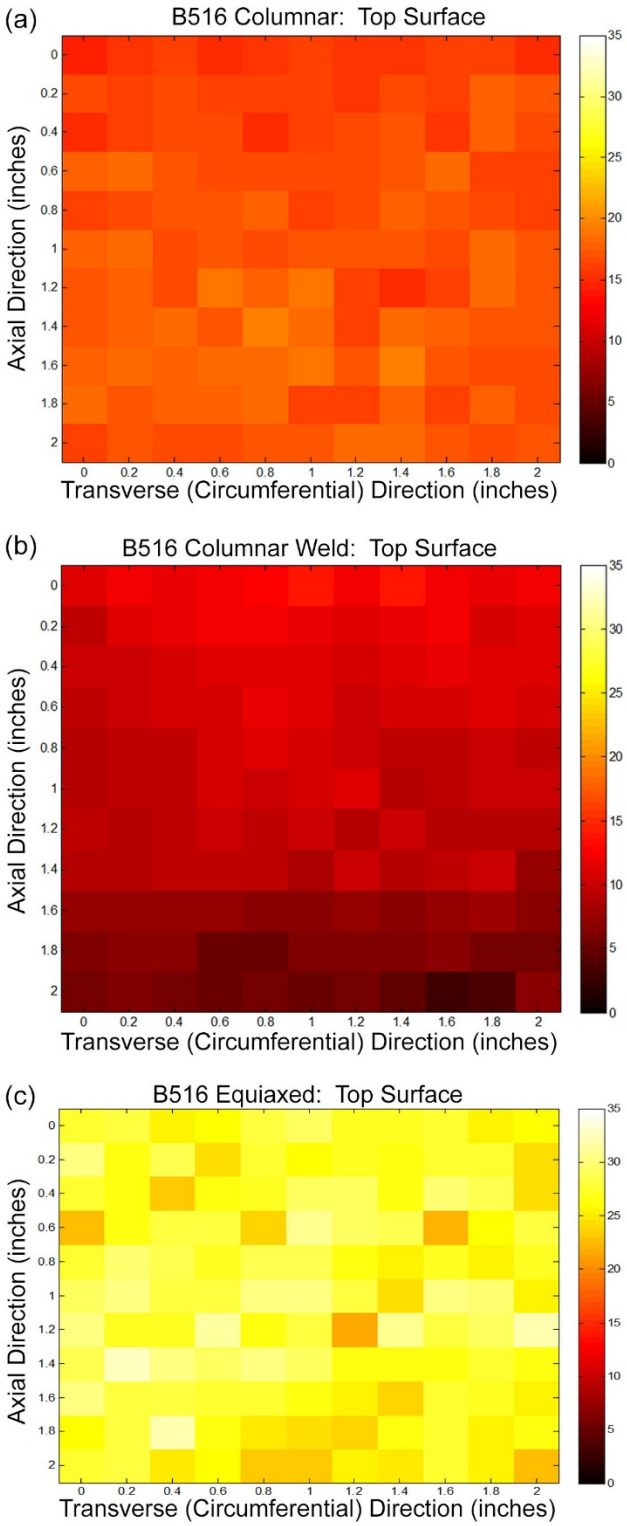

Figure 3.8. B-516, OD Surface Scan, on the Fine Grid. In all three figures, the y-axis is the axial direction on the pipe segment. (a) Columnar—the y-axis is increasing toward the weld centerline. (b) Columnar and weld region—the y-axis is increasing toward the weld centerline. The scan area overlapped the columnar region and a portion of the weld. (c) Equiaxed region—the y-axis is increasing away from the weld.

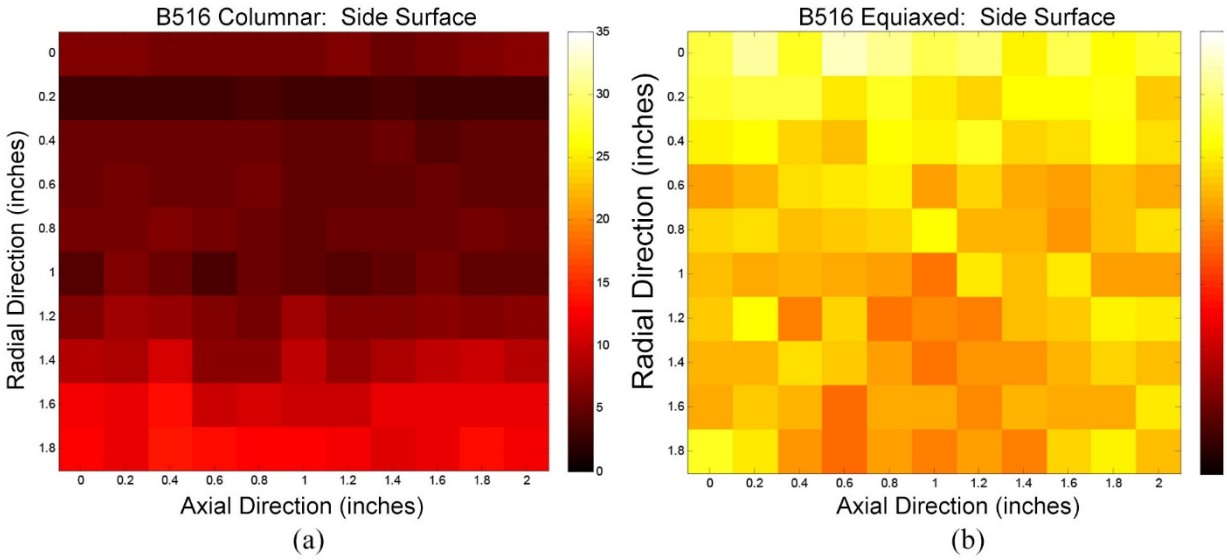

Figure 3.9. B-516, Axial-radial Cross-section Scan, on the Fine Grid. In both figures, the y-axis is the radial direction and is increasing from the OD to the ID. (a) Columnar region; (b) Equiaxed region.

Figure 3.11 and Figure 3.12 present another example of the measurement (in the circumferential-radial cross section) from a banded microstructure. Figure 3.11 shows the cross-section of the specimen (courtesy of IHI Southwest), while Figure 3.12 shows the measured ferrite content.

These preliminary measurements seem to indicate that the ferrite content is generally homogeneous on the surface but not necessarily through the thickness, with some variation near the weld region. The homogeneity is illustrated in Figures 3.8(a), 3.8(c), 3.10(a), and 3.10(c). The variation near the welds and through cross sections is illustrated in Figures 3.8(b), 3.9(a), 3.9(b), 3.10(b), and 3.10(d). The local OD homogeneity justified larger, coarse grids often covering the entire CCSS specimen. These 2.54 cm (1 in.) or larger grid spacing scans were performed only on CCSS pipe, and on both the OD and ID (see Section 4.2.2).

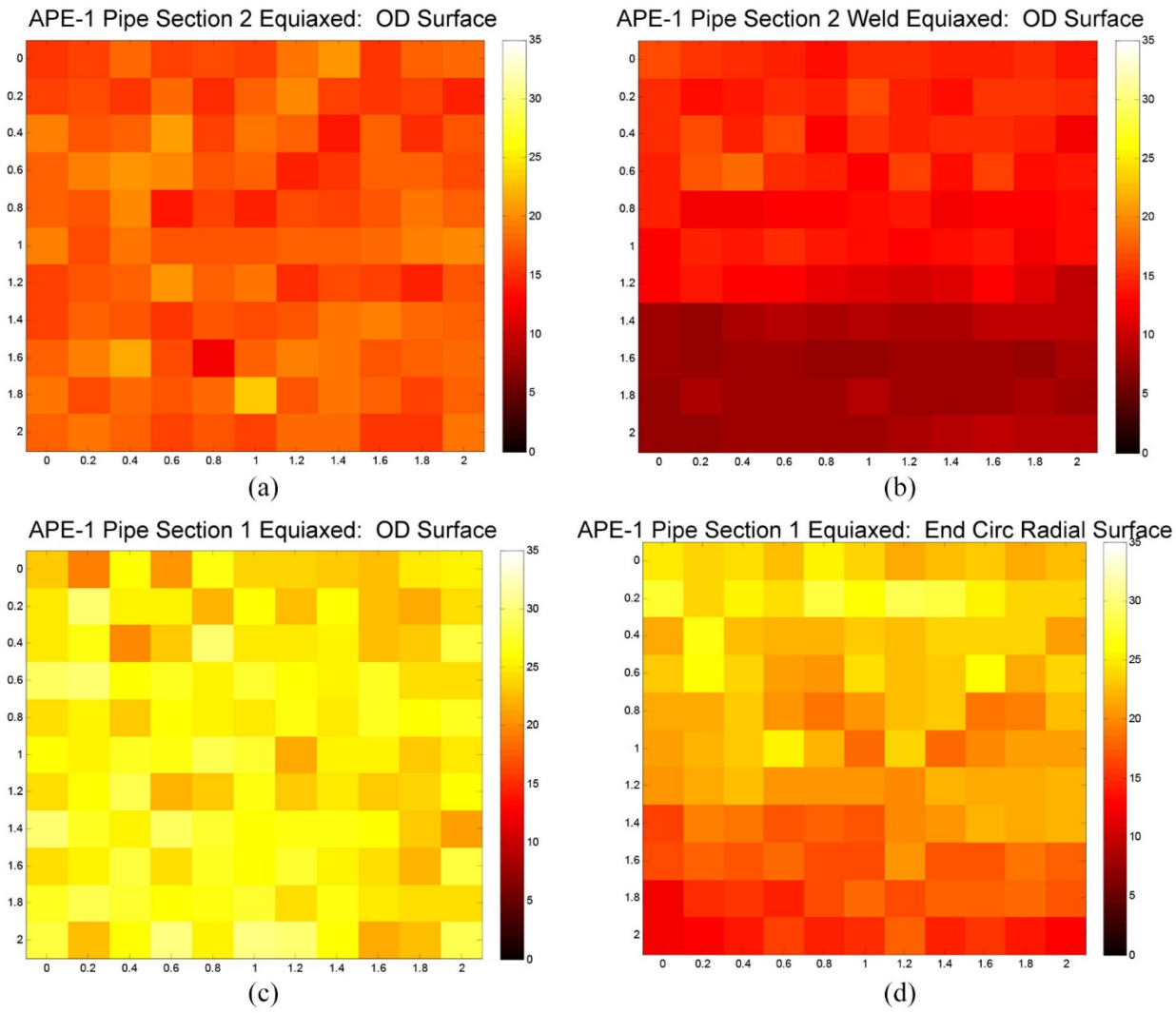

Figure 3.10. APE-1, OD Surface Scan, Fine-Grid Scan with 5.1 mm (0.2 in.) Spatial Resolution. (a) SCSS elbow region; (b) region overlapping the SCSS elbow section and weld; (c) CCSS pipe OD surface scan; and (d) circumferential-radial cross-section of CCSS piping. For (a)–(c), the y-axis is along the pipe axis; the x-axis is along the pipe circumference. For (d), the y-axis (radial direction) increases from OD to ID. The x-axis corresponds to the circumferential direction.

Figure 3.11. Overview of Mixed Microstructure Specimen (IHI Southwest ring)

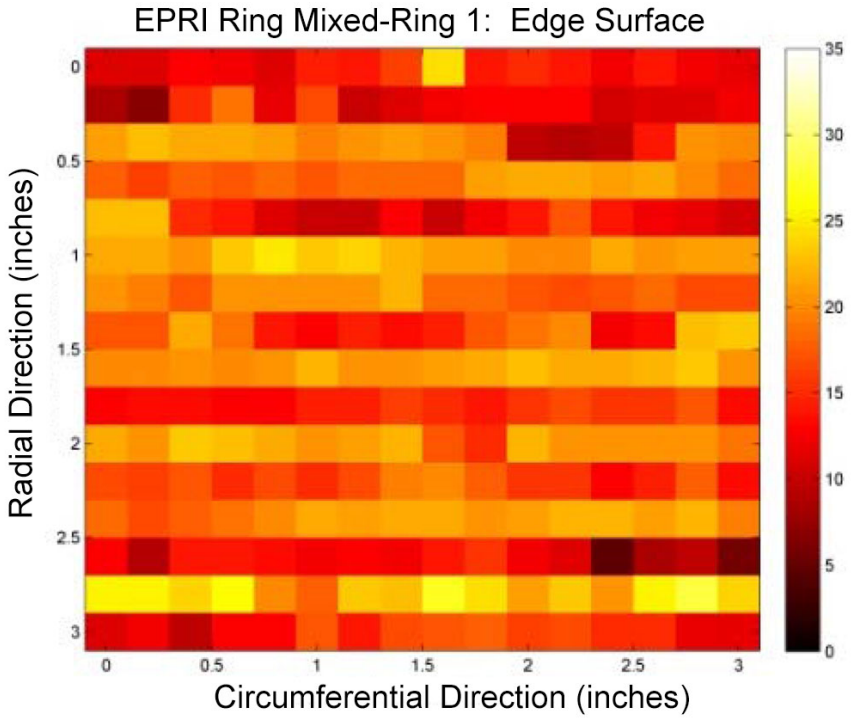

Figure 3.12. Ferrite Values in IHI Ring Specimen Circumferential-Radial Cross Section, Fine-Grid Scans. The y-axis (radial direction) increases from ID to OD. The x-axis corresponds to the circumferential direction.

Figure 3.13 presents an example of the data from the coarse grid scans. The figure presents the OD (Figure 3.13(a)) and ID (Figure 3.13(b)) scans on the CCSS pipe section of specimen MPE-6. Again, variability in the region close to the weld is evident, with relative homogeneity of the measurements away from the weld. Note that the ID measurements do not appear to show significant variability, even close to the weld.

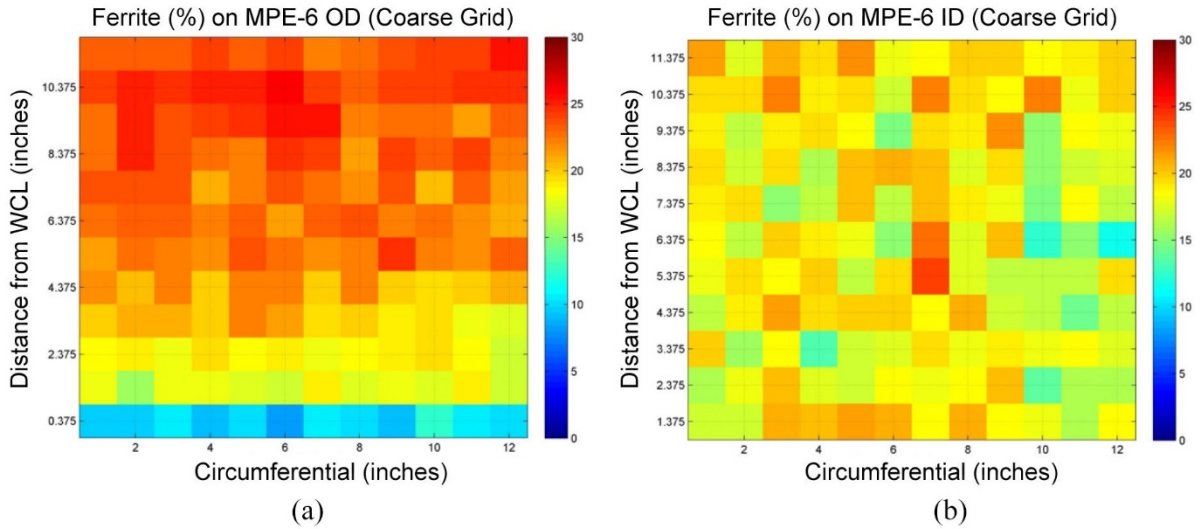

Figure 3.13. Ferrite Measurements on a Coarse Grid (with 2.54 cm [1 in.] grid spacing on the OD) on Specimen MPE-6: (a) OD measurements, (b) ID measurements. In both figures, the vertical axis is along the axis of the CCSS pipe, with the weld center line close to the bottom of the figure.

3.3 X-Ray Fluorescence Measurements

XRF measurements were made on the same specimens listed above using a Bruker AXS Turbo^{SD} S1 handheld XRF measurement unit (Figure 3.14). The unit was loaned by Bruker AXS in Kennewick, Washington, and was operated at the 40 kV setting, the default setting.

Figure 3.14. Bruker AXS Turbo^{SD} S1 (courtesy Bruker Corp.)

The unit was calibrated using calibration check samples with known elemental compositions. The measurement repeatability for the instrument was a function of dwell time and the element whose composition is being measured. In this study, the dwell time was fixed to 30 seconds, based on the reported standard error in preliminary measurements performed on a subset of samples.

Measurements on both the inner (ID) and outer (OD) surface of the pipe were made. All measurements were made on the same coarse grid locations used for the ferrite measurements. As with the ferrite measurements, the grid locations for corresponding inner and outer surfaces were along the same radial line.

Table 3.3 shows an example of the recorded data from specimen MPE-6. The table presents both the XRF measured concentration of the different elements and the estimated error in these readings. Each row of the table corresponds to a different measurement grid location. Data from both the OD and ID surfaces are presented. From the recorded data, spreadsheets were developed listing the elements pertinent to ferrite content according Aubrey et al. (1982) and Hammar and Svenson (1979). The spreadsheets included the mean and standard deviation (computed over all the measurement grid locations on the ID or OD) of the elemental measurements of Mn, Cr, Ni, and Mo as well as the calculation of ferrite using the model #1 as described by Aubrey et al. (1982). Also, for some specimens additional spreadsheets were developed calculating the mean and standard deviation by omitting measurements that were considered outliers (outside one standard deviation from the mean, when the standard deviation was greater than the percent elemental error calculated by the instrumentation). In all cases, these outliers were due either to the measurement location being very close to a label (or other similar item affixed to the surface) or due to local surface irregularities that made good contact of the instrument with the surface difficult. This refinement was performed on those specimens where the standard deviation of the measurement was significantly greater than the estimated error shown in the elemental measurements (e.g., Table 3.3).

Table 3.3. XRF Measurements from OD and ID Surfaces of Specimen MPE-6. The listings show the measured quantity (in percent) of each element along with the estimated error.

		Element Composition (Estimated Percent, and Percent Error in Estimate)											
	Location	Mn	Mn Err	Cr	Cr Err	Ni	Ni Err	Mo	Mo Err	Co	Co Err	Nb	Nb Err
OD Surface	1	0.5908	0.0519	20.397	0.0824	8.1522	0.0825	0.0067	0.0036	0.1199	0.0437	0.0055	0.0021
	2	0.551	0.0511	20.3895	0.0814	8.1753	0.0814	0.0038	0.0035	0.1197	0.0431	0.0055	0.0021
	3	0.5819	0.055	20.3881	0.0874	8.1422	0.0873	0.0045	0.0038	0.1374	0.0464	0.0059	0.0023
	4	0.5356	0.0529	20.3803	0.0844	8.2076	0.0848	0.0043	0.0037	0.157	0.0449	0.0069	0.0022
	5	0.56	0.0509	20.3913	0.081	8.1882	0.0814	0.0039	0.0035	0.1249	0.043	0.0054	0.0021
	6	0.5694	0.0516	20.4324	0.0822	8.2236	0.0824	0.0053	0.0036	0.1216	0.0435	0.0052	0.0021
	7	0.5637	0.0509	20.2565	0.0808	8.117	0.0812	0.0045	0.0035	0.1349	0.0431	0.0066	0.0021
	8	0.5892	0.0523	20.3055	0.083	8.2242	0.0838	0.0063	0.0037	0.1547	0.0443	0.0054	0.0022
	9	0.5292	0.0515	20.3927	0.0821	8.1799	0.0828	0.0021	0.0035	0.111	0.0435	0.005	0.0021
	10	0.5231	0.0515	20.4223	0.0822	8.1439	0.0823	0.0058	0.0036	0.109	0.0434	0.0072	0.0022
	11	0.5565	0.0538	20.2736	0.0854	8.182	0.086	0.0042	0.0037	0.074	0.0451	0.0066	0.0023
	12	0.5849	0.0519	20.413	0.0825	8.1568	0.0825	0.0049	0.0036	0.1249	0.0437	0.0061	0.0022
	13	0.5677	0.0507	20.3521	0.0805	8.2049	0.0813	0.0021	0.0034	0.0741	0.0425	0.0055	0.0021
	14	0.575	0.0507	20.3572	0.0804	8.1947	0.081	0.0055	0.0035	0.1081	0.0426	0.0055	0.0021
	15	0.5349	0.0507	20.3618	0.0809	8.2223	0.0814	0.003	0.0035	0.0891	0.0427	0.0038	0.002
	16	0.5385	0.0514	20.288	0.0818	8.2184	0.0826	0.0032	0.0035	0.1172	0.0434	0.0044	0.0021
ID Surface	1	0.5114	0.0506	20.3282	0.0809	8.4422	0.0828	0.0064	0.0036	0.0992	0.0428	0.0053	0.0021
	2	0.5124	0.0507	20.2799	0.0808	8.2299	0.0817	0.0048	0.0035	0.0904	0.0428	0.0047	0.0021
	3	0.6079	0.0531	20.1256	0.0837	8.2111	0.0848	0.0053	0.0037	0.1078	0.0446	0.0058	0.0022
	4	0.5215	0.0515	20.2272	0.0821	8.2961	0.0832	0.0036	0.0036	0.1458	0.0438	0.0036	0.0021
	5	0.5568	0.0519	20.2318	0.0823	8.0782	0.0826	0.0038	0.0036	0.1323	0.0439	0.0064	0.0022
	6	0.5891	0.0517	20.1284	0.0816	8.0796	0.0825	0.0023	0.0035	0.1232	0.0436	0.0061	0.0022
	7	0.494	0.0511	20.1809	0.0814	8.0732	0.082	0.0016	0.0035	0.1078	0.0433	0.0065	0.0022
	8	0.5206	0.0508	20.234	0.0809	8.2888	0.0823	0.0045	0.0035	0.0858	0.0428	0.0051	0.0021
	9	0.5202	0.0507	20.1376	0.0806	8.1261	0.0815	0.003	0.0035	0.1256	0.043	0.0065	0.0021
	10	0.5372	0.0514	20.0965	0.0815	8.0399	0.0821	0.0035	0.0035	0.1269	0.0436	0.0057	0.0021
	11	0.5125	0.0516	20.2594	0.0822	8.1153	0.0827	0.0031	0.0036	0.1343	0.0438	0.005	0.0021
	12	0.4954	0.0527	20.3184	0.0842	8.1213	0.0844	0.005	0.0037	0.1314	0.0447	0.0065	0.0022
	13	0.5196	0.0541	20.1568	0.086	8.1783	0.0875	0.0063	0.0038	0.0983	0.0458	0.0075	0.0023
	14	0.5837	0.0513	20.1819	0.0814	8.3457	0.0832	0.0064	0.0036	0.0759	0.0431	0.0058	0.0021
	15	0.5883	0.0515	20.1593	0.0813	8.1507	0.0823	0.0046	0.0036	0.101	0.0433		
	16	0.5275	0.0527	20.1282	0.084	8.4824	0.0867	0.0069	0.0037	0.119	0.0447	0.0073	0.0023

Table 3.3 (continued)

		Element Composition (Estimated Percent, and Error in Estimate)									
	Location	V	V Err	Fe	Fe Err	Ti	Ti Err	Cu	Cu Err	W	W Err
OD Surface	1	0.0223	0.0164	69.9363	0.1027			0.0778	0.0117	0.0065	0.0065
	2	0.0079	0.0159	69.9749	0.1015	0.004	0.0146	0.0589	0.011	0.0098	0.0068
	3	0.0162	0.0172	69.9677	0.109			0.0705	0.0122	0.0127	0.0075
	4	0.0177	0.0167	69.915	0.1054	0.0044	0.0151	0.0782	0.012	0.0153	0.0075
	5	0.0223	0.0161	69.9134	0.1012			0.0906	0.0119	0.0191	0.0075
	6	0.0151	0.0161	69.8521	0.1024	0.0012	0.0146	0.0739	0.0116	0.0106	0.0069
	7	0.0263	0.0162	70.0988	0.1012	0.0037	0.0146	0.0892	0.0118	0.0169	0.0074
	8	0.0247	0.0166	69.8836	0.1041	0.0021	0.0149	0.1148	0.0128	0.024	0.0082
	9	0.037	0.0167	69.9489	0.1025	0.01	0.0149	0.0902	0.012	0.0109	0.0069
	10	0.0191	0.0163	69.9726	0.1024	0.0044	0.0147	0.0814	0.0118	0.0132	0.0071
	11	0.0211	0.0169	70.096	0.1069			0.0769	0.0121	0.0143	0.0075
	12	0.0155	0.0163	69.8635	0.1029	0.014	0.015	0.1031	0.0124	0.0187	0.0076
	13	0.0314	0.0162	69.9778	0.1007			0.0984	0.012	0.0122	0.0069
	14	0.028	0.0161	69.9497	0.1005			0.073	0.0113	0.0162	0.0073
	15	0.0152	0.016	69.9521	0.101	0.0159	0.0148	0.0917	0.0119	0.0111	0.0068
	16	0.0228	0.0163	70.0137	0.1024	0.0075	0.0148	0.0982	0.0122	0.0097	0.0068
ID Surface	1	0.0293	0.0162	69.8251	0.1014			0.0714	0.0114	0.0104	0.0068
	2	0.0241	0.0161	70.0875	0.1013			0.0741	0.0114	0.016	0.0073
	3	0.0166	0.0166	70.1363	0.1054	0.0048	0.0152	0.0797	0.012	0.0106	0.0071
	4	0.0179	0.0162	70.0402	0.103			0.0827	0.0119	0.014	0.0072
	5	0.0247	0.0165	70.125	0.1032	0.0236	0.0154	0.1043	0.0124	0.0218	0.0079
	6	0.0253	0.0167	70.1147	0.1028	0.0784	0.0166	0.116	0.0127	0.0251	0.0081
	7	0.0322	0.0165	70.2813	0.1021	0.0155	0.015	0.0943	0.012	0.02	0.0077
	8	0.0289	0.0163	70.0385	0.1015	0.0012	0.0145	0.0927	0.012	0.017	0.0074
	9	0.0201	0.0164	70.1245	0.1015	0.0828	0.0165	0.1061	0.0123	0.0309	0.0085
	10	0.0204	0.0165	70.2899	0.1026	0.0555	0.0161	0.1017	0.0123	0.0183	0.0076
	11	0.021	0.0165	70.0779	0.1031	0.0508	0.016	0.0956	0.0122	0.0232	0.008
	12	0.0226	0.0168	70.074	0.1053	0.0158	0.0154	0.096	0.0125	0.0234	0.0082
	13	0.0266	0.0177	70.0467	0.1084	0.0992	0.018	0.1107	0.0132	0.025	0.0086
	14	0.0061	0.0163	69.8013	0.1027	0.1038	0.0171	0.1212	0.0128	0.0296	0.0084
	15	0.021	0.0164	70.0782	0.1023	0.0496	0.0159	0.1207	0.0128	0.0223	0.0079
	16	0.0183	0.0169	69.8169	0.1062	0.0708	0.0169	0.1112	0.013	0.0204	0.008

4.0 Discussion of Results

This section contains a detailed discussion based on the measured ferrite content (from the Feritscope), calculated ferrite content (from XRF-measured elemental composition), calculated ferrite content (based on ladle analysis where available), and XRF-measured elemental composition. A measure of grain structure (the percentage of columnar grains) in specimens, based on metallographic data, is first briefly described. The Feritscope measurements (including the fine-grid scan and large 2.54 cm [1 in.] grid scan data) are analyzed, followed by the XRF measurements. The percentage of columnar grains is then used as an overall measure of grain structure, to determine whether correlations exist between the grain structure, Feritscope-measured ferrite content, calculated ferrite content (from XRF), calculated ferrite content (from ladle analysis, where available), and XRF-measured elemental content. The standard errors reported in this section are based on the measurement method used, and are briefly summarized below:

- Calculated ferrite from ladle composition: The reported error is based on reported compositional variation by the foundry (Table 3.2).
- Calculated ferrite from XRF-measured elemental composition: The estimated error is a function of the percent elemental error calculated by the instrumentation.
- Measured ferrite using Feritscope: The standard error is estimated based on repeated measurements taken using the Feritscope on test locations on multiple specimens.
- Measured elemental composition from XRF: The standard error is the percent elemental error calculated by the instrumentation.

Qualitative comparisons between measured and calculated ferrite content are also reported in this section, to determine how the direct measurement of ferrite compares to the calculated value, and whether differences in these quantities are dependent on grain structure.

4.1 An Overall Measure of Grain Structure

This section briefly describes proposed criteria for applying the grain structure observed in CCSS specimens to produce a value for grain type. The process relies on the data cited in Ruud et al. (2009, Table 4.4), and the availability of photomicrographs.

Micrographs showing the through-thickness grain structure were obtained for all of the specimens studied herein, except the UMich and Manoir specimens. The grain structure presented in the micrographs was used to produce a value for the proportion of columnar grains in each of the specimens. Bands with purely columnar grains were assigned a value of 100% columnar grains, while whose with purely equiaxed grains were assigned a value of 0% columnar grains. It was arbitrarily decided that the designation MG (mixed grain) would mean 50% columnar grains. For specimens with a single band, this approach produces a measure of grain structure. In specimens with multiple bands, a weighted average was used. Specifically, if the cross-sectional thickness of the specimen is d, and the specimen has n bands of thickness $d_1,d_2,\ldots,d_n$ and percentage columnar grains in the bands designated by $c_1,c_1,\ldots,c_n$, respectively, then the overall percent of columnar grains is computed as:

$$c_{av} = \frac{c_1 d_1 + c_2 d_2 + \ldots c_n d_n}{d_1 + d_2 + \ldots d_n} \times 100\% .$$

4.2 Feritscope Measurements

4.2.1 Fine-Grid Scans

The complete list of fine-grid OD surface scans and through-wall scans, along with the specimens on which the measurements were made, are summarized in Table 4.1. Table 4.2 lists the foundry, heat numbers, and summarizes the data from the OD surface and through-thickness cross-section scans for the eight specimens measured in the fine-grid scans. The Table 4.1 listing includes through-wall cross-section scans from seven of the eight specimens. These scans were performed on the axial-radial and/or circumferential radial cross sections through the specimen wall. Table 4.3 summarizes the ferrite information from these fine-grid scans on seven of the eight specimens and includes information on variation of ferrite from near the OD to near the ID. Note that, as the Feritscope probe radius was 2.9 mm (0.114 in), the center of the scan row in the through-wall direction nearest the OD ranged from 5.7 mm (0.224 in.) to 10.2 mm (0.404 in.) below the OD. Likewise, the center of the scan row nearest the ID ranged from 6.2 mm (0.244 in.) to 13.6 mm (0.534 in.) above the ID. Thus, the probe was remote enough from the ID and OD surfaces to eliminate concerns due to edge effects.

4.2.1.1 Variation of Ferrite from Scan to Scan and Within a Scan

The variation (standard deviation) within any column or row in a scan area on the OD surface of the CCSS pipe was evaluated to reveal variations due to heat treating, welding, or casting. Casting inhomogeneities would be revealed by XRF elemental variations and will be discussed in Section 4.2.1.2. Table 4.2 lists the maximum, minimum, and mean standard deviation for the fine-grid scans of the eight specimens previously listed.

The standard estimated error of the Feritscope is one parameter that may be used to determine homogeneity of the measured ferrite. Specifically, if the measured ferrite is within the standard estimated error, then the ferrite could be judged as homogeneous. This evaluation requires an assessment of the standard estimated error of the Feritscope. Available literature provides some insights into expected values for this parameter. Aubrey et al. (1982), based on Feritscope and metallographic ferrite measurements, concluded that the standard estimated error for Feritscope measurements was 1.2%. However, they report that for some of the 25% to 34% ferrite specimens, differences between the Feritscope and metallographic percentages were as high as 8.9%. Ratz and Gunia (1969), page 80, reported estimated error for measured and calculated ferrite of ± 3% for specimens with less than 10% ferrite and ±6% for specimens with 10% to 24% ferrite. In the present study, considering measurement difficulties on these curved and machined specimens and based on measurements taken using the Feritscope on test locations on multiple specimens, the standard error in the measurements reported here was estimated at less than 3% ferrite.

Only the fine-grid scan ferrite measurements on the OD of the CCSS pipe and at sufficient distance from the weld center line (W_{CL}) were considered in determining the homogeneity within the fine-grid scans. For the purposes of these measurements, "sufficient distance from the W_{CL}" was arbitrarily defined as the distance equal to the wall thickness of the CCSS pipes [about 6.3 cm (2.5 in.)].

Table 4.1. Listing of Fine-Grid Feritscope Scans

Number @ Table 4.4 (Ruud et al. 2009)	Identifi-cation	Scan A	Scan B	Scan C	Scan D	Scan E	Scan F
1	APE-1 PWROG	CCSS, OD	SCSS, OD	CCSS, Circ-Rad	SCSS, OD	SCSS & Weld Metal, OD	
7	MPE-6 PWROG	SCSS, OD	SCSS, OD	SCSS/Weld, OD	CCSS, OD	CCSS, Circ-Rad	SCSS, Circ-Rad
12	OPE-2 PWROG	CCSS, OD	SCSS/Weld, OD	SCSS, OD	No Scan Data	No Scan Data	No Scan Data
18	AAD#2 SwRI	CCSS, Circ-Rad	No Scan Data	No Scan Data	No Scan Data	No Scan Data	No Scan Data
21	IHI SwRI	CCSS, Circ-Rad	No Scan Data	No Scan Data	No Scan Data	No Scan Data	No Scan Data
NA	B-510	CCSS, OD, Columnar Side	CCSS, OD, Equiaxed Side	CCSS, Axial-Rad, Columnar Side	CCSS, Axial-Rad, Equiaxed Side	CCSS, Circ-Rad, Equiaxed Side	CCSS, Circ-Rad, Columnar Side
NA	B-516	CCSS, OD, Columnar Side	CCSS, OD, Equiaxed Side	CCSS, Axial-Rad, Equiaxed Side	CCSS, OD, Col Side, Overlapping CCSS & Weld	CCSS, Axial-Rad, Col Side	
NA	B-527	CCSS, OD, Equiaxed Side	CCSS, OD, Columnar Side	CCSS, Axial-Rad, Equiaxed Side	CCSS, Axial-Rad, Columnar Side	CCSS, Circ-Rad, Columnar Side	CCSS, Circ-Rad, Equiaxed Side

NA = not applicable

Table 4.2. Maximum, Minimum, and Mean Standard Deviation Feritscope-Measured Percent Ferrite for the Rows and Columns of Fine-Grid Scans on Selected CASS Specimens

Specimen/ Scan	Foundry/Heat	Scan Surface	Mean Ferrite %	CCSS or SCSS	Circ Min S.D.	Circ Max S.D.	Circ Mean S.D.	Axl Min S.D.	Axl Max S.D.	Axl Mean S.D.
APE-1/A	SFM 156529	OD	25.5	CCSS	1.18	3.28	2.10	1.3	3.06	2.13
APE-1/B	ESCO 28594-3	OD	17.5	SCSS	1.09	2.33		1.22	2.19	
APE-1/C	SFM 156529	Circ-Rad		CCSS	0.85	2.16		3.25	4.98	
APE-1/D	ESCO 28594-3	OD	17.9	SCSS	1.56	2.88		1.07	2.53	
APE-1/E	ESCO 28594-3	OD	11.9	SCSS & Weld	0.32	1.67		2.62	3.88	
MPE-6-A/A	ESCO 28594-3	OD	13.0	SCSS	2.64	3.47		0.56	1.89	
MPE-6-A/B	ESCO 28594-3	OD	17.0	SCSS	0.67	2.09		2.46	3.48	
MPE-6-A/C	ESCO 28594-3	OD	11.2	SCSS	0.52	2.41		1.99	3.18	
MPE-6-A/D	SFM 156529	OD	23.1	CCSS	0.88	2.30		1.02	2.30	
MPE-6-A/E	SFM 156529	Circ-Rad		CCSS	1.00	2.07		2.96	4.17	
MPE-6-A/F	ESCO 28594-3	Circ-Rad		SCSS	1.21	2.30		1.25	2.69	
OPE-2/A	USP C2291A	OD	20.9	CCSS	0.71	1.24		0.86	1.66	
OPE-2/B	ESCO 72176-1	OD	12.7	SCSS & Weld	0.44	2.35		5.92	8.24	
OPE-2/C	ESCO 72176-1	OD	25.4	SCSS	1.27	2.80		1.59	3.19	
AAD#2/A		Circ-Rad		CCSS	0.46	1.65		1.13	2.08	
IHI/ A		Circ-Rad		CCSS	1.06	4.74		3.54	5.34	
B-510C/A		OD	5.6	CCSS	1.28	1.82	1.54	0.28	0.73	0.55
B-510C/C		Axl-Rad		CCSS	0.40	1.11	0.61	2.23	3.17	
B-510C/F		Circ-Rad		CCSS	0.14	0.70		0.96	1.28	
B-510E/B		OD	11.9	CCSS	0.87	2.08	1.60	0.83	1.76	1.36
B-510E/D		Axl-Rad		CCSS	1.62	4.17		1.47	2.26	
B-510E/F		Circ-Rad		CCSS	0.14	0.70		0.96	1.28	

Table 4.2. (continued)

Specimen/ Scan	Foundry/Heat	Scan Surface	Mean Ferrite %	CCSS or SCSS	Circ Min S.D.	Circ Max S.D.	Circ Mean S.D.	Axl Min S.D.	Axl Max S.D.	Axl Mean S.D.
B-516C/A		OD	17.0	CCSS	0.52	1.18	0.75	0.59	1.29	0.95
B-516C/D		OD	9.3	CCSS	0.35	1.18		1.56	2.70	
B-516C/E		Axl-Rad		CCSS	0.19	1.26		2.76	3.69	
B-516E/B		OD	27.3	CCSS	1.27	2.86	2.00	1.60	2.47	2.15
B-516E/C		Axl-Rad		CCSS	1.19	2.78		1.93	3.63	
B-527C/B		OD	5.1	CCSS	0.21	0.46	0.36	0.28	0.65	0.41
B-527C/D		Axl-Rad		CCSS	0.11	0.67		2.14	2.54	
B-527C/E		Circ-Rad		CCSS	0.15	0.69		1.03	1.60	
B-527E/A		OD	12.2	CCSS	1.35	2.58	2.00	0.64	1.69	1.23
B-527E/C		Axl-Rad		CCSS	0.58	1.97		1.77	2.78	
B-527E/F		Circ-Rad		CCSS	1.17	1.74		1.49	2.46	

S.D. = standard deviation

*Columns 6 through 8 for OD scans are always circumferential and 9 through 11 axial. For circumferential-radial through-thickness scans columns, 6 through 8 are circumferential and 9 through 11 radial. For axial-radial through-wall scans columns, 6 through 8 are axial and 9 through 11 radial.

Table 4.3. Summary Data from Fine-Grid Feritscope Scans of Through Wall on Seven* Selected CASS Specimens

Specimen/ Scan	Foundry Heat[a]	Cross Section	Percent Columnar Grains: Grain Structure[b]	Ferrite At OD	Ferrite Near OD[c]	Ferrite Near ID[d]	Mean Ferrite thru Thickness	Trend Near OD to ID[e]	Plotted Trend[f]
APE-1/C	SFM 156529	Circum-Radial	50%: 3 Bands of Mixed Grain	25.5 ± 2.1	23.4 ± 1.7	14.5 ± 1.6	20.7	Decrease	Decrease
MPE-6/E	SFM 156529	Circum-Radial	64%: 3 Bands, 2 Col to 1 Equ	23.1 ± 1.6	24.0 ± 1.2	17.7 ± 1.1	21.8	Decrease	Decrease
AAD-2/A	Unknown	Circum-Radial	86%: 3 Bands, 2 Col, 1 Mixed		18.7 ± 0.5	21.6 ± 1.4	21.0	Increase	Increase
IHI/A	Unknown	Circum-Radial	90% Bands of Columnar		14.2 ± 2.6	13.7 ± 3.2	17.3	No Trend	No Trend
B-510C/C	Unknown	Axial-Radial	100%: Columnar	5.6 ± 1.0	5.7 ± 0.5	12.2 ± 1.1	7.2	Increase	Increase
B-510C/F	Unknown	Circum-Radial	100%: Columnar	5.6 ± 1.0	1.2 ± 0.2	4.0 ± 0.5	3.0	No Trend	Increase
B-510E/D	Unknown	Axial-Radial	0%: Equiaxed	11.9 ± 1.5	17.1 ± 1.8	17.9 ± 4.2	17.6	No Trend	No Trend
B-510E/E	Unknown	Circum-Radial	0%: Equiaxed	11.9 ± 1.5	8.4 ± 1.7	12.2 ± 1.8	10.7	Increase	Increase
B-516C/E	Unknown	Axial-Radial	100%: Columnar	17.0 ± 0.9	6.0 ± 4.4	12.6 ± 0.8	6.9	Increase	Increase
B-516E/C	Unknown	Axial-Radial	0%: Equiaxed	27.3 ± 2.1	28.8 ± 2.2	22.0 ± 2.8	23.6	Decrease	Decrease
B-527C/D	Unknown	Axial-Radial	100%: Columnar	5.1 ± 0.4	3.8 ± 0.3	10.0 ± 0.7	5.2	Increase	Increase
B-527C/E	Unknown	Circum-Radial	100%: Columnar	5.1 ± 0.4	3.2 ± 0.3	7.2 ± 0.7	4.3	Increase	Increase
B-527E/C	Unknown	Axial-Radial	0%: Equiaxed	12.2 ± 1.6	14.6 ± 0.6	11.3 ± 1.0	15.9	Decrease	Decrease
B-527E/F	Unknown	Circum-Radial	0%: Equiaxed	12.2 ± 1.6	18.7 ± 1.2	13.3 ± 1.5	15.9	Decrease	Decrease

*Note, no through-wall scans were performed on Specimen OPE-2; thus, only seven of the eight specimens are listed in this table.

(a) SFM, ASTM CF8A; USP (U.S. Pipe), ASTM CF8A or CF8M
(b) The criteria and estimation of percent columnar grains from the micrographs of the specimens studied are discussed in Section 4.1.
(c) The Feritscope probe diameter was 5.78 mm (0.23 in.); thus, the center of the scan row nearest the OD ranged from 5.7 mm (2.8 + 2.9) [0.224 in. (0.11 + 0.114)] to 10.2 mm (7.3 + 2.9) [0.404 in. (0.29 + 0.114)] below the OD.
(d) The Feritscope probe diameter was 5.78 mm (0.23 in.); thus, the center of the scan row nearest the ID ranged from 6.2 mm (3.3 + 2.9) [0.244 in. (0.13 + 0.114)] to 13.6 mm (10.7 + 2.9) [0.534 in. (0.42 + 0.114)] below the ID.
(e) "No Trend" was noted when the difference between the OD and ID were within the standard deviation of the measurements. "Uncertain" was noted when the ferrite at OD and ferrite near OD do not imply the same trend within their standard deviations.
(f) Plots (graphs) of the mean ferrite of each row (axial or circumferential) vs. distance from the OD are shown in Appendix A.

The specimens and scans listed in Table 4.2 were reviewed to determine if the ferrite content of the CCSS pipe could be considered homogeneous within the fine-grid scans. The analysis computed the standard deviation of the measurements in the axial and circumferential directions to estimate the variability in the measured ferrite content in these directions. All but one, APE-1 scan A, of the OD measurements on CCSS pipe were judged homogeneous in that they showed a maximum standard deviation of percent ferrite (either axially or circumferentially) of less than 3%. However, the APE-1 scan A data showed four measurements that increased the overall standard deviation to beyond the measurement error estimate (3%). An examination of the specimen did not indicate any large changes in local surface roughness or potential for lift-off of the probe at these four locations. These four measurements were also not collocated (which might indicate a locally inhomogeneous region in the specimen). The standard deviation of the overall scan (including these four outliers) was also computed and found to be well within the estimated measurement error of 3%.

To rule out the possibility of localized inhomogeneities, previously collected eddy current measurements (for a related study on microstructure characterization of CASS) in the same region on specimen APE-1 were also analyzed; these measurements did not show any strong evidence of inhomogeneity either (the standard error in the axial and circumferential directions were generally less than 3%). Based on these analyses, it was concluded that these four measurements in specimen APE-1 were likely outliers due to measurement errors (for instance, errors in probe placement) and could be discarded for the present analysis.

Based on these analyses, it was concluded that the specimens were homogeneous within the fine-grid scan and the grid size could be increased from about 5.1 mm (0.2 in.), used in the fine-grid scans, to 2.54 cm (1 in.) or larger in subsequent measurements.

To compare the Feritscope readings from a single CCSS heat (pipe) incorporated in two or more specimens, Table 4.2 lists the foundry and heat numbers in the second column, and the mean percent ferrite from the scan in the fourth column. Note that only OD scan measurements obtained at a distance of at least one pipe thickness from the weld line are compared here. The data indicate:

- The difference between ferrite readings on two specimens (APE-1 and MPE-6) from the same heat (CCSS SFM heat 15629) is well within the standard estimated error. The ferrite percent listed in the fourth column in Table 4.2 shows mean ferrite percent of 25.5 and 23.1, for APE-1 and MPE-6, respectively.
- Specimen B-516C (columnar grained CCSS pipe), while nominally from the same piping segment (and therefore the same heat, but unknown heat number) as specimens B-510C and B-527C, has a different ferrite content than specimens B-510C and B-527C. The ferrite content for specimens B-510C and B-527C, measured from the OD surfaces, are 5.6 and 5.1, respectively, while B516C has a ferrite percent of 17.0 at the OD surface. Thus, B-510C and B-527C compare well within the standard error but B-516C does not.
- Specimen B-516E (equiaxed grained CCSS pipe), while nominally from the same piping segment (and therefore the same heat, but unknown heat number) as specimens B-510E and B-527E, has a different ferrite content than specimens B-510E and B-527E. The ferrite contents for the OD surfaces of B-510E and B-527E are from the same unknown heat and are 11.9 and 12.9, respectively, while the ferrite content for specimen B-516E is 27.3. Thus, B-510E and B-527E compare well within the standard error but B-516E does not.

The comparatively high percent ferrite measured on B-516C and B-516E indicates that this specimen (B-516) may have been subjected to a different thermal treatment than the other two. A related PISC-III specimen (B-515) is known to have been thermally stress-relieved, mechanically bent open, and then bent back to its original shape (Diaz et al. 2007). B-515 was not included in this study nor is there evidence that B-516 was bent; but if one specimen in the B series has undergone a special heat treatment, it is possible that another specimen in this series, for example, B-516, also may have been thermally treated resulting in a change in the ferrite content.

Nevertheless, the variation of ferrite from one scan to another, as well as within a single scan, is within the estimated measurement error and on all fine-grid OD surface scans that were at least the distance of the thickness of the CCSS specimen away from a weld (see column 5, Table 4.3). Column 5 of Table 4.3 shows that the measured percent ferrite on CCSS specimens of the same heat was within ±3% except for the columnar and equiaxed sides of B-516.

Moreover, comparison of the Mean Ferrite through-thickness (column 8 of Table 4.3) with the Ferrite at OD (column 5 of Table 4.3) shows good agreement with the SFM heats, except for specimen B-516C and B-516E, one of which may be from SFM 144179. Again this may indicate that B-516 may have undergone different heat treatment than the other PISC-III specimens. Also, the unknown heat used for the equiaxed side of the PISC-III does not show agreement within the ±3% for columns 5 and 8 in Table 4.3 on any of the three PISC-III specimens studied. However, B-510E and B-527E are within the ±6% for the 10 to 24% ferrite range observed by Ratz and Gunia (1969) on page 80 of their report.

Thus, the variation of Feritscope-measured ferrite within a fine-grid scan is for the most part within the ±3% estimated error for less than 10% ferrite and the ±6% for 10 to 24% ferrite (Ratz and Gunia 1969). Comparison of different specimens with the same heat number showed good correlation within these ranges, except for B-516 columnar and equiaxed sides.

4.2.1.2 Ferrite Content Trend OD to ID

Chopra and Sather (1990) noted that ferrite content is always lower toward the ID of CCSS pipe, apparently related to the nickel content; that is, enrichment of nickel in the liquidus near the ID; which would promote columnar grains. Their observation implies a decreasing trend of ferrite content from OD to ID. According to the trends shown in Table 4.3, the SFM heat number 156529 showed a decreasing trend but the unknown heat in the AAD-2 specimen did not, and only two of the five cross-section scans of the unknown equiaxed PISC-III showed the decreasing trend. Three of the five columnar PISC-III cross-section scans showed the opposite (increasing) trend of ferrite content from OD to ID, one showed increasing, and one showed no trend.

Example plots (graphs) of through-thickness mean ferrite percent vs. distance from the OD are shown in Figures 4.1 and 4.2, with the data from all of the specimens shown in Appendix A. While not necessarily representative of measurements from the available specimens, these plots illustrate the ability to show the OD to ID trends more clearly than simply comparing the ferrite near the OD and ID from tabular data. As an example, Figure 4.1 shows the mean percent ferrite at each depth through the wall thickness on a circumferential-radial cross section of the columnar half of B-527 and is typical of these columnar PISC-III scans, where the ferrite content shows a definite increase from OD to ID, although near the OD the trend in Figure 4.1 shows a slight decrease. As an example of measurements from an equiaxed specimen, the mean percent ferrite at each depth through the wall thickness on an axial-radial cross section of the equiaxed half of B-527 is plotted in Figure 4.2. While this specific scan shows a decreasing trend, this is not representative of data from other equiaxed specimens (Appendix A), which show no consistent trends.

Thus, the data in Table 4.3 from the fine-grid scans do not support observations of Chopra and Sather (1990) that ferrite content is always lower toward the ID of CCSS pipe and would promote columnar grains. Whether decreasing or increasing from OD to ID, the fine-grid scan results do not show a clear correlation to columnar grain structure.

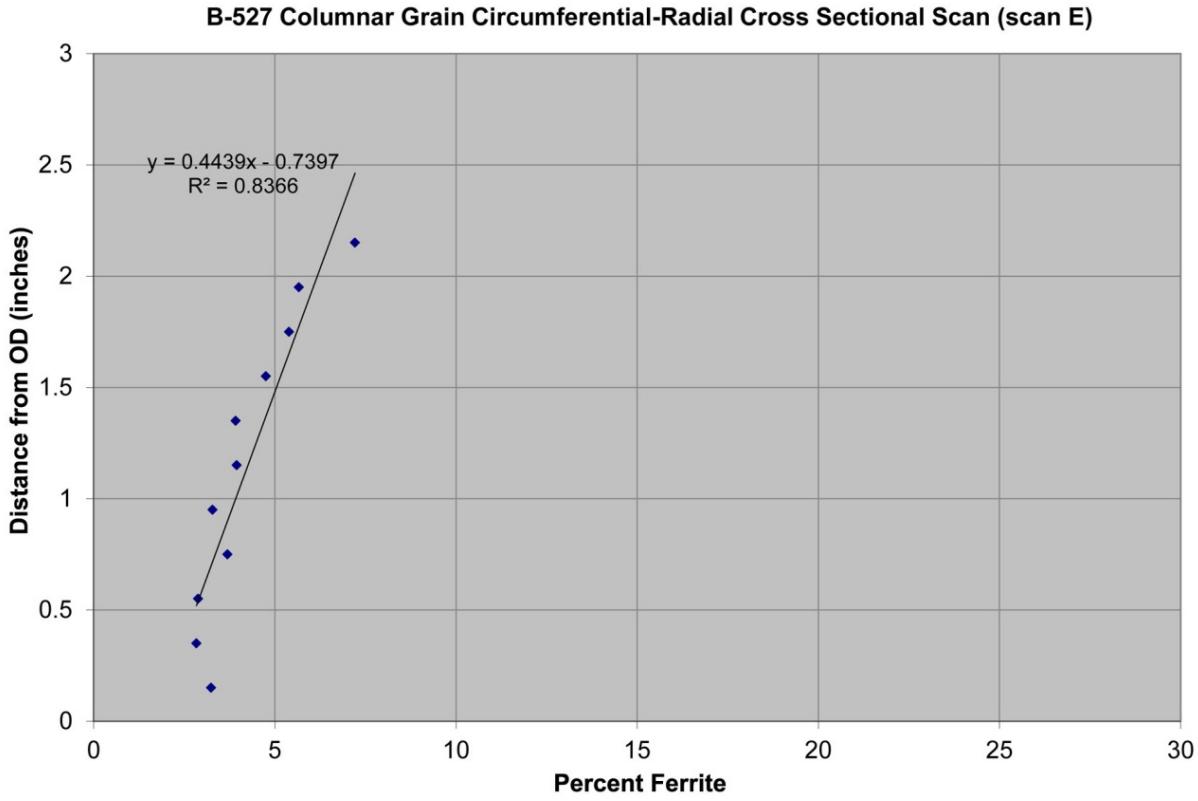

Figure 4.1. B-527 Columnar Grain Circumferential-Radial Cross Sectional Scan (B527C/E)

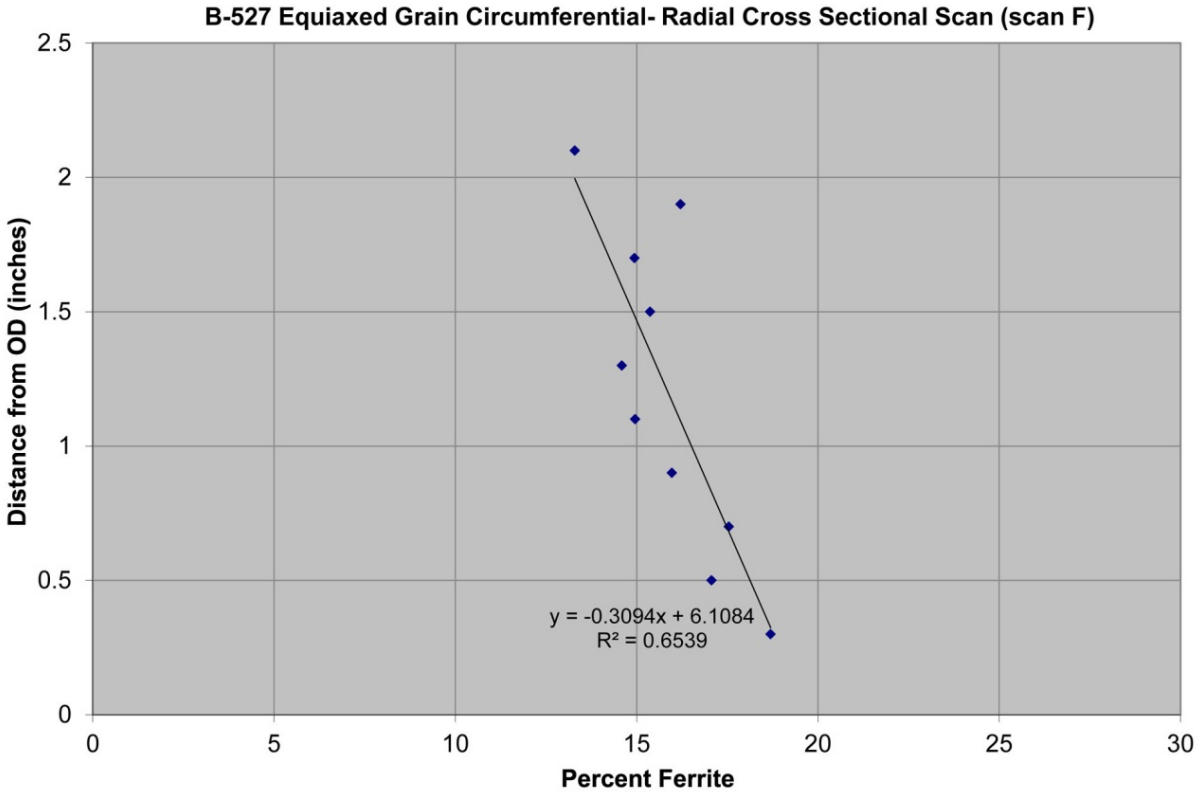

Figure 4.2. B-527 Equiaxed Grain Circumferential-Radial Cross Sectional Scan (B527E/F)

4.2.1.3 Higher Ferrite at the OD

CASS products are considered duplex stainless steels. CASS products having high chromium content initially solidify as primary delta ferrite according to the constant Cr pseudo binary Fe-Ni phase diagram (Figure 2.1). During cooling and in the solid state, when gamma-like elemental concentrations, mainly C and N, are sufficient, some solid-state transformation of delta to gamma occurs, diminishing the delta ferrite content (Massoud et al. 1998).

Initial solidification as primary delta ferrite would imply higher ferrite content at, and near, the OD on CCSS pipe. To assess the ferrite content at, and near, the OD surface, the depth of sampling of the Feritscope needed to be estimated. Using an estimated magnetic permeability (for austenitic stainless steels) and the frequency of the induction probe used in the Feritscope, the estimated depth of sampling of the Feritscope (i.e., the depth of penetration of the induced currents in the specimen) was assessed and found to be on the order of 25.4 mm (1 in.). The breadth, or diameter, of the interrogated volume was found to be on the order of the probe diameter (2.54 mm [0.1 in.]), assuming constant magnetic permeability throughout the volume of the specimen. If this assumption generally holds true, the region sampled by the Feritscope in the radial (wall-thickness) direction would be different depending on whether the measurement is made from the OD surface or on the cross section. Specifically, ferrite measured from the OD surface would likely be averaged over an approximately cylindrical volume that is 25.4 mm in the radial direction, while ferrite measured from the first row (near-OD surface) on the cross section would likely be averaged over an approximately cylindrical region that is about 2.54 mm in the radial direction. This is indicated in Table 4.3, where the “Ferrite at OD” refers to the OD surface scans and would sample several rows into the cross section; “Ferrite Near to OD” refers to the row of cross-sectional scans nearest the OD and would have sampled only a few millimeters into the thickness of the

pipe. Note that, depending on the curvature of the specimen and the need to keep the probe a certain distance away from the edge of the specimen (to avoid erroneous measurements), the distance of the row of cross-sectional scans nearest the OD may vary from a few mm to several mm (see Note (c) in Table 4.3).

The two PWROG specimens fabricated from SFM 156529 show that the "at OD" and "near OD" ferrite concentrations are within the ±3% estimated error. However, of the PISC-III specimens, the B-516 columnar specimen ferrite concentration "at OD" is significantly greater than "near OD"; in combination with the data reported in Section 4.2.1.1, this may be an indication of the columnar side of this specimen being subjected to different processing than the other two PISC-III columnar specimens. However, the equiaxed portions of the PISC-III specimens, for which the foundry and heat origins are unknown, exhibit no consistent trend with respect to relative ferrite concentration "at OD" versus "near OD."

Thus, the results of the fine-grid ferrite scans on these eight specimens do not support the hypothesis that ferrite will be higher at the OD. However, homogenous distribution of ferrite in the axial-radial cross sections is an ideal assumption that may not be realized in practice. Given that the fine-grid ferrite scans are localized measurements, it is possible that the sampling is insufficient to accurately capture the dominant axial trend. This will be addressed further in Section 4.2.2, with the analysis of data from coarse grid scans.

No correlation between the ferrite content at the OD or through thickness could be found with the percent columnar grains.

4.2.1.4 Ferrite Content and Grain Structure

Temple and Ogilvy (1992) claim that the grain structure in CASS with lower ferrite content is likely to tend toward columnar grains. Presumably, the ferrite content to which they referred was the overall content as calculated from the specifications or ladle analysis.

Table 4.3 lists the mean ferrite at the OD (column 5) and the mean ferrite through the wall thickness (column 8) as well as the percent columnar grains (column 4). The mean ferrite for heat SFM 156529 was 24.3% with an average of 57% columnar grains (see Section 4.5.2); the unknown PISC-III columnar heat with 9.2% ferrite averaged 100% columnar; and the unknown PISC-III with 17.1% ferrite averaged zero percent columnar. All of the equiaxed samples were 11.9% ferrite or higher and all of the columnar were 15.6% ferrite or lower (not counting B-516). The mixed grain, including columnar to equiaxed, were higher than 20.9% ferrite. Also, as discussed previously under Section 4.2.1.2, the plots (graphs) of percent ferrite through the wall thickness on the PISC-III equiaxed specimens show patterns and variation of ferrite through the wall of as much as 7%, even though they are 0% columnar. And, each of the columnar PISC-III specimens show similar patterns of ferrite variation through the thickness by nearly 10% even though they are 100% columnar.

Thus, this sample of three heats shows no correlation between measured OD or through-thickness ferrite and percent columnar grain structure and does not support Temple and Ogilvy's hypothesis.

4.2.1.5 Calculated Ferrite Compared to Measured Ferrite on OD Surface

Since, according to Massoud et al. (1998), CASS initially solidifies as primary delta ferrite, it would be reasonable to assume that the OD surface scans, if very shallow, would show higher ferrite than those deeper in the wall. However, since the OD and ID surfaces for all specimens were likely machined after casting and heat treatment, they are likely to have a thin cold worked layer on the surface, about 2.54 mm

(0.10 in.) thick where some of the austenite was converted to ferrite due to plastic deformation. Nevertheless, the Feritscope interrogation depth (see Section 4.2.1.3) was estimated to be about 25.4 mm (1 in.); thus, the effect of machining would have been negligible.

According to Table 3.2, SFM heat 156529 had a calculated percent ferrite (from the ladle analysis) of 18.1 to 18.3 compared to that measured from the OD shown in Table 4.2 of 25.5 and 23.1 (24.3 average). Note that the calculations are based on the assumption that the CASS has undergone post-heat treatment around 1000°C (1850°F) followed by a rapid cooling (Massoud et al. 1998).

The very limited data from the OD scans of one known heat of the CCSS specimens listed in Table 4.3 shows that the measured OD ferrite is higher than the ferrite content calculated from the ladle analysis. Thus, a trend of higher ferrite at the OD than the calculated ferrite content from ladle analysis is indicated for heat SFM 156529.

4.2.1.6 Ferrite Trends and Welds

Hammar and Svensson (1979) noted that, "In austenitic weld deposits a certain ferrite content between 0 and 6%, depending on the grade, can help prevent hot cracking." This implies that low ferrite content would be expected in the CASS weld metal. Note that they were investigating steels with chromium and nickel contents of about 17 and 12 percent, respectively.

The first row of scan E on specimen APE-1 was about 51 mm (2 in.) from the W_{CL} joining the CCSS pipe and SCSS elbow, on the elbow side. The last row of scan E was about 5.4 mm (0.214 in. [0.1 + 0.114 in.]) from the W_{CL}. The average ferrite percent in these rows was 8 and 8.3, respectively, and this represents a decrease in ferrite from the SCSS elbow toward the W_{CL}, likely due to the heat of welding.

Scan C on specimen MPE-6 crossed the W_{CL} joining the CCSS pipe to the SCSS elbow. The average ferrite percent of the first row, which was on the SCSS side, was 16.1, the second row was 15.6, and the third row was 11.0. This would indicate a transition, likely from the SCSS alloy to the weld metal between the second and third rows. The last row on the SCSS side showed an 11.2% ferrite average. Again, the trend exhibits a decrease in ferrite from the SCSS toward the weld.

Scan B on specimen OPE-2 crossed the W_{CL} joining the CCSS pipe to the SCSS elbow. The ferrite in the first row, which was nearest the CCSS alloy, averaged 8.5% and in the last row near the SCSS elbow averaged 26.1%, which indicates a decrease from the SCSS elbow through the weld and on to the CCSS pipe. There was an abrupt decrease in ferrite between row 10 and row 9, from 26.3% to 13.4%, indicating a significant compositional transition.

The first row of scan D on specimen B-516 was on the columnar side, and about 51 mm (2 in.) from the W_{CL} joining the CCSS columnar pipe and the CCSS equiaxed pipe. The last row of scan D was about 7.72 mm (0.304 in.) from the W_{CL}. The average ferrite percent in the first and last rows was 12.5 and 5.3, respectively; this represents a decrease in ferrite from the CCSS columnar pipe toward the W_{CL}, and is consistent with scan E on APE-1.

Thus, in the welded specimens in which ferrite was measured in this investigation, the ferrite content decreases near and through the weld. Nevertheless, the ferrite content in the region of welds and the grain structure in the CCSS pipe does not seem to be related.

4.2.1.7 Fine-Grid Scan Summary Results and Preliminary Conclusions

The results presented in Sections 4.2.1.1–4.2.1.6 are based on the fine-grid scans and only show the ferrite variation in a small region on the specimen. The following conclusions may be drawn based on the fine-grid scan results:

- The variation of Feritscope-measured ferrite from scan to scan and within a scan is within the estimated measurement error on all fine-grid OD surface scans that were at least the distance of the thickness of the CCSS specimen away from a weld. Thus, in order to interrogate more of each specimen, it was determined that the scan grid could be expanded from about 0.5 cm to 2.54 cm (0.2 in. to 1 in.) or more on the OD and ID surfaces of all CCSS specimens available.
- The results of fine-grid Feritscope scans on the limited number of specimens examined and discussed in this section showed little to no correlation between the ferrite content and the grain structure (percent columnar grains).
- The Feritscope-measured ferrite content in specimen B-516 is not consistent with the other two PISC-III specimens, perhaps due to a variation in thermal processing of this specimen.
- The Feritscope ferrite measurements were fairly consistent from specimen to specimen within a heat. Variations in ferrite measurements between different specimens from the same heat may indicate the presence of post-casting thermal and/or mechanical aberrations.
- The Feritscope-measured ferrite shows no clear decreasing trend from OD to ID as predicted in the literature. This could be due to the presence of post-casting thermal and/or mechanical processing.
- The Feritscope-measured ferrite near the welds and in the weld metal tends to be lower than away from the weld in the CCSS pipe.

4.2.2 Coarse-Grid Scans

Because the fine-grid scans (approximately 0.5 cm [0.2 in.] grid) showed that the ferrite content on the OD for CCSS pipe was for the most part homogeneous, larger grids ranging from 2.54 cm to 7.6 cm (1 in. to 3 in.) were applied to subsequent scans. These scans spanned the axial length and circumferential width of the available CCSS specimens.

The ID and OD surface measurements were acquired at identical axial and circumferential positions on a grid with 2.54 cm (1 in.) or larger spacing (coarse grid). Plots of the means along the axial (distance from the weld) and circumferential directions are shown in Appendix B.

A summary of the specimens used in the coarse-grid study, and the mean measured ferrite percent from the OD and ID surfaces of the CCSS pipe is summarized in Table 4.4.

Table 4.4. Summary of Ferrite Scans on the OD and ID of CCSS Pipe on Coarse Grid Scans from Several CASS Specimens Incorporating CCSS Pipe

Specimen	Heat #	OD Mean w/o Weld % Fe (S.D.)	ID Mean w/o Weld % Fe (S.D.)	% Fe OD to ID Trend	Mean OD % Fe Nearest Weld (S.D.)	Weld Affect Dist. (cm; in.)	Average % Fe OD+ID w/o Weld
APE-1	SFM 156529	24.3 (<2.4)	13.6 (<2.4)	Decrease	7.6 (0.6)	<7.8; 3.09	19.0
MPE-6	SFM 156529	23.0 (<1.4)	18.4 (<3.5)	Decrease	10.0 (1.1)	<3.4; 1.35	20.7
ONP-D-2	SFM 156361	21.4 (<1.9)	14.8 (<2.5)	Decrease	11.7 (1.3)	<3.5; 1.36	18.1
ONP-D-5	SFM 156361	11.5* (<0.6)	16.8 (<2.2)	Increase	9.5 (0.4)	<3.5; 1.36	14.2
ONP-3-5	SFM 156361	21.8 (<2.4)	13.3 (<2.2)	Decrease	13.5 (2.4)	~ <7.6; 3.0	17.6
OPE-2	USP C2291A	20.7 (<1.9)	17.5 (<4.0)	Decrease	19.3 (1.1)	~ <7.6; 3.0	19.1
OPE-5	USP C2291A	16.7 (<1.2)	16.7 (<3.0)	None	15.8 (0.8)	~ <7.6; 3.0	16.7
B-510-C		2.8 (<2.3)	7.5 (<1.0)	Increase	11.0 (0.9)	~ <10.2; 4.0	5.2
B-510-E		10.3 (<1.8)	12.2 (<2.2)	Increase	19.0 (2.4)	~ <10.2; 4.0	11.3
B-516-C		15.7 (<1.2)	8.6 (<2.8)	Decrease	10.7 (0.3)	~ <10.2; 4.0	12.2
B-516-E		26.3 (<2.1)	20.5 (<1.5)	Decrease	25.8 (1.1)	~ <10.2; 4.0	23.4
B-527-C		5.2 (<1.1)	7.4 (<2.5)	Decrease	11.7 (1.3)	~ <10.2; 4.0	11.1
B-527-E		10.3 (<1.8)	12.2 (<2.2)	Increase	11.4 (1.7)	~ <10.2; 4.0	11.3
UMich-1		31.0 (<1.8)	15.1 (<4.2)	Decrease	23.0 (5.2)	~>(−17.8; −7), <17.8; 7	23.1
UMich-2		29.9 (<1.8)	16.0 (<3.1)	Decrease	21.1 (4.6)	~>(−17.8; −7), <17.8; 7	23.0
UMich-3		30.2 (<1.3)	16.8 (<2.0)	Decrease	21.7 (3.4)	~>(−17.8; −7), <17.8; 7	23.5
Westinghouse		15.8 (<6.8)	13.0 (<3.0)	Decrease	N. A.	N. A.	14.4
AAD-2 SwRI						N. A.	0.0
IHI Ring		17.6 (<2.9)	19.5 (<1.8)	Increase	N. A.	N. A.	18.6
Manoir Ring		15.8 (<2.0)	13.7 (<2.0)	Decrease	N. A.	N. A.	14.8

The CCSS pipe in APE-1 and MPE-6 was from SFM 156529 and the CCSS pipe in ONP-D-2, ONP-D-5, ONP-3-5, and ONP-3-8 was from SFM 156361 (Ruud et al. 2009, Table 4.4). The CCSS pipe in specimens OPE-2 and OPE-5 was from USP heat number C2291A (Ruud et al. 2009, Table 4.4). The microstructural data are listed in Ruud et al. (2009, Table 4.4). The ladle elemental chemistry of SFM 156529 is shown in Table 3.2; that of USP C2291A was not available.

It had been previously established that one side of the PISC-III CCSS pipe specimens was from SFM heat number 144179 (see Ruud et al. 2009, p. 4.37 #33-47) but, as discussed later in Section 4.3, XRF results did not clearly establish which side, columnar or equiaxed, was from SFM 144179. And, the Feritscope data coarse-grid scans showed the mean columnar OD+ID (Table 4.4) of the PISC-III specimens to range from 5.2% to 12.2% and the equiaxed from 11.3% to 23.5%; while the SFM 144179 ladle calculated ferrite was 16.8%. Thus, there was no clear evidence as to whether SFM 144179 was used in the columnar or equiaxed sides.

The UMich, or University of Michigan, specimens consisted of two CCSS pipes welded together, and no ladle analysis, heat number, or foundry source were available for these specimens. Microstructural information on these specimens was not available at the time of writing of this report.

No ladle analysis, heat number, or foundry source for the Westinghouse Spool and IHI CCSS pipe specimens were available, but the microstructural data are listed in Ruud et al. (2009, Table 4.4). The Manoir ring consists of a single CCSS pipe, from an unknown heat number.

In Table 4.4, the first column lists the identification of each specimen. The second column lists the heat number including the foundry designation. The third and fourth columns list the mean and standard deviation, excluding the weld affected circumferential row scan, of the Feritscope readings on the OD and ID. The standard deviation (S.D.) listed is the higher S.D. of any row (circumferential) set of readings. The fifth column indicates the trend of the mean surface readings through the wall from OD to ID. The sixth column lists the mean of the circumferential OD scan nearest the weld, the seventh column lists the greatest distance from the weld of the affected readings, and the last column lists the average of the OD plus the ID surface readings.

In Table 4.4, the first two specimens listed are from the same SFM heat and the next three specimens are from another SFM heat. The data excluding the weld region ("w/o Weld") from the University of Michigan specimens were taken as the mean ferrite in the rows farthest from the W_{CL}. There was no weld in the Westinghouse Spool, IHI Ring, or the Manoir Ring specimens, thus the "w/o Weld" mean is the mean over the entire specimen. For the University of Michigan specimens, the mean OD % Fe nearest weld is the average from the two rows closest to the weld, and the S.D. is the largest of the S.D. from the two rows. Note that the data from each row are along the same circumference.

Table 4.5 shows that the mean OD + ID Feritscope measured ferrite percent for the CCSS pipe in APE-1 and MPE-6 closely matches the ferrite percent calculated from ladle analysis for SFM 156529.

Table 4.5. Calculated Percent Ferrite from Ladle Analysis and Average Feritscope Measured Percent Ferrite OD+ID

Specimen	Foundry and Heat Number	OD Mean w/o Weld Measured % Fe	Average Measured Mean w/o Weld % Fe OD+ID	Calculated Percent Ferrite from Ladle Analysis
APE-1	SFM 156529	24.3	19.0	18.1
MPE-6	SFM 156529	23.0	20.7	18.1

4.2.2.1 Variation of Ferrite from Specimen to Specimen and Within a Specimen

The CCSS pipe in the Westinghouse Owners Group (PWROG) specimens APE-1 and MPE-6, listed in Tables 4.2 and 4.4, were both from SFM heat number 156529. Thus, they were pieces of the same cast pipe. The mean OD percent ferrite, excluding the weld for the fine-grid scans from these specimens, ranged from 23.1 to 25.5 (Table 4.2) and from the large grid scans from 23.3 to 24.3 (Table 4.4). These are well within the estimated error of 6% reported in Aubrey et al. (1982) for ferrite measurements.

The CCSS pipe in specimens ONP-D-2 thru ONP-3-8 listed in Table 4.4 were from SFM heat number 156361. Thus, they were pieces of the same cast pipe. The mean OD percent ferrite, excluding the heat affected zone (HAZ) for the large grid scans for specimens ONP-D-2 and ONP-3-5, ranged from 21.4 to 21.8 (Table 4.4). However, the percent ferrite for ONP-D-5 was 11.5. Thus, the ONP-D-5 OD readings are significantly lower than from the other specimens from the same CCSS pipe; however, the mean ID

readings are within the estimated error. As noted in the footnote of Table 4.4, the ONP-D-5 OD Feritscope data are unreliable because some of the measurement locations were covered with a label that indicated the specimen identification, but this does not sufficiently account for low ferrite readings from the OD of this CCSS specimen. Perhaps the OD has received a surface thermal or mechanical treatment, including the possibility of a variation on the standard machining of the OD surface.

The CCSS pipe in specimens OPE-2 and OPE-5, listed in Table 4.4, were from USP heat number C2291A. Thus, they were pieces of the same cast pipe. The mean OD percent ferrite, excluding the HAZ for the large grid scans for these specimens, ranged from 16.7 to 20.7 (Table 4.4), which is well within the estimated error.

Either the columnar or the equiaxed half of the CCSS pipe in the PISC-III specimens was from SFM heat number 144179 and the other from an unknown heat. Thus, the columnar sides of all three specimens came from the same heat, and similarly, the equiaxed sides from another heat. The mean OD percent ferrite, excluding the HAZ, for the fine-grid scans for the columnar side of B-510, B-516, and B-527 shown in Table 4.2, were 5.6, 17.0, and 5.1, respectively, and the percent ferrite for the larger grid scans shown in Table 4.4 were 2.8, 15.7, and 5.2, respectively. The ferrite percent values for B-510 and B-527, OD and ID, fine-grid and large grid scans compare well; however, as previously noted in Section 4.2.1.7, the Feritscope-measured ferrite content in specimen B-516 is not consistent with the other two PISC-III specimens. The inconsistency of the percent ferrite in these three, supposedly identical specimens indicates that some may have experienced additional thermal or mechanical treatments after welding. For example, this could have been in the form of a thermal stress relief, grinding, machining, or some other surface treatment.

One other specimen that was included in both the fine-grid scans and the larger grid scans was the IHI Ring. However, only a single through-thickness, circumferential-radial scan was made and cannot be compared with the coarse-grid scans listed in Table 4.4.

The University of Michigan specimens all showed OD ferrite percentages of about 30 ± 1.0 and ID of 16 ± 1.0 from the coarse 25.4 mm (1 in.)-grid scans.

Thus, excluding the weld HAZ and anomalies such as labels, the variation of the Feritscope measurement of ferrite within a specimen are for the most part within the estimated error. Except for the OD of specimen ONP-D-5, the variation of ferrite from specimen to specimen of the PWROG specimens with the same CCSS pipe heat is within estimated error. Also, the University of Michigan specimens show excellent consistency from specimen to specimen and are all likely from the same heat. There is consistency of the coarse-grid Feritscope-measured ferrite in two of the PISC-III specimens.

Thus, some groups of specimens incorporating the same CCSS pipe heat show good consistency from specimen to specimen and others do not, which likely indicates that Feritscope-measured ferrite is very sensitive to measurement conditions and post-casting thermal and mechanical processing. Therefore, Feritscope-measured ferrite content does not appear to be a reliable indicator for grain structure and does not support Temple and Ogilvy's (1992) implication that low ferrite content would indicate columnar grains while high ferrite would indicate equiaxed grains.

4.2.2.2 Ferrite Content Trend OD to ID

As discussed in Section 4.2.1.2, previous studies have indicated a lower ferrite content toward the ID of CCSS pipe (Chopra and Sather 1990). This observation implies a decreasing trend of ferrite content from OD to ID.

As shown in Tables 4.3 and 4.4, the measured percent ferrite decreased from OD to ID in the PWROG specimens incorporating CCSS pipe SFM heat 156529. Those PWROG specimens incorporating SFM 156361 also showed a decrease in the percent ferrite from OD to ID except for ONP-D-5, which showed anomalous OD readings. The PISC-III specimens showed both decrease and increase in the percent ferrite from OD to ID, the University of Michigan all showed decrease, as did the Manoir Ring. The IHI Ring showed an increase in percent ferrite from OD to ID.

Thus, the Feritscope measurement of ferrite showed no consistent trend from OD to ID and did not support the observations of as Chopra and Sather (1990) nor the rationale that slower cooling of the ID would result in lower ferrite at the ID.

4.2.2.3 Calculated Ferrite Content Compared to Feritscope Measurements

The last column of Table 4.4 lists the average Feritscope-measured percent ferrite of the OD plus ID means for each specimen. Table 3.2 lists the measured and calculated percent ferrite using Model #1 as $\%Fe_1$ for the one heat for which ladle analysis was available and identified as incorporated in specimens studied herein.

The average measured OD+ID percent ferrite compares well with that calculated from the ladle analysis for APE-1 and MPE-6. However, a single heat is not statistically sufficient to indicate that Feritscope-measured ferrite offers a means to identify CCSS pipe heats.

4.2.2.4 Ferrite Trends and Welds

Appendix B shows plots of the Feritscope measured percent ferrite versus the axial distance from the weld for all specimens that were studied.

An example of one of the plots from the PWROG specimens is shown in Figure 4.3. It shows a plot of axial Feritscope-measured ferrite (Fe) and calculated Fe (from XRF) for both the OD and ID of specimen APE-1 as an example of the variation of percent ferrite with axial distance from the weld. The measured OD shows a marked decrease, about 15% ferrite, when going from about 28 cm (11 in.) from the W_{CL} to about 25.4 mm (1 in.) from the W_{CL}. All of the PWROG (APE-1 through OPE-2) specimens show such deceases near the weld although not all are as severe. Note that the weld region corresponding to this change varies markedly from specimen to specimen, with some specimens showing large variations in ferrite as great as 12.7 cm (5 in.) from the W_{CL} and some as little as 6.4 cm (2.5 in.) from the W_{CL}. These variations could be caused by changes in the welding process including the number of weld passes, amount of weld metal per pass, thickness of the welded components, size of the components, starting and stopping azimuth, post-weld thermal treatments, and other pertinent factors. At the same time, the measured ferrite percent from the ID does not appear to show such clear changes, with the variation in measured ferrite from the ID near the weld within the estimated error in measurements from the ID.

These data illustrate the sensitivity of the Feritscope measured ferrite to the heat of welding.

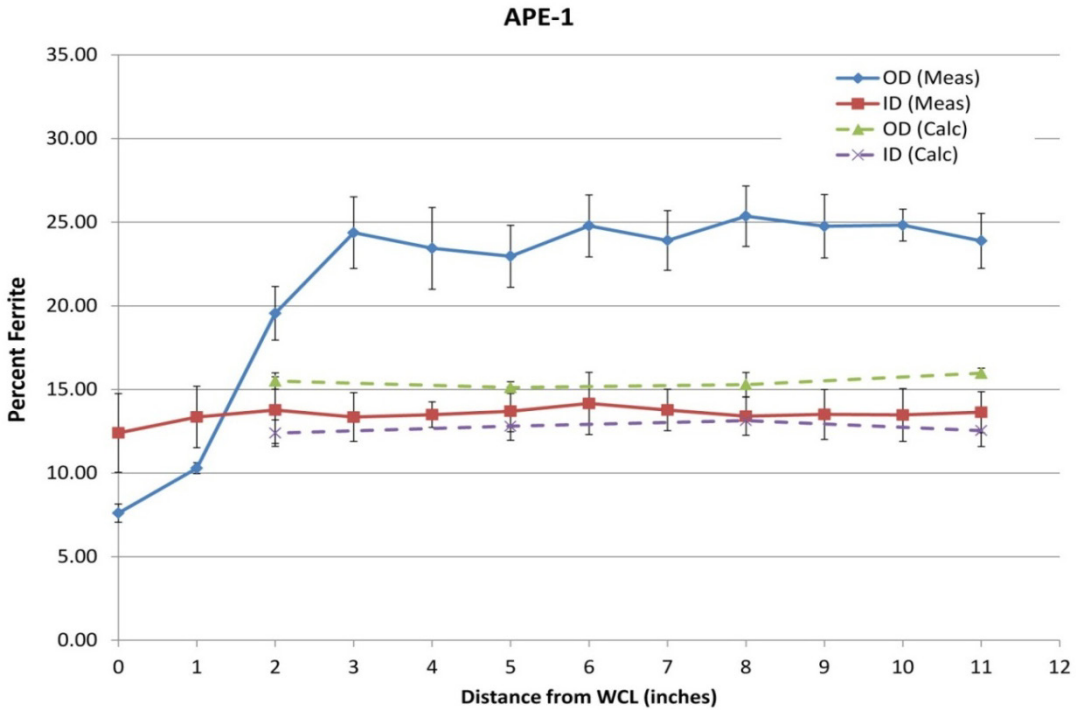

Figure 4.3. Measured and Calculated Ferrite Content in APE-1 CCSS Pipe as a Function of Distance from the Weld Center Line

An example of data from one of the PISC-III specimens is shown in Figure 4.4, and it shows a plot of the axial Feritscope-measured ferrite (Fe) and calculated Fe (from XRF) for both the OD and ID of specimen B-527-C. Again the OD shows a decrease in measured ferrite toward the weld and B-527-E, B-516-C, and B-516-C showed similar trends; however, B-510-C and B-510-E showed an increase. The IDs all showed a negligible change in ferrite toward the welds.

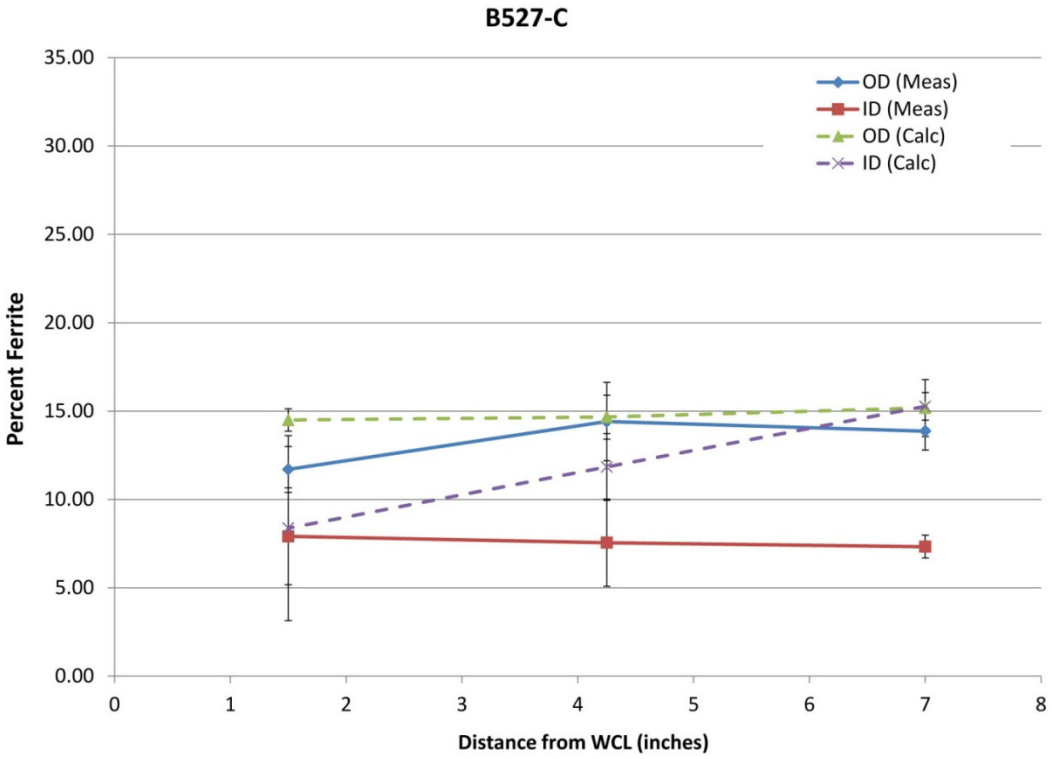

Figure 4.4. Measured and Calculated Ferrite Content in B-527 (columnar side) CCSS Pipe as a Function of Distance from the Weld Center Line

An example of a plot from one of the UMich specimens is shown in Figure 4.5 and it shows a plot of the axial measured ferrite (Fe) and calculated Fe (from XRF) for both the OD and ID of specimen UMich-1. All three of the UMich specimens show similar plots with the OD measured percent ferrite decreasing toward the weld and a negligible change at the ID.

Thus, for the most part, the PWROG and UMich specimens showed that the measured percent ferrite tended to decrease near the weld; however, the calculated percent ferrite based on XRF elemental content was generally constant.

These plots of the change in percent ferrite vs. distance from the weld along the axis of the pipe, as measured by the Feritscope, compared to the percent ferrite calculated from XRF elemental content shows that Feritscope-measured ferrite is not a reliable indicator of as-cast ferrite. The fact that the elemental content is nearly constant along the pipe axis shows that the Feritscope-measured ferrite change is likely not due to composition variation (see Section 4.2.1.1) but may be the result of post-casting thermal or mechanical treatment.

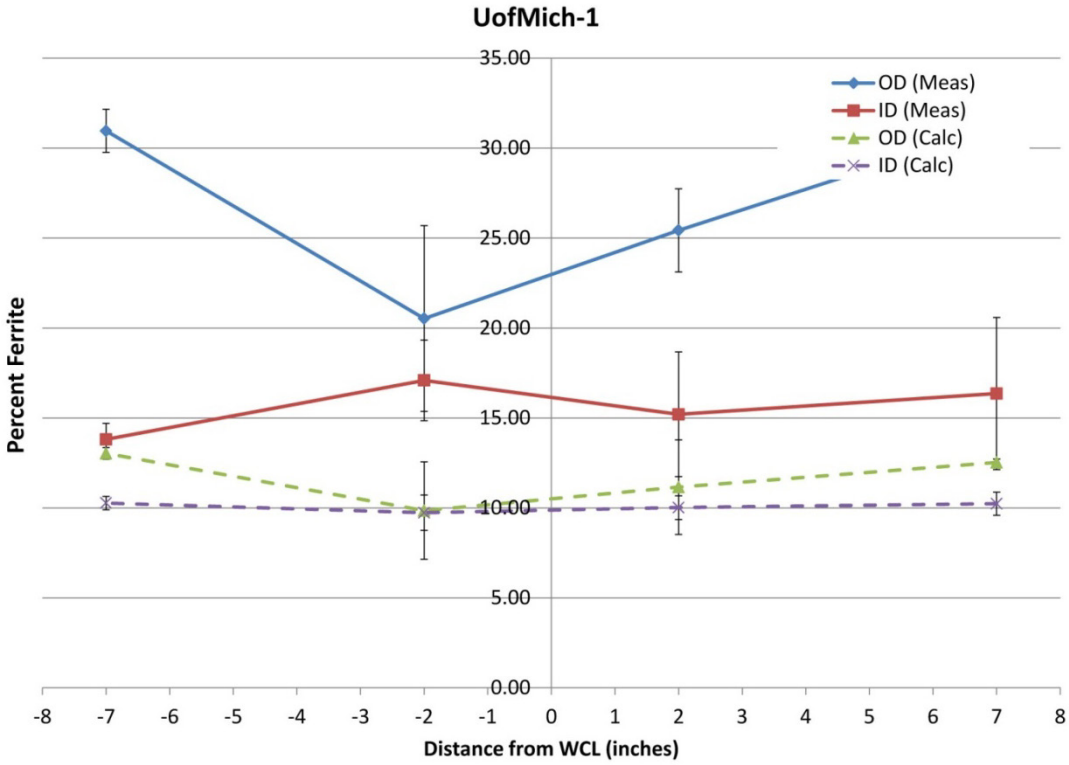

Figure 4.5. Measured and Calculated Ferrite Content in UMich-1 CCSS Pipe as a Function of Distance from the Weld Center Line

4.2.2.5 Coarse Grid Summary Results and Preliminary Conclusions

The following preliminary conclusions may be drawn, based on the coarse grid results:

- Feritscope-measured ferrite content is not a reliable indicator of grain structure (percent columnar grains).
- Feritscope-measured ferrite did not support Temple and Ogilvy's (1992) implication that low ferrite content would indicate columnar grains while high ferrite would indicate equiaxed grains.
- Feritscope-measured ferrite content showed no consistent trend OD to ID and thus did not support the observations of Chopra and Sather (1990) nor the rationale that slower cooling of the ID would result in lower ferrite at the ID.
- Feritscope-measured ferrite content is very sensitive to the heat of welding and is likely sensitive to any post-casting thermal or mechanical processing.

4.3 XRF Measurements

The mean percent and standard deviation of Mn, Cr, Ni, and Mo at the OD and ID surface of CCSS pipe on coarse-grid scans from the CASS specimens incorporating CCSS pipe that were studied are summarized in Table 4.6. The values listed are unrefined except for the omission of measurements that were outliers, as defined in Section 3.3.

Table 4.6. Unrefined Mean Elemental Content by XRF and Mean XRF Calculated and Feritscope-Measured Ferrite from CCSS Pipe[(a)]

Specimen	Heat	Mean % Mn	S.D. Mn	Mean % Cr	S.D. Cr	Mean % Ni	S.D. Ni	Mean % Mo**	S.D. Mo	Mean Calc % Ferrite[(b)]	Mean Meas % Ferrite w/o Weld	Calc Ferrite minus Meas w/o Weld
APE-1 OD	SFM 156529	0.566	0.023	20.276	0.052	8.122	0.048	0.003	0.002	15.5	24.3	−8.8
APE-1 ID	SFM 156529	0.542	0.017	20.223	0.053	8.510	0.101	0.006	0.002	12.7	13.6	−0.9
MPE-6 OD	SFM 156529	0.559	0.022	20.363	0.054	8.183	0.033	0.004	0.001	15.6	23.0	−7.4
MPE-6 ID	SFM 156529	0.537	0.036	20.198	0.072	8.204	0.134	0.004	0.002	14.5	18.4	−3.9
Ladle Analysis	SFM 156529	0.66		20.0		8.3		0.5*		16.2		0.0
ONP-D-2 OD	SFM 156361	0.435	0.025	20.837	0.051	8.36	0.051	0.000	0.000	11.0	21.4	−10.4
ONP-D-2 ID	SFM 156361	0.445	0.032	20.811	0.283	8.547	0.588	0.000	0.000	11.4	14.8	−3.4
ONP-D-5 OD	SFM 156361	0.451	0.025	20.800	0.184	8.401	0.315	0.000	0.000	12.0	11.5*	0.5
ONP-D-5 ID	SFM 156361	0.433	0.028	20.842	0.039	8.714	0.127	0.000	0.000	10.5	16.8	−6.3
ONP-3-5 OD	SFM 156361	0.423	0.025	20.947	0.076	8.363	0.080	0.000	0.000	12.8	21.8	−9.0
ONP-3-5 ID	SFM 156361	0.448	0.024	20.851	0.074	8.675	0.135	0.000	0.000	10.7	13.3	−2.6
ONP-3-8 OD	SFM 156361	0.446	0.035	20.883	0.026	8.315	0.049	0.000	0.000	12.8	?	0.0
ONP-3-8 ID	SFM156361	0.452	0.028	20.885	0.041	8.862	0.147	0.000	0.000	10.0	?	0.0
OPE-2 OD	USPC2291A	0.905	0.020	20.195	0.059	8.228	0.079	0.561	0.008	13.0	20.7	−7.7
OPE-2 ID	USP C2291A	0.862	0.039	20.141	0.091	8.461	0.240	0.570	0.016	11.6	17.5	−5.9
OPE-5 OD	USP C2291A	0.903	0.025	20.264	0.037	8.316	0.056	0.562	0.007	12.8	16.7	−3.9
OPE-5 ID	USP C2291A	0.847	0.024	20.245	0.066	8.455	0.163	0.567	0.010	12.1	16.7	−4.6
B-510-C OD		0.582	0.162	20.768	0.393	7.865	0.053	0.363	0.006	17.5	2.8	14.7
B-510-C ID		0.926	0.124	19.87	0.565	7.770	0.771	0.382	0.014	13.4	7.5	5.9
B-510-E OD		0.394	0.068	19.787	0.407	8.269	0.129	0.000	0.000	8.5	10.3	−1.8
B-510-E ID		0.636	0.077	19.458	0.553	8.259	0.629	0.000	0.000	7.9	12.2	−4.4
B-516-C OD		0.804	0.035	21.117	0.054	7.835	0.075	0.365	0.003	19.6	15.7	3.9
B-516-C ID		0.885	0.137	20.922	0.341	8.447	0.250	0.339	0.088	14.3	8.6	5.7
B-516-E OD		0.535	0.030	20.263	0.092	8.306	0.106	0.000	0.000	10.0	26.3	−16.3

Table 4.6. (continued)

Specimen	Heat	Mean % Mn	S.D. Mn	Mean % Cr	S.D. Cr	Mean % Ni	S.D. Ni	Mean % Mo**	S.D. Mo	Mean Calc % Ferrite[(b)]	Mean Meas % Ferrite w/o Weld	Calc Ferrite minus Meas w/o Weld
B-516-E ID		0.551	0.026	20.207	0.039	8.568	0.079	0.000	0.000	8.6	20.5	−11.9
B-527-C OD		0.642	0.064	20.430	0.271	7.971	0.092	0.367	0.004	14.8	14.8	0.0
B-527-C ID		0.738	0.043	20.593	0.347	8.309	0.086	00.376	0.009	13.0	7.4	5.6
B-527-E OD		0.495	0.043	19.516	0.264	8.620	0.243	0.000	0.000	6.1	10.3	−4.2
B-527-E ID		0.565	0.031	19.240	0.233	9.187	0.347	0.000	0.000	4.1	12.2	−8.1
LadleAnalysis	SFM144179	0.68		20.42		8.58		0.5		7.7		0.0
UMich-1 OD		0.709	0.022	20.295	0.037	7.821	0.053	0.020	0.003	12.8	31.0	18.2
UMich-1 ID		0.738	0.029	20.245	0.048	8.289	0.134	0.023	0.002	10.1	15.1	−5.0
UMich-2 OD		0.707	0.022	20.261	0.039	7.813	0.049	0.021	0.000	12.7	29.9	−17.2
UMich-2 ID		0.735	0.030	20.269	0.067	8.310	0.152	0.024	0.003	10.1	16.0	−5.9
UMich-3 OD		0.718	0.026	20.250	0.020	8.183	0.063	0.018	0.002	13.7	30.2	−16.5
UMich-3 ID		0.725	0.023	20.262	0.042	8.318	0.198	0.023	0.002	10.0	16.8	−6.8
IHIRing OD		0.53	0.021	20.289	0.082	9.541	0.061	2.878	0.016	19.9	17.6	2.3
IHIRing ID		0.673	0.070	20.203	0.068	9.714	0.180	2.906	0.041	18.5	19.5	−1.0
Manoir Ring OD		0.697	0.032	20.470	0.042	9.139	0.078	0.139	0.003	7.8	15.8	−8.0
Manoir Ring ID		0.679	0.031	20.374	0.080	9.437	0.121	0.144	0.002	6.6	13.7	−7.1
Westinghouse Ring OD		0.681	0.025	20.545	0.077	9.833	0.096	2.926	0.016	19.6	15.8	3.8
Westinghouse Ring ID		0.669	0.061	20.262	0.674	9.835	0.234	3.057	0.293	19.5	13.0	6.5

*Assumed.

**Negative Mo readings were assumed to be zero.

(a) Note: Some individual values were found to be obviously anomalous and were thus not included in the calculation of the unrefined mean and standard deviation (see Section 3.3).

(b) The #1 Model for calculating ferrite content reported in Table 3.2 was used and the percentages of Mo and N were assumed as 0.5 and 0.04, respectively. For C the ladle analysis was used when available, and when not it was assumed as 0.08 (the maximum allowable for CF8, CF8A, and CF8M). All mean calculated percent ferrite use unrefined XRF elemental content (see Section 3.3) except for the ladle analyses.

The ID and OD XRF measurements were made at the same axial and circumferential positions on grids with 1 in. or larger spacings (Section 4.2.2) as the ferrite measurements using the Feritscope. It would have also been beneficial to measure Si, P, and S, but XRF analysis for these elements requires an upgraded analyzer, which was not available. Also, analysis for N and C would have been important but these elements typically cannot be measured by XRF. In an attempt to identify whether the columnar or equiaxed side of the PISC-III specimens were from heat SFM 144174, Table 4.7 was developed. It lists the unrefined mean XRF-determined elemental content pertinent to the calculation of ferrite of the four key elements analyzed, and the calculated ferrite from the OD and ID of the three PISC-III specimens examined herein. Also listed in the table are the percent content of the four elements and the calculated ferrite from the ladle chemistry. Comparison of the ladle to XRF in Table 4.7 did not clearly identify SFM 144179 as the source for either the columnar or equiaxed pipe incorporated in the PISC-III specimens.

Thus, the data from Feritscope-measured ferrite, ferrite calculated from XRF analysis, or XRF elemental analysis did not clearly identify SFM 144179 as the source for either the columnar or equiaxed side of the three PISC-III specimens.

Also included in this study was a 937 mm OD CCSS pipe identified as Manoir, a vintage CASS specimen obtained from the Manoir foundry in France. Both Feritscope and XRF measurements were made on this pipe section. A comparison of the XRF-measured elemental composition with the elemental composition data provided in Manior heat number Z1257 shows significant differences. The XRF data from the Manoir pipe shows a mean Mo (OD+ID) content of about 0.14% while the ladle analysis for heat number Z1257 (935 mm) is 2.52% Mo. Also, the ladle analysis calculated ferrite for the 935 mm pipe is 21.2% and that calculated from the OD+ID XRF from the 937 mm pipe is 7.2%. Finally, the photographs of CCSS pipe specimens obtained for this project include two that show a “French MCC 10” pipe segment.

Based on these discrepancies, it was assumed that the specimen identified as Manoir in this study was not from the Manoir heat number Z1257.

4.3.1 Coarse-Grid XRF Scans

4.3.1.1 Variation of Elemental Content and Calculated Ferrite within a Specimen and from Specimen to Specimen from the Same Heat

As indicated earlier, Table 4.6 summarizes the data in terms of the mean and standard deviation of the Mn, Cr, Ni, and Mo elemental content and the calculated ferrite. The estimated error for the XRF measurement of each of four elements is summarized in Table 4.8. Note that for the most part the OD XRF results are featured because the OD is more representative of the as-cast condition as more material was usually removed by machining for the ID than the OD due to the rough as-cast condition of the ID (Ruud et al. 2009, page I.2, paragraph 2).

Table 4.7. Refined XRF and Ladle Mean Elemental Content[(a)] of B-Series Columnar and Equiaxed Compared to Heat SFM 144179

Specimen	Mean % Mn	Mean % Cr	Mean % Ni	Mean % Mo	Cr Equiv	Ni Equiv	Cr Equiv/ Ni Equiv	% Ferrite[(c)]
B-510 Col/OD	0.582	20.768	7.865	0.3625	16.7	12.4	1.35	26.1
B-510 Col/ ID	0.893	19.953	7.998	0.3500	15.9	12.6	1.26	18.5
B-516 Col/OD	0.804	21.117	7.835	0.3648	17.0	12.4	1.37	29.1
B-516 Col/ID	0.817	21.085	8.435	0.3250	17.0	13.0	1.30	22.2
B-527 Col/OD	0.623	20.366	7.962	0.3676	16.3	12.5	1.30	22.0
B-527 Col/ID	0.738	20.893	8.214	0.3800	16.8	12.8	1.32	23.5
Average Columnar	0.743	20.697	8.052	0.3583	16.6	12.6	1.32	23.6
Ladle[(b)] Analysis	0.680	20.42	8.580	0.5000	16.6	13.6	1.22	15.1
Average Equiaxed	0.518	19.7736	8.484	0.0000	15.3	13.0	1.17	12.1
B-510 Equ/OD	0.392	19.788	8.274	0.0000	15.3	12.8	1.19	13.3
B-510 Equ/ID	0.613	19.126	8.697	0.0000	14.6	13.2	1.10	8.0
B-516 Equ/OD	0.535	20.263	8.306	0.0000	15.8	12.8	1.23	15.7
B-516 Equ/ID	0.551	20.207	8.568	0.0000	15.7	13.1	1.20	13.6
B-527 Equ/OD	0.497	19.484	8.576	0.0000	15.0	13.1	1.14	10.1
B-527 Equ/ID	0.561	19.287	9.229	0.0000	14.8	13.8	1.07	6.5

(a) The mean elemental percent data was refined by omitting those values that were greater than one standard deviation from the mean, and the standard deviation was greater than the percent elemental error such as that listed in Table 4.8 and Table 3.3 for example.

(b) Ladle analysis is for Heat SFM 144179.

(c) – The number 1 model for predicting ferrite content according to Aubrey et al. (1982): Cr equivalent = Cr_e = %Cr + 1.21 %Mo + 0.48 %Si − 4.99 and Ni equivalent = Ni_e = %Ni + 0.11 %Mn − 0.0086 $\%Mn^2$ + 18.4 %N + 24.5 %C + 2.77. Ferrite content = $\%Fe_1 = 100.3 \times (Cr_e/Ni_e)^2 - 170.72\ (Cr_e/Ni_e) + 74.22$. Note these equations are based upon Hull's equivalent factors (Aubrey et al. 1982).

– Value of Mo was assumed to be 0.5 for the ladle analysis.

– C was assumed as 0.04, N as 0.04, Si as 1.0 for CF8 and CF8A; these values compare well with the mean C, N, and Si values shown for the heats listed in Table 3.3 (i.e., 0.037, 0.039, and 1.1, respectively) (EPRI 1991). Note the high values reported for N in two of the heats was questionable and thus not included in the calculation of the means. Note that the previous tables in this report made the same assumptions except for C, which was assumed as 0.08%.

Table 4.8. Unrefined Mean XRF Elemental OD Content[(a)] and Estimated[(b)] Measurement Error for Specimens of the Same Heat

Specimens	Heat	OD Mean % Mn	% Mn Error ±	OD Mean % Cr	% Cr Error ±	OD Mean % Ni	% Ni Error ±	OD Mean % Mo	% Mo Error ±
APE-1	SFM 156529	0.566	0.052	20.276	0.083	8.122	0.083	0.003	<0.01
MPE-6	SFM 156529	0.559	0.052	20.363	0.083	8.183	0.083	0.004	<0.01
Mean	***S.D.***	***0.5625***	***0.005***	***20.3195***	***0.06152***	***8.1525***	***0.04313***	***0.0035***	***0.001***
LadleAnalysis	SFM156529	0.66		20.00		8.3		N.A.	
ONP-D-2	SFM156361	0.435	0.052	20.837	0.085	8.360	0.085	0.000	<0.01
ONP-D-5	SFM156361	0.451	0.052	20.800	0.085	8.401	0.085	0.000	<0.01
ONP-3-5	SFM156361	0.423	0.052	20.947	0.085	8.363	0.085	0.000	<0.01
ONP-3-8	SFM156361	0.446	0.052	20.883	0.085	8.315	0.085	0.000	<0.01
Mean	***S.D.***	***0.4405***	***0.0078***	***20.867***	***0.063***	***8.360***	***0.035***	***0***	***0***
OPE-2	USP C2291A	0.905	0.055	20.195	0.085	8.228	0.085	0.561	<0.01
OPE-5	USP C2291A	0.903	0.055	20.264	0.082	8.316	0.083	0.562	<0.01
Mean	***S.D.***	***0.904***	***0.0014***	***20.2295***	***0.04879***	***8.272***	***0.06223***	***0.5615***	***0.001***
B-510-C		0.582	0.051	20.768	0.085	7.865	0.085	0.363	<0.01
B-516-C		0.804	0.052	21.117	0.083	7.835	0.080	0.365	<0.01
B-527-C		0.642	0.051	20.430	0.082	7.971	0.081	0.367	<0.01
Mean	***S.D.***	***0.676***	***0.115***	***20.772***	***0.344***	***7.810***	***0.071***	***0.365***	***0.002***
Ladle Analysis	SFM 144179	0.68		20.42		8.58		N.A.	
B-510-E	Unknown	0.394	0.051	19.787	0.079	8.269	0.084	0.000	<0.01
B-516-E	Unknown	0.535	0.051	20.263	0.081	8.306	0.084	0.000	<0.01
B-527-E	Unknown	0.495	0.052	19.516	0.079	8.620	0.085	0.000	<0.01
Mean	***S.D.***	***0.4445***	***0.07142***	***19.6515***	***0.191626***	***8.4445***	***0.248194***	***0***	***0***
UMich-1	Unknown	0.709	0.052	20.295	0.081	7.821	0.084	0.020	<0.01
UMich-2	Unknown	0.707	0.054	20.261	0.081	7.813	0.081	0.021	<0.01
UMich-3	Unknown	0.718	0.053	20.250	0.081	8.183	0.083	0.018	<0.01
Mean	***S.D.***	***0.738***	***0.045***	***20.269***	***0.023***	***7.939***	***0.211***	***0.020***	***0.002***
IHIRing		0.530	0.046	20.289	0.085	9.541	0.089	2.878	0.02
Manoir Ring		0.697	0.052	20.470	0.084	9.139	0.089	0.139	<0.01
Westinghouse Ring		0.681	0.046	20.545	0.086	9.833	0.089	2.926	0.02

(a) Note: Measurement values that were outliers (as described in the text) were excluded in the calculation of the mean (see Section 3.3).
(b) XRF instrument measurement error estimated from information recorded by the XRF instrument during the measurement process.

The standard deviation of OD XRF measurements within each PWROG specimen (with the exception of outliers described earlier) was used in the evaluation of the uniformity of elemental content within the specimens. The standard deviation [summarized in Table 4.6 (columns 4, 6, 8, and 10)] was compared to the ±% elemental error of four elements listed in Table 4.8 (columns 4, 6, 8, and 10). The comparison indicated that, with one exception, the standard deviation of all XRF readings on the OD are less than or equal to the XRF percent error (±% error) for each element. The exception appears to be specimen ONP-D-5 (from heat SFM 156361), where the standard deviations for Cr and Ni are outside the XRF percent error (±% error).

Thus, the elemental content within the PWROG specimens as measured by XRF may be considered to be uniform.

To compare the XRF elemental results from different PWROG specimens from the same heat, the mean and standard deviation of the four elements from specimens of the same heat were calculated and compared to the percent error of each specimen and element in Table 4.8. For the two CCSS specimens incorporating SFM 156529, the average of the four elements listed for the two specimens (Table 4.8) were 0.5625, 20.3195, 8.1525, and 0.0035, and the standard deviations were 0.005, 0.06125, 0.04313, and 0.001, respectively. All of the standard deviations for the mean of the two pipes were less than the percent error for the elements reported. Comparison of the four ONP specimens from SFM 156361 and the two OPE pipe from USP C2291A also showed excellent agreement.

Thus, comparison of the measured elemental content of CCSS pipe from these different PWROG specimens verified that the CCSS pipes were likely from the same heat.

For evaluation of the uniformity of elemental content within the columnar PISC-III specimens, the standard deviation of all of the OD XRF measurements within each columnar grained PISC-III specimen (Table 4.6) was compared to the ±% elemental error of four elements listed in Table 4.8 as follows: The standard deviation (Table 4.6; columns 4, 6, 8, and 10) of the measurements from the OD of the CCSS pipe in two of the columnar grained PISC-III-C specimens, both from the same heat, are all nearly equal to or less than the XRF ±% error for each element (Table 4.8; columns 4, 6, 8, and 10). However, the standard deviation of the OD measurements for Mn and Cr were much higher for B-510C than the estimated percent XRF error. The XRF data for B-510C shows a large variability in the measurements at different locations and thus measurement difficulties could be the explanation for the large standard deviation of XRF measurements on this specimen. Also, the standard deviation of all of the OD Cr XRF measurements in B-527C was nearly four times higher than the estimated error, but no explanation for the large standard deviation is apparent.

Thus, the elemental uniformity within the columnar side of the PISC-III specimens as measured by XRF was poor.

For evaluation of the elemental uniformity within the equiaxed PISC-III specimens, the standard deviation of all of the OD XRF measurements within each equiaxed PISC-III specimen (Table 4.6) was compared to the ±% elemental error of four elements listed in Table 4.8 as follows: The XRF reading for Ni in specimen B-510E is 1.5 times higher than the ±% error indicated in Table 4.8 but only one anomalous reading was apparent for Ni. For specimen B-527E, the standard deviation for both Cr and Ni were significantly larger than the percent ± error shown in Table 4.8.

Thus, the elemental uniformity within the equiaxed side of the PISC-III specimens as measured by XRF was poor.

To compare the XRF elemental results from different PISC-III specimens from the same heat, the mean and standard deviation of the four elements from specimens of the same heat were calculated and compared to the percent error for each specimen and element in Table 4.8. The standard deviations for Cr and Ni listed in Table 4.8 for both the columnar and the equiaxed PISC-III were much higher that the percent XRF ±% error.

Thus, comparing the elemental uniformity of different columnar and equiaxed PISC-III specimens from the same heat as measured by XRF showed poor results.

As described in Section 4.2.1.1, one of either the columnar or the equiaxed halves of the CCSS pipes in the PISC-III specimens was from SFM heat number 144179, while the other was from an unknown heat. Feritscope ferrite measurements previously described were not able to establish whether SFM 144179 was the columnar or equiaxed material. It was hoped that the XRF elemental or calculated ferrite data could establish which material was from SFM 144179. However, since the PISC-III XRF data showed poor uniformity, the data were more closely examined for statistical variability. For a more precise comparison of the XRF data and calculated ferrite, refinement of the data from the PISC-III specimens was performed (see Section 3.3). This refinement consisted of omitting values that were greater than one standard deviation from the mean, and the standard deviation was greater than the percent elemental errors listed in Table 4.8. Table 4.7 is the result and it lists the mean refined elemental content for the columnar and equiaxed sides of the PISC-III specimens, the average of the OD plus ID columnar and equiaxed sides, as well as the ladle analysis from SFM 144179. Comparison of the average columnar and equiaxed sides with the ladle analysis does not clearly establish which side originated from the SFM 144179 heat.

For evaluation of the elemental uniformity within the UMich specimens, the standard deviation of all of the OD XRF measurements within each UMich specimen (Table 4.6) was compared to the ±% elemental error of four elements listed in Table 4.8 as follows: The standard deviation (Table 4.6; columns 4, 6, 8, and 10) of the OD from the CCSS pipe in UMich 1, 2, and 3 are all less than the XRF ±% error for each element Table 4.8; columns 4, 6, 8, and 10).

Thus, the XRF results from these UMich CCSS pipe shows that, elementally, they are homogeneous.

To compare the XRF elemental results from the three UMich specimens all assumed to be from the same heat, the mean and standard deviation of the four elements were calculated and compared to the percent error for each specimen and element in Table 4.8. The standard deviations for Cr and Ni listed in Table 4.8 are slightly higher that the percent XRF ± error.

Thus, comparison of the measured elemental content of the CCSS pipe from different UMich specimens verified that the CCSS pipe specimens were likely from the same heat.

For evaluation of the elemental uniformity within a specimen, the standard deviation of all of the OD XRF measurements within the IHI Ring (Table 4.6) was compared to the ±% elemental error of four elements listed in Table 4.8 as follows: The standard deviation (Table 4.6; columns 4, 6, 8, and 10) of the OD from this ring section of a CCSS pipe are all nearly equal or less than the XRF ±% error for each element (Table 4.8; columns 4, 6, 8, and 10).

Thus, the IHI Ring is elementally homogeneous.

For comparison of the elemental uniformity within a specimen, the standard deviation of all of the OD XRF measurements within the Manoir Ring (Table 4.6) was compared to the ±% elemental error of four elements listed in Table 4.8 as follows: The standard deviation (Table 4.6; columns 4, 6, 8, and 10) of the OD from this ring section of a CCSS pipe are all less than the XRF ±% error for each element (Table 4.8; columns 4, 6, 8, and 10).

Thus, the Manoir Ring is elementally homogeneous.

For evaluation of the elemental uniformity within a specimen, the standard deviation of all of the OD XRF measurements within the Westinghouse Ring (Table 4.6) was compared to the ±% elemental error of four elements listed in Table 4.8 as follows: The standard deviation (Table 4.6; columns 4, 6, 8, and 10) of the OD from this ring section of a CCSS pipe are all nearly equal or less than the XRF ±% error for each element Table 4.8; columns 4, 6, 8, and 10).

Thus, the Westinghouse Ring is elementally homogeneous.

Figure 4.6 is an example of the average XRF-measured nickel content along the axis of the pipe from specimen APE-1. The standard deviations of the circumferentially-averaged data are also shown with error bars. Note that the ID nickel content is higher as predicted by Chopra and Sather (1990) (see Section 4.2.2.2) and that when considering the error bars the nickel content is essentially constant. This trend was seen to hold for most of the specimens examined in this study, with the variations in the elemental data for the PWROG specimens along the axis largely within the standard deviation of the measurements. The exception is ONP-D-5, where the XRF-measured elemental content appears to be inhomogeneous. Similarly, the variations in the elemental data for the PISC-III specimens are largely within the standard deviation of the measurements**.** However B-510-C Mn and Cr show larger standard deviations than the other two. Likewise, with the exception of UMich-3 Mn OD, UMich-1 Cr ID, UMich-2 Ni OD, all of the UMich specimens appear to be elementally homogeneous within the scatter of measurement. However, all three of the UMich specimens seem to show high Mo near the weld on one side. The authors have no explanation for this trend.

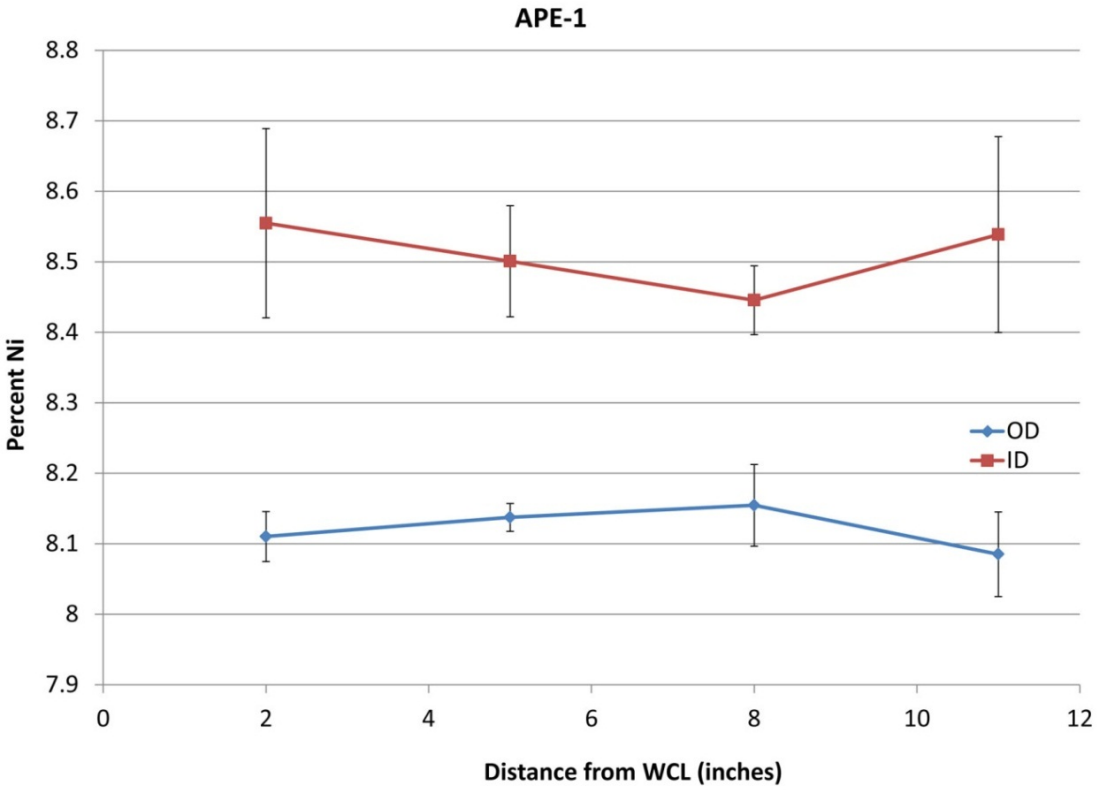

Figure 4.6. Plot of XRF-measured Nickel Content Along the Axis of the Pipe as Function of Distance from the Weld for Specimen APE-1

4.3.1.2 Elemental Content and Calculated Ferrite OD to ID

Table 4.6 lists the mean OD and ID content for the four elements measured by XRF as well as the calculated ferrite from the XRF values.

As discussed earlier, Chopra and Sather (1990) observed that ferrite content is always lower toward the ID of CCSS pipe, apparently related to the nickel content; that is, enrichment of nickel in the liquidus near the ID, which would promote columnar grains. Their observation implies a decreasing trend of ferrite content from OD to ID. The PWROG specimens incorporating heats SFM 156529, SFM 156361, and USP C2291C listed in Table 4.6 show that the Ni content at the ID is higher than at the OD confirming Chopra and Sather's (1990) observation that Ni is higher at the ID. And, all the other specimens listed in Table 4.6 show the same trend reinforcing the confirmation of Chopra and Sather's observations.

CASS are considered duplex stainless steels and having high chromium content, initially solidify as a primary delta ferrite according to the constant Cr (18%) pseudo binary Fe-Ni phase diagram (Figure 2.1). During cooling and in the solid state, when gamma-like elemental concentrations (mainly C and N) are sufficient, some solid-state transformation of delta to gamma occurs, diminishing the delta ferrite content (Massoud et al. 1998). The calculated ferrite trend from OD to ID based upon XRF elemental analysis shows that ferrite content is higher at the OD than at the ID, indicating that the material at the OD tended to have a higher concentration of elements solidifying as ferrite.

The CCSS pipe in all but two of the specimens showed nearly equal Cr at the OD and ID surfaces (MPE-6 and B-510C were exceptions) and less than half of the specimens containing Mo showed the highest content at the ID. According to the ASM Handbook (1980, pg. 96), ferrite (delta) content is controlled by composition, and chromium, molybdenum, and silicon promote its formation.

Also, considering that in CCSS pipe casting processes, the ID cools slower than the OD, the ID would be expected to have a lower percent ferrite. This is because the slower cooling material remains at a temperature for a longer time where ferrite tends to transform to austenite, thus allowing more transformation. However, the lower ferrite trend at the ID as measured by Feritscope should have been intensified by the heat treatment previously mentioned in Section 3.1.4. Nevertheless, as discussed in Section 4.2.2.2, the Feritscope measurements did not show a consistent OD to ID ferrite trend.

Nevertheless, all of the specimens show higher Ni at the ID and lower XRF-calculated ferrite, as cited in the literature (Chopra and Sather 1990) and reflecting the composition and casting process parameters in existence at casting.

4.3.1.3 Comparison of Measured Ferrite Content to Calculated Ferrite (from XRF)

The last three columns of Table 4.6 list the mean XRF-calculated and Feritscope-measured percent ferrite, excluding the weld zone, and the difference between the calculated and measured. The calculated percent ferrite was by model #1 as provided in the footnote of Table 3.2 and described by Aubrey et al. (1982). Most of the differences are greater than the expected error of 6% with the measured values usually larger than the calculated values. As discussed earlier, the expected error from Feritscope measurements between 10% and 24% ferrite is ± 6% (Aubrey et al. 1982).

As shown in Table 4.6, the difference between the OD calculated and measured ferrite values for:

- SFM 156529 ranged from −8.8 to −7.4
- SFM 156361 from −0.5 to 10.4
- USP C2219A from −3.9 to −7.7
- Unknown heat used in the PISC-III columnar side from 0.0 to 14.7
- Unknown heat used in the PISC-III equiaxed side from −16.3 to −1.8
- Unknown heat used in the UMich specimens from −17.2 to −18.2.

Therefore, a key result of this study shows there was no apparent correlation between XRF-calculated and Feritscope-measured ferrite. This result supports the viewpoint that the calculated ferrite is based upon chemistry from XRF measurements, and affected only by the casting conditions, whereas the factors affecting the measured Feritscope ferrite may include variations in the casting process from foundry to foundry, the heat of welding, thermal stress relief, and machining.

Further, these data support the previously discussed conclusions in Section 4.2.2.5, that Feritscope-measured ferrite content is probably too sensitive to post-casting processes to be a reliable indicator of casting conditions. The grain structure, however, is dictated by the casting conditions including composition of the CASS which to a large degree is reflected in the OD XRF-calculated composition.

4.3.1.4 XRF Elemental Trends and Welds

Appendix B includes plots that show the mean of the circumferential ferrite concentrations at each axial position as measured by the Feritscope vs. the axial distance from the weld, as well as the calculated ferrite concentrations from the XRF elemental analysis. Calculated ferrite was determined by #1 model described in Table 3.2. Figure 4.3 is an example of plots that show that the calculated ferrite from XRF is essentially constant along the axis; whereas, the Feritscope measured ferrite usually decreased near the weld, likely due to the heat of welding.

Thus, the XRF-calculated ferrite shows the variation of Feritscope-measured ferrite is not due to variation in elemental content along the CCSS pipe axis.

4.3.1.5 XRF Summary Results and Preliminary Conclusions

The results of the XRF analysis enable the following preliminary conclusions:

- The CCSS pipe heat SFM 144179 was not confirmed as a possible source of either the columnar or equiaxed sides of the three PISC-III specimens studied here.
- The elemental uniformity within all of the specimens studied, except the PISC-III specimens, was within estimated error.
- The elemental uniformity of both the columnar and equiaxed sides of the PISC-III specimens as measured by XRF was poor.
- The mean XRF-measured elemental content from different CCSS specimens from the same heat, compared well within the estimated measurement error except for the three PISC-III specimens.
- The XRF-measured Ni content at the ID was higher than at the OD on all of the specimens studied, which is consistent with predictions in the literature.
- The calculated percent ferrite from XRF measurements on all of the specimens studied was higher at the ID than at the OD; which is consistent with observations cited in the literature.
- The axial variation of the XRF elemental content for most of the specimens and elements within the specimens studied is within the estimated measurement error.
- The axial uniformity of the XRF elemental measurements on the PWROG specimens established for those specimens that the decrease in Feritscope-measured ferrite along the pipe axis toward the weld is not due to axial elemental compositional variations during casting.
- The ladle and XRF analysis for the four elements reported for heat number SFM 156529 compared within estimated error.

4.4 Ladle and XRF Elemental Analysis

Table 4.8 lists the elemental content of four elements analyzed by XRF for three heats of CCSS pipe cast by SFM as well as the ladle analysis as reported by the foundry for two heats of CCSS pipe cast by SFM. Only one heat and ladle analysis (SFM 156529) could be confirmed as being incorporated in specific specimens studied in this investigation (see Section 3.1.4). The specimens were APE-1 and MPE-6. The XRF-estimated elemental error ± values are higher than both of the standard deviations of the average for the two specimens from SFM 156529, which indicates that the XRF readings on the pipe from this heat are all within the estimated error for elemental analysis.

The ladle chemistry analyses were not available for any of the other CCSS heats incorporated in the specimens studied herein.

In the case of SFM 156529, the only heat for which ladle chemistry was available and which could be confirmed as being incorporated in specific specimens, the ladle and XRF analysis compared well.

4.5 Estimation of Columnar Grains

4.5.1 Computation of Quantitative Measure of Grain Structure

The following summarizes the computation of a quantitative measure of grain structure (percent columnar grains) through the wall thickness of the CCSS pipe described in Section 4.1.

The PISC-III specimens had two sides identified as either C for columnar or E for equiaxed. Photomicrographs are shown in Bates et al. (1987, Appendix C) and are estimated as either 100% columnar (for the columnar side) or 0% columnar (for the equiaxed side).

The microstructure of the Westinghouse Spool piece is listed in Ruud et al. (2009, Table 4.4), as having one band of columnar grains; thus, it is estimated as 100% columnar.

The microstructure of the IHI CCSS pipe as shown in Diaz et al. (2007, Figures 5.1, A.11, and A.12) reveals that the pipe has different grain structures along the circumference at a single axial position. The information listed in Ruud et al. (2009, Table 4.4) lists two extremes; a single band with 100% columnar grains and nine bands, five of which have columnar and four equiaxed grains. The calculation of the percent columnar grains in the nine bands would result in 100% × (16+12+11+6+20 mm)/81 mm [(0.63+0.47+0.43+0.24+0.79 in.)/3.2 in.] = 80%, where the five columnar bands are 16, 12, 11, 6, and 20 mm thick (0.63, 0.47, 0.43, 0.24, and 0.79 in.) thick and 81 mm (3.2 in.) is the wall thickness of the IHI CCSS pipe. Averaging the single band and the nine bands would result in an average of 90% columnar for the IHI CCSS pipe.

The three UMich specimens are not listed in Ruud et al. (2009, Table 4.4). An examination of the microstructure (Table 3.3) did not provide clear indication of the grain structure, although it appears to be banded, equiaxed, and/or mixed grain.

The APE-1 PWROG specimen was listed in Ruud et al. (2009, Table 4.4) as having three bands of MG (mixed grains); thus, the CCSS pipe in APE-1 was 50% columnar.

The MPE-6 PWROG specimen was listed in Ruud et al. (2009, Table 4.4) as having three bands, the first as columnar 24 mm (0.9 in.) thick, the second as equiaxed 25 mm (0.98 in.), and the third as equiaxed 22 mm (0.87). Thus, the calculated percent columnar was 100% × 24 mm/(24+25+22 mm) [100% × 0.9 in./(0.9+0.98+0.87)] = 34% columnar.

The ONP-3-8 PWROG specimen was listed in Ruud et al. (2009, Table 4.4) as having two MG bands and because the CCSS pipe from it and ONP-3-5 are the same heat, it is assumed that they have the same microstructure. Thus, because both bands are MG, it is assumed that these CCSS pipes are 50% columnar.

The ONP-D-5 PWROG specimen was listed in Ruud et al. (2009, Table 4.4) as having one MG band and because the CCSS pipe from it and ONP-D-2 are the same heat, it is assumed that they have the same microstructure. Thus, because the one band is MG, it is assumed that the CCSS pipe is 50% columnar.

The OPE-2 PWROG specimen was listed in Ruud et al. (2009, Table 4.4) as having two bands, the first with columnar grains and 30 mm (1.18 in.) thick and the second with equiaxed grains and 21 mm (0.8-in) thick. Thus, the calculated percent columnar would be 100% × 30 mm/(30+21 mm) [100% × 1.18 in./(1.18+0.8 in.)] = 59% columnar. The CCSS in OPE-5 is the same heat as OPE-2, and thus is assumed to have the same percent columnar grains; that is, 59%.

4.5.2 Summary Results of Columnar Grain Estimation

The results of the columnar grain estimation process described above are summarized in Table 4.9.

Table 4.9. Summary of Columnar Grain Percentage Estimation

Specimen	% Columnar Grains
B-510C	100
B-516C	100
B-527C	100
B-510E	0
B-516E	0
B-527E	0
Westinghouse Spool	100
IHI	90
APE-1	50
MPE-6	34
ONP-D-2	50
ONP-D-5	50
ONP-3-5	50
ONP-3-8	50
OPE-2	59
OPE-5	59

4.6 Merged Analysis/Discussion of Results

Figure 4.7(a) shows the grain type, as percent columnar grains, from Table 4.9 plotted against the refined calculated percent ferrite from the mean OD XRF measurements. These data are also provided in tabular form in Table 4.10. Figure 4.7(b) shows the Feritscope-measured percent ferrite from the OD (listed in Table 4.6) as a function of percent columnar grains.

Figure 4.7(a) shows an apparent correlation between the percent columnar grains and the calculated percent ferrite in that the higher the percent ferrite the more columnar grains will be present. However, poor correlation is seen between the Feritscope-measured ferrite value and the percent columnar grains (Figure 4.7(b))—further indication that the Feritscope-measured ferrite content is too sensitive to post-casting thermal and mechanical treatments to be a reliable indicator of the conditions extant at the time of solidification to reveal grain structure.

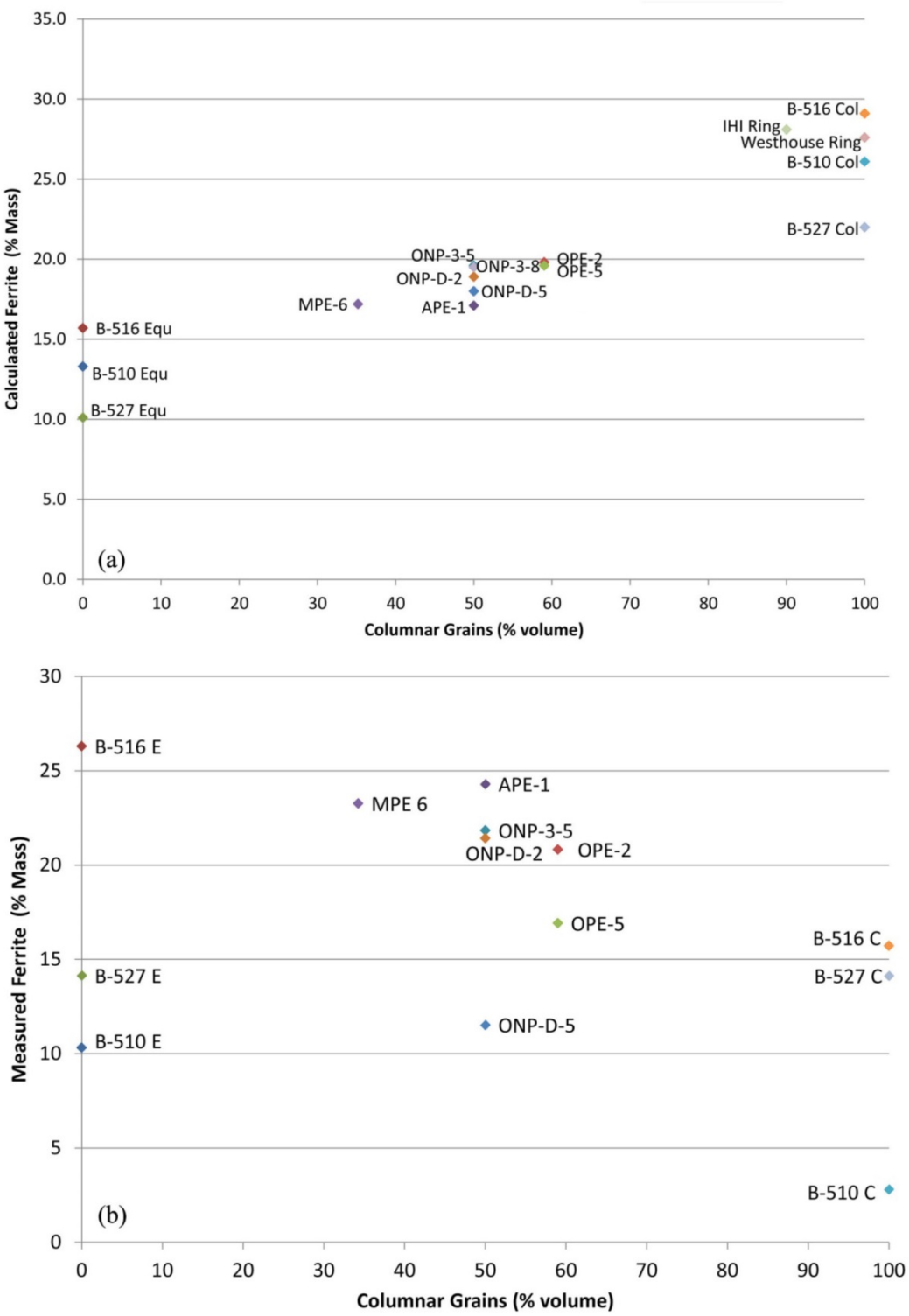

Figure 4.7. Mean (a) Calculated and (b) Measured Ferrite Concentrations on OD Specimen Surfaces are Plotted Versus Percent Columnar Grain Concentration. The HAZ is excluded on the OD specimen surfaces for the measured ferrite concentrations.

Table 4.10. OD Mean Refined Elemental Content[(a)] by XRF and Calculated Ferrite

Specimen	Heat	Mean % Mn	Mean % Si[(b)]	Mean % Cr	Mean % Ni	Mean % Mo	Cr Equiv	Ni Equiv	Cr Equiv/ Ni Equiv	% Ferrite[(c,d,e)]	% Column Grains
APE-1	SFM 156529	0.566	1.00	20.276	8.122	0.0029	15.8	12.7	1.24	17.1	50
MPE-6	SFM 156529	0.559	1.00	20.363	8.183	0.0044	15.9	12.7	1.25	17.2	34
ONP-D-2	SFM 156361	0.435	1.00	20.837	8.360	0.0000	16.3	12.9	1.27	18.9	50
ONP-D-5	SFM 156361	0.448	1.00	20.842	8.477	0.0000	16.3	13.0	1.26	18.0	50
ONP-3-5	SFM 156361	0.423	1.00	20.947	8.363	0.0000	16.4	12.9	1.27	19.6	50
ONP-3-8	SFM 156361	0.446	1.00	20.883	8.315	0.0000	16.4	12.8	1.27	19.5	50
OPE-2	USP C2291A	0.905	1.00	20.195	8.228	0.5610	16.4	12.8	1.28	19.8	59
OPE-5	USP C2291A	0.903	1.00	20.264	8.316	0.5616	16.4	12.9	1.27	19.6	59
B-510 Col	Unknown	0.582	1.00	20.768	7.865	0.3625	16.7	12.4	1.35	26.1	100
B-510 Equ	Unknown	0.392	1.00	19.788	8.274	0.0000	15.3	12.8	1.19	13.3	0
B-516 Col	Unknown	0.804	1.00	21.117	7.835	0.3648	17.0	12.4	1.37	29.1	100
B-516 Equ	Unknown	0.535	1.00	20.263	8.306	0.0000	15.8	12.8	1.23	15.7	0
B-527 Col	Unknown	0.623	1.00	20.366	7.962	0.3676	16.3	12.5	1.30	22.0	100
B-527 Equ	Unknown	0.497	1.00	19.484	8.576	0.0000	15.0	13.1	1.14	10.1	0
UMich-1	Unknown	0.709	1.00	20.295	7.821	0.0195	15.8	12.4	1.28	19.8	
UMich-2	Unknown	0.707	1.00	20.261	7.813	0.0209	15.8	12.4	1.28	19.6	
UMich-3	Unknown	0.688	1.00	20.260	7.806	0.0185	15.8	12.4	1.28	19.7	
IHI Ring	Unknown	0.753	1.00	20.289	9.541	2.8782	19.3	14.1	1.37	28.1	90
Manior	Unknown	0.697	1.00	20.470	9.139	0.1390	16.1	13.7	1.18	12.3	
Westhse Ring	Unknown	0.681	1.00	20.545	9.833	2.9264	19.6	14.4	1.36	27.6	100

(a) Mean refined elemental content indicates that the some of the values for the elemental content measured by XRF on some of the specimens were omitted because they were one standard deviation away from the mean and the standard deviation was greater than the percent elemental error listed in Table 4.8.

(b) The XRF instrument did not measure silicon content, thus it was assumed as 1.000%.

(c) C was assumed as 0.04, N as 0.04, Si as 1.0 for CF8 and CF8A; these values compare well with the mean C, N, and Si values shown for the heats listed in Table 3.3 (i.e., 0.037, 0.039, and 1.1, respectively). Note the high values reported for N in two of the heats was questionable and thus not included in the calculation of the means. Note that the previous tables made the same assumptions except for C, which was assumed as 0.08%.

(d) The number 1 model for predicting ferrite content according to Aubrey et al. (1982): Cr equivalent = Cr_e = %Cr + 1.21 %Mo + 0.48 %Si − 4.99 and Ni equivalent = Ni_e = %Ni + 0.11 %Mn − 0.0086 $\%Mn^2$ + 18.4 %N + 24.5 %C + 2.77. Ferrite Content = $\%Fe_1 = 100.3 \times (Cr_e/Ni_e)^2 - 170.72\ (Cr_e/Ni_e) + 74.22$. Note these equations are based upon Hull's equivalent factors (Aubrey et al. 1982).

(e) Values of Mo and N were assumed to be 0.5 and 0.04 where chemistry data for these elements were not available (EPRI 1991).

It is likely that the XRF-calculated ferrite scatter in Figure 4.7(a) could be reduced if all of the elements used to calculate ferrite from elemental data (see Table 3.2 footnote) could be measured. The missing elements, which were not detectable with the XRF instrument available for this study were, Si, C, and N, and these were assumed to be 1.0, 0.4, and 0.4, respectively, in Table 4.10, based on nominal ranges for these elements in cast stainless steels from the literature. Nevertheless, XRF instruments exist that can measure Si, which might provide a more precise calculation for ferrite, and may reduce the uncertainty in the prediction of the percent columnar grains shown in Figure 4.7.

Figure 4.7(a) indicates that there may be a correlation between the calculated percent ferrite as measured at the OD and the grain structure as defined by the percent columnar grains. This does not support Temple and Ogilvy (1992) claim that the grain structure in CASS with lower ferrite content is likely to tend toward columnar grains. Figure 4.7(b) demonstrates that Feritscope-measured ferrite does not correlate with grain structure as represented by percent columnar grains.

Nevertheless, it is reasonable that the elemental content at the OD is a measure of the elemental content of the metal as it initially solidifies and reflects the actual initial casting conditions. This is supported by the ASM Handbook (1992, p. 298), “The as-cast structures obtained in horizontal centrifugal casting of steels vary according to composition.” Because the initial solidification has a major effect on the grain structure of the CCSS pipe, the correlation shown in Figure 4.7(a) is logical.

Further, the correlations in this report are based upon a small statistical sampling of CCSS heats and only four of the seven pertinent elements; thus, the examination of more heats and more elements are required to firmly establish the correlation with calculated percent ferrite as determined by XRF analysis.

5.0 Conclusions

This report describes the results of research to determine if correlations exist between measured delta ferrite content in CASS components and the microstructure of these components. An earlier review of the literature had indicated that the propensity for the development of columnar grains in CASS pipe and components may be enhanced by low ferrite content of the casting alloy. The research described in this report examined a number of vintage CASS specimens using commercially available instrumentation for measuring ferrite content in metals. In addition to a direct measurement of ferrite content, an indirect estimate was also obtained using elemental composition measured using XRF. The resulting data sets were analyzed to determine the correlation in ferrite content (measured or calculated) with respect microstructure. The sensitivity of this correlation to a number of variables was examined: spatial location on the OD surface, spatial location on the ID surface, through-thickness, proximity to a weld. The analysis also incorporated the measurement variability inherent to these measurements, and attempted to assess whether any changes observed in ferrite content were significant enough (i.e., greater than the measurement variability). The conclusions drawn from these analyses are summarized below.

5.1 Primary Conclusions

Based on the analysis of both ferrite and XRF measurements from a set of available CASS piping, the following primary conclusions may be drawn:

- There appears to be a correlation between grain structure, as defined by percent columnar grains, and ferrite percent as calculated from XRF OD measurements.
- There is no apparent correlation between Feritscope-measured ferrite levels and grain structure.
- The percentage of ferrite present in CCSS pipe as measured by Feritscope is likely too sensitive to post-casting thermal (including welding) and mechanical processes to be a reliable indicator of grain structure solidification.

5.2 Secondary Conclusions

In addition, the following secondary conclusions may be drawn:

- The elemental uniformity within all of the specimens studied, except the PISC-III specimens, was within estimated XRF error.
- The mean XRF-measured elemental content from different CCSS specimens from the same heat compared well within the estimated measurement error except for the three PISC-III specimens.
- The XRF-measured Ni content at the ID was higher than at the OD on all of the specimens studied, which is consistent with predictions in the literature.
- The calculated percent ferrite from XRF measurements on all of the specimens studied was higher at the ID than at the OD; which is consistent with observations cited in the literature.
- The axial variation of the XRF elemental content within the specimens studied is, for most of the specimens and elements, within the estimated measurement error.

- The axial uniformity of the XRF elemental measurements on the PWROG specimens established that the decrease in Feritscope-measured ferrite along the pipe axis toward the weld of the welded specimens is not due to axial elemental compositional variations during casting. Further, variation of Feritscope-measured ferrite along the CCSS pipe axis is likely not due to variations in casting parameters.
- Feritscope-measured ferrite may provide a technique for the detection of post-casting thermal and mechanical effects in CCSS pipe.
- Ferrite calculated from XRF elemental measurements is not sensitive to post-casting thermal (including welding) and mechanical processing.
- The Feritscope-measured ferrite content in specimen B516 is not consistent with the other two PISC-III specimens.
- The ladle and XRF analysis for three of the elements reported for heat number SFM 156529, used in PWROG APE-1 and MPE-6, compared within estimated error. Ladle measurements were not available for molybdenum.
- The CCSS pipe heat SFM 144179 was not confirmed as a possible source of either the columnar or equiaxed side of the three PISC-III specimens studied.

5.3 Open Questions

Improving the reliability of field ultrasonic inspection methods will likely require the ability to first fully characterize the grain structure through the volume of the CASS specimen. The apparent correlations between grain structure, as defined by percent columnar grains, and ferrite percent as calculated from XRF OD measurements are only an incremental step towards the ultimate goal of improving the reliability of UT. The percentage of columnar grains is a coarse metric, and does not capture the complexity of the grain structure distribution (purely columnar, purely equiaxial, banded, mixed, banded and mixed, etc.) through the volume of vintage CASS specimens. Further, the use of XRF to obtain a volumetric distribution of grain structures (through measurements of elemental composition as a function of spatial location within the volume) is unlikely, as the XRF is sensitive to near-surface elemental composition only. Instead, characterizing the grain structure through the volume of the CASS specimen may be possible, for instance, using various ultrasonic measurement techniques as documented in several previous TLRs (Ramuhalli et al. 2010; Ramuhalli et al. 2009; Ramuhalli et al. 2011).

It is unclear whether surface inspection methods, such as eddy current inspection, are widely used in the field inspection of CASS. However, the results described here indicate that the variation in ferrite content (near the OD, and near the ID) is likely to have an impact on the ability to use eddy current inspection in CASS for reliable detection of flaws. Additional research will need to be conducted to quantify the effect of such ferrite variations on eddy current inspection techniques.

Finally, the use of measurements on additional specimens is likely to improve the understanding of the correlations between ferrite percentage and grain structure in CCSS piping. Such measurements would need to include:

- XRF elemental analysis on the OD locations on specimens studied herein using a XRF instrument capable of measuring Si, P, and S, and recalculate the percent ferrite.
- XRF elemental analysis on the OD locations of additional CCSS specimens of known grain structure in order to establish a more precise relationship between grain structure and calculated ferrite content.

- Develop a multivariate elemental model to calculate a parameter predicting the percent columnar grains using all of the elements heavier than Ti quantified by XRF.
- Develop a multivariate elemental model to calculate a parameter predicting the probability of grain structure interfering with ultrasonic inspection of CCSS pipe using all of the elements heavier than Ti quantified by XRF.

6.0 References

Anderson MT, SL Crawford, SE Cumblidge, KM Denslow, AA Diaz and SR Doctor. 2007. *Assessment of Crack Detection in Heavy-Walled Cast Stainless Steel Piping Welds Using Advanced Low-Frequency Ultrasonic Methods*. NUREG/CR-6933, PNNL-16292, U.S. Nuclear Regulatory Commission, Washington, D.C. ADAMS Accession No. ML071020410.

ASM. 1980. *ASM Handbook, Volume 3, Alloy Phase Diagrams*. ASM International, Materials Park, Ohio.

ASM. 1992. *ASM Handbook, Volume 15: Casting*. ASM International, Materials Park, Ohio.

ASNT. 2004. *Nondestructive Testing Handbook, Third Edition: Volume 5, Electromagnetic Testing*. SS Udpa and PO Moore, American Society for Nondestructive Testing, Columbus, Ohio.

Aubrey LS, PF Wieser, WJ Pollard and EA Schoefer. 1982. "Ferrite Measurement and Control in Cast Duplex Stainless Steels." In *Stainless Steel Castings, ASTM STP 756*, eds: VG Behal and AS Melilli. American Society for Testing Materials, West Conshohocken, Pennsylvania.

Bates DJ, SR Doctor, PG Heasler and E Burck. 1987. *Stainless Steel Round Robin Test: Centrifugally Cast Stainless Steel Screening Phase*. NUREG/CR-4970, PNL-6266, PISC III Report No. 3, U.S. Nuclear Regulatory Commission, Washington, D.C.

Chopra OK. 1991. *Estimation of Fracture Toughness of Cast Stainless Steel During Thermal Aging in LWR Systems*. NUREG/CR-4513, ANL-90/42, R2, U.S. Nuclear Regulatory Commission, Washington, D.C.

Chopra OK and HM Chung. 1985. *Long-Term Embrittlement of Cast Duplex Stainless Steels in LWR Systems - Annual Report October 1983 - September 1984*. NUREG/CR-4204, ANL-85-20, U.S. Nuclear Regulatory Commission, Washington, D.C.

Chopra OK and A Sather. 1990. *Initial Assessment of the Mechanisms and Significance of Low-Temperature Embrittlement of Cast Stainless Steels in LWR Systems*. NUREG/CR-5385, ANL-89/17, U.S. Nuclear Regulatory Commission, Washington, D.C.

Diaz AA, RA Mathews, J Hixon and SR Doctor. 2007. *Assessment of Eddy Current Testing for the Detection of Cracks in Cast Stainless Steel Reactor Piping Components*. NUREG/CR-6929, PNNL-16253, U.S. Nuclear Regulatory Commission, Washington, D.C.

EPRI. 1991. *Application of Electromagnetic Acoustic Transducers to Coarse-Grained Material*. EPRI NP-7438, Electric Power Research Institute, Palo Alto, California.

Hammar O and J Svensson. 1979. "Influence of Steel Composition on Segregation and Microstructure During Solidification of Austenitic Stainless Steels." In *Solidification and Casting of Metals: Proceedings of an International Conference on Solidification*, pp. 401-410. July 18-21, 1977, Sheffield, England. Metals Society, London.

Lundin CD and CPD Chou. 1983. *Hot Cracking Susceptibility of Austenitic Stainless Steel Weld Metals*. WRC Bulletin 289, Welding Research Council, New York.

Massoud J-P, C Boveyron, P Ould, G Bezdikian and H Chuier-Bessenec. 1998. "Effect of the Manufacture Process on Thermal Ageing of PWR Duplex Stainless Steel Components." In *6th International Conference on Nuclear Energy (ICONE)*. May 10-14, 1998, San Diego, California. American Society of Mechanical Engineers (ASME), New York. Paper 6085.

Ramuhalli P, LJ Bond, R Mathews, KC Roberts, RV Harris Jr., AA Diaz, MT Anderson and CO Ruud. 2010. *In-situ Characterization of Cast Austenitic Stainless Steel Microstructure: An Interim Study*. PNNL-19325, Pacific Northwest National Laboratory, Richland, Washington.

Ramuhalli P, MS Good, AA Diaz, MT Anderson, BE Watson, TJ Peters, M Dixit and LJ Bond. 2009. *Ultrasonic Characterization of Cast Austenitic Stainless Steel Microstructure: Discrimination between Equiaxed- and Columnar-Grain Material – An Interim Study*. PNNL-18912, Pacific Northwest National Laboratory, Richland, Washington.

Ramuhalli P, RM Meyer, AD Cinson, TL Moran, BE Watson, MS Prowant, RV Harris Jr., R Mathews, AA Diaz and MT Anderson. 2011. *In-situ Characterization of Cast Austenitic Stainless Steel Microstructures*. PNNL-20550, Pacific Northwest National Laboratory, Richland, Washington.

Ratz GA and RB Gunia. 1969. "How Accurate are Methods for Measuring Ferrite?" *Metal Progress* 95(1):76-80.

Ruud CO, AA Diaz and MT Anderson. 2009. *Grain Structure Identification and Casting Parameters of Austenitic Stainless Steel (CASS) Piping*. PNNL-19002, Pacific Northwest National Laboratory, Richland, Washington.

Steele JH and JL McCall. 1984. *STP839, Practical Applications of Quantitative Metallography*. ASTM International, West Conshohocken, Pennsylvania.

Temple JAG and JA Ogilvy. 1992. *Propagation of Ultrasonic Elastic Waves in Centrifugally Cast Austenitic Steel*. AEA-RS-4223, AEA Reactor Services, Risley, United Kingdom.

Verma HR. 2007. *Atomic and Nuclear Analytical Methods: XRF, Mossbauer, XPS, NAA and Ion-Beam Spectroscopic Techniques*. Springer-Verlag, Berlin.

Appendix A

Measured Ferrite Through-Thickness Trends in CCSS Piping Specimens

Appendix A

Measured Ferrite Through-Thickness Trends in CCSS Piping Specimens

Appendix A contains plots of the measured ferrite using the Feritscope along the cross-section of selected CCSS piping specimens. The scan area was approximately 5.08×5.08 mm (2×2 in.). The cross sections are either the axial-radial (side-view) or circumferential-radial (end-view) of the specimens, or both. A listing of the radial cross-section scans is presented in Table 4.1. The plots presented in this appendix show the measured ferrite vs. the distance (in inches) from the OD surface of the pipe. For axial-radial cross-sections, the measured ferrite was averaged in the axial direction. For circumferential-radial cross sections, the ferrite was averaged in the circumferential direction.

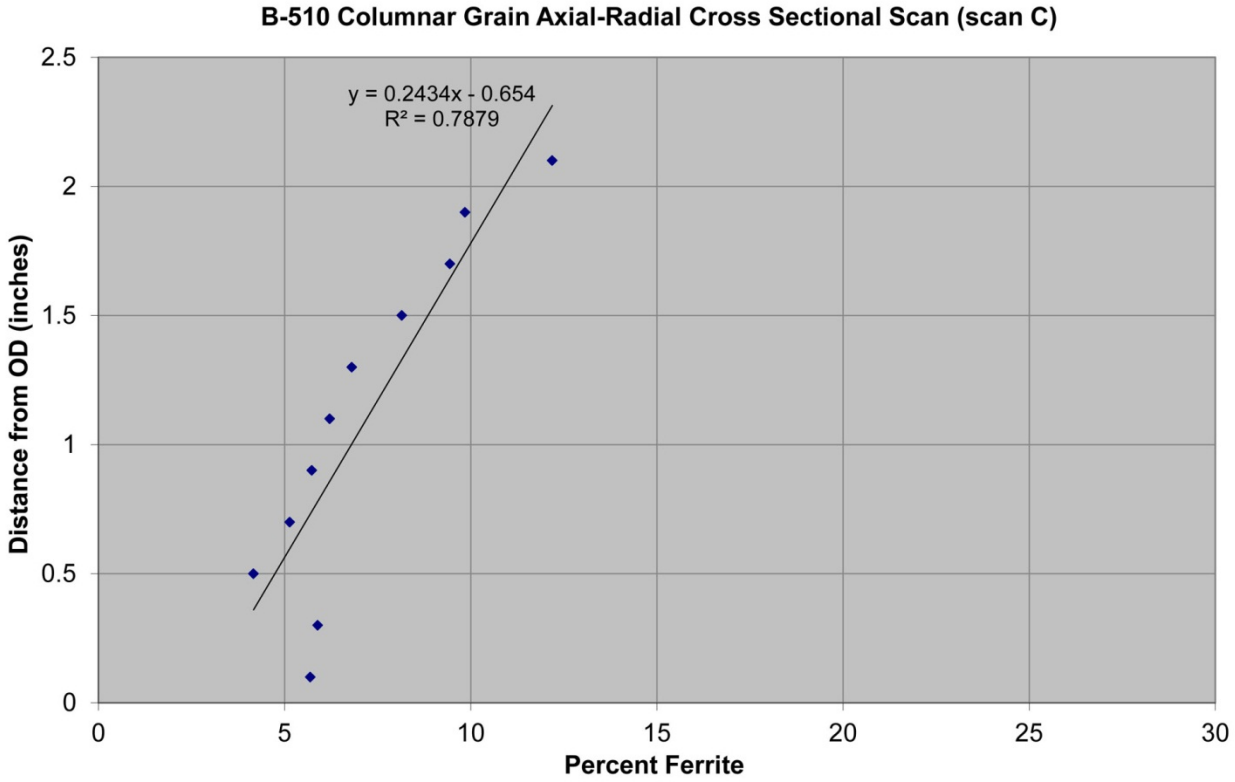

Figure A.1. Measured Ferrite Content along the Axial-Radial Cross Section for Specimen B-510, Columnar Side, Presented as a Function of Distance from the OD Surface

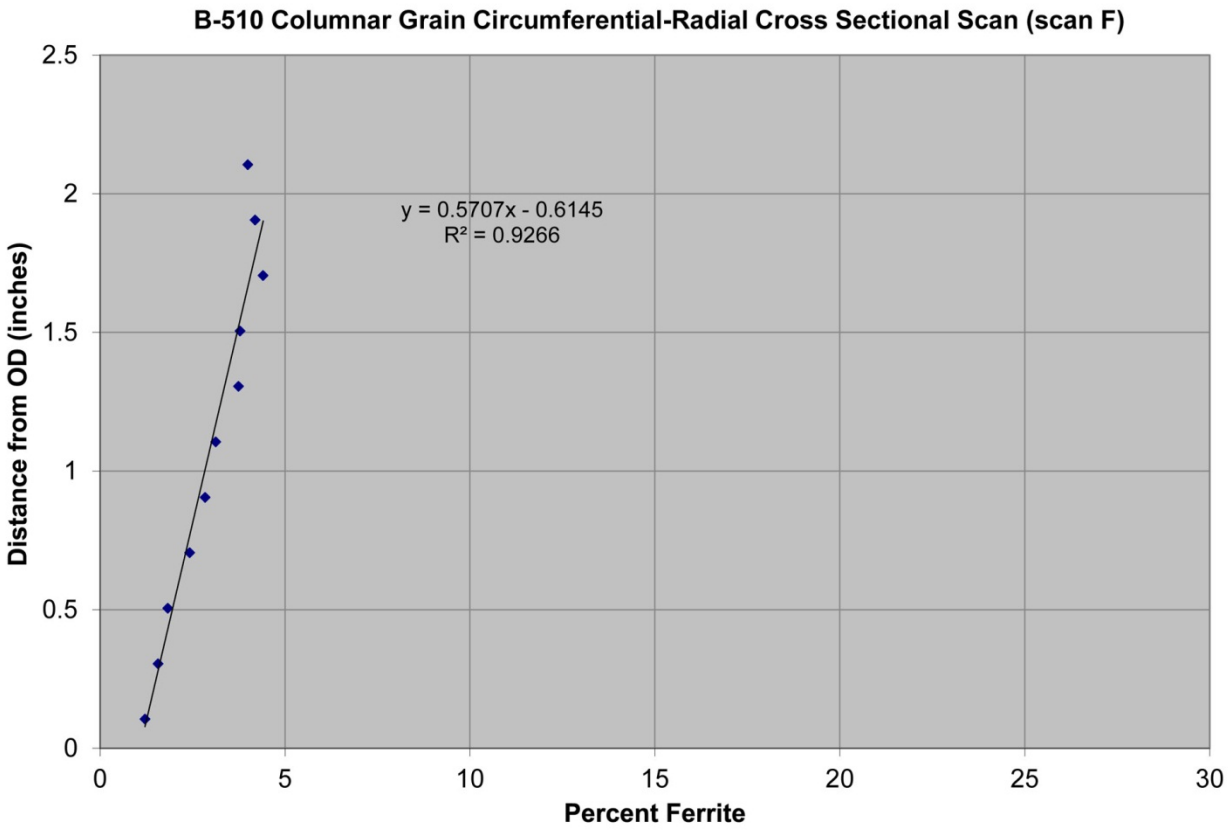

Figure A.2. Measured Ferrite Content along the Circumferential-Radial Cross Section for Specimen B-510, Columnar Side, Presented as a Function of Distance from the OD Surface

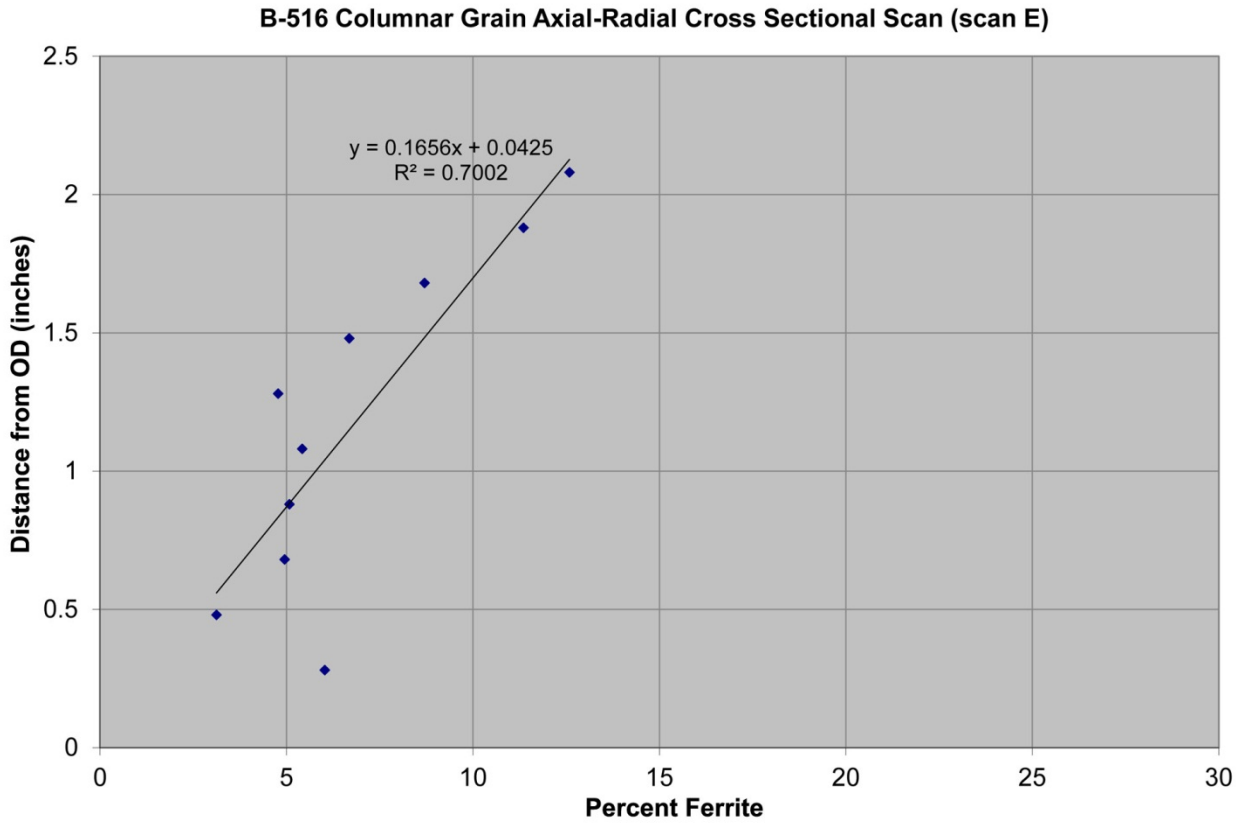

Figure A.3. Measured Ferrite Content along the Axial-Radial Cross Section for Specimen B-516, Columnar Side, Presented as a Function of Distance from the OD Surface

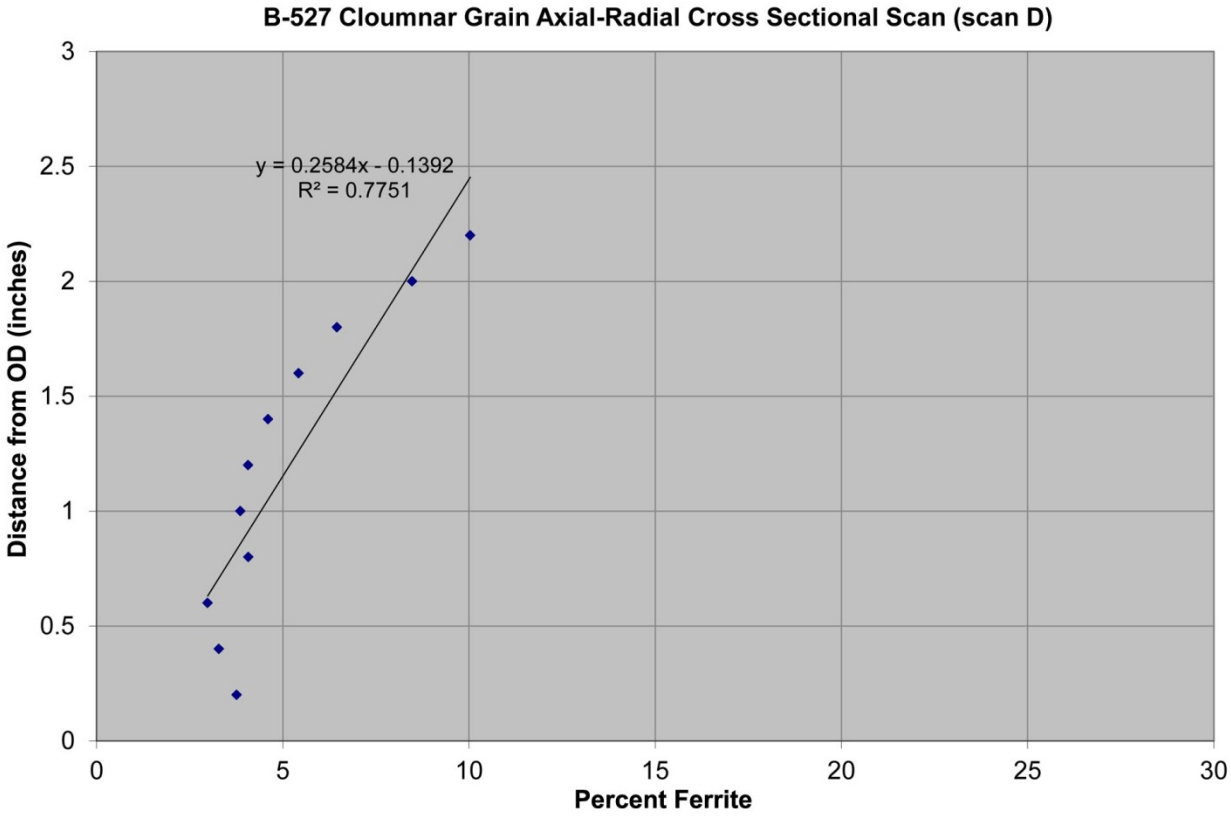

Figure A.4. Measured Ferrite Content along the Axial-Radial Cross Section for Specimen B-527, Columnar Side, Presented as a Function of Distance from the OD Surface

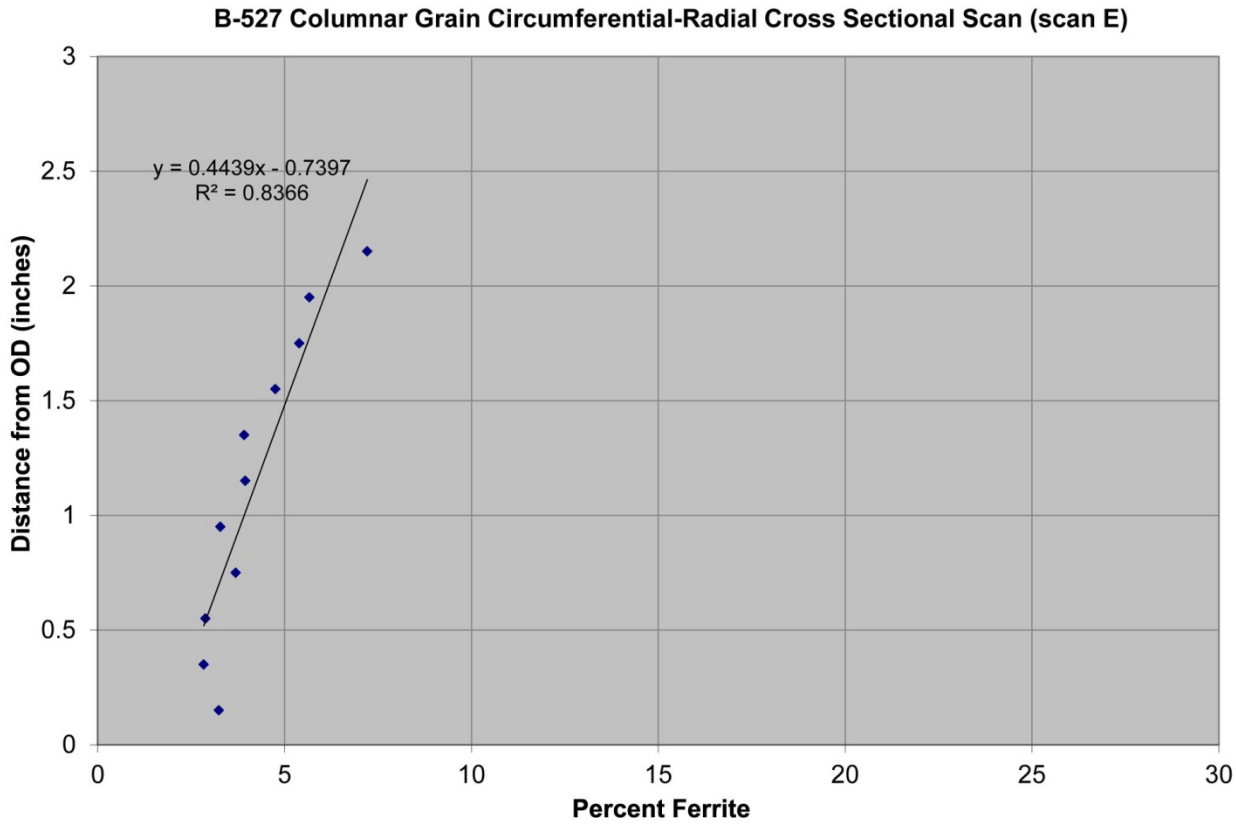

Figure A.5. Measured Ferrite Content along the Circumferential-Radial Cross Section for Specimen B-527, Columnar Side, Presented as a Function of Distance from the OD Surface

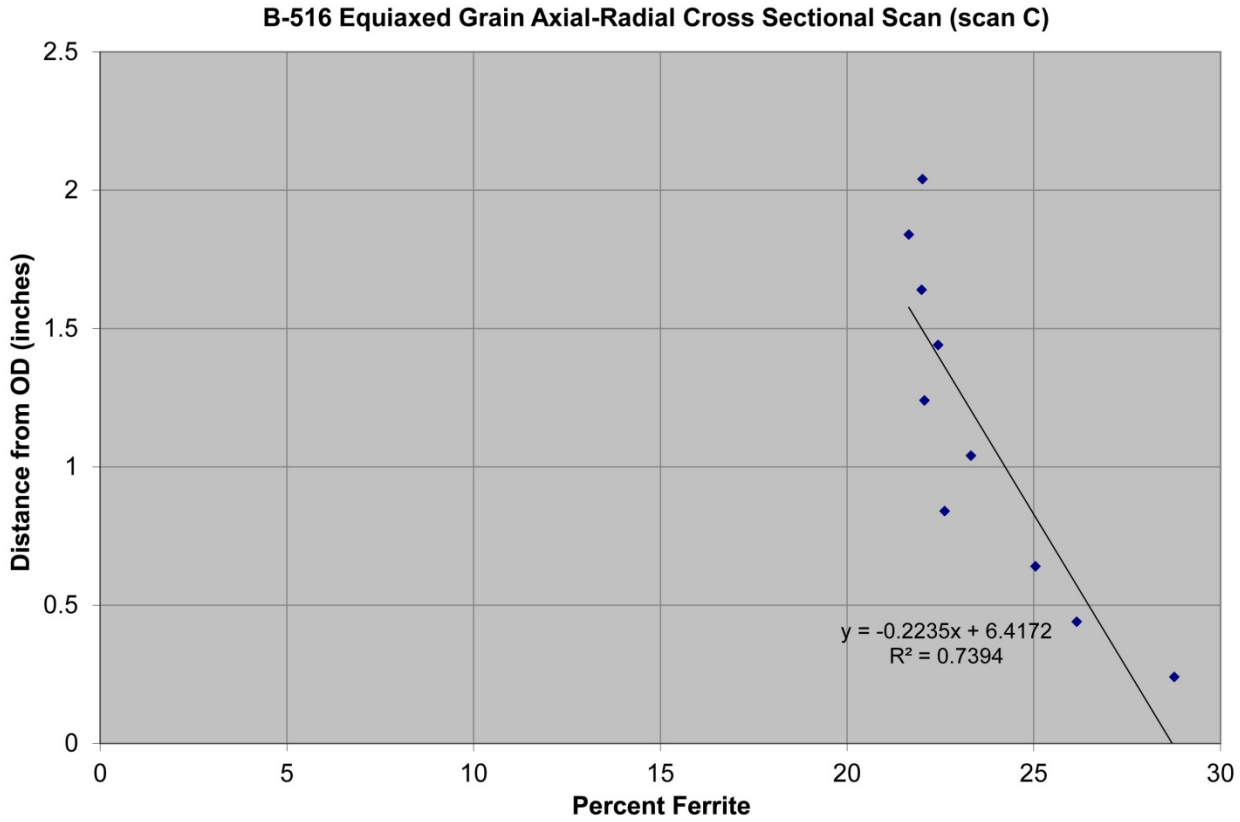

Figure A.6. Measured Ferrite Content along the Axial-Radial Cross Section for Specimen B-510, Equiaxed Side, Presented as a Function of Distance from the OD Surface.

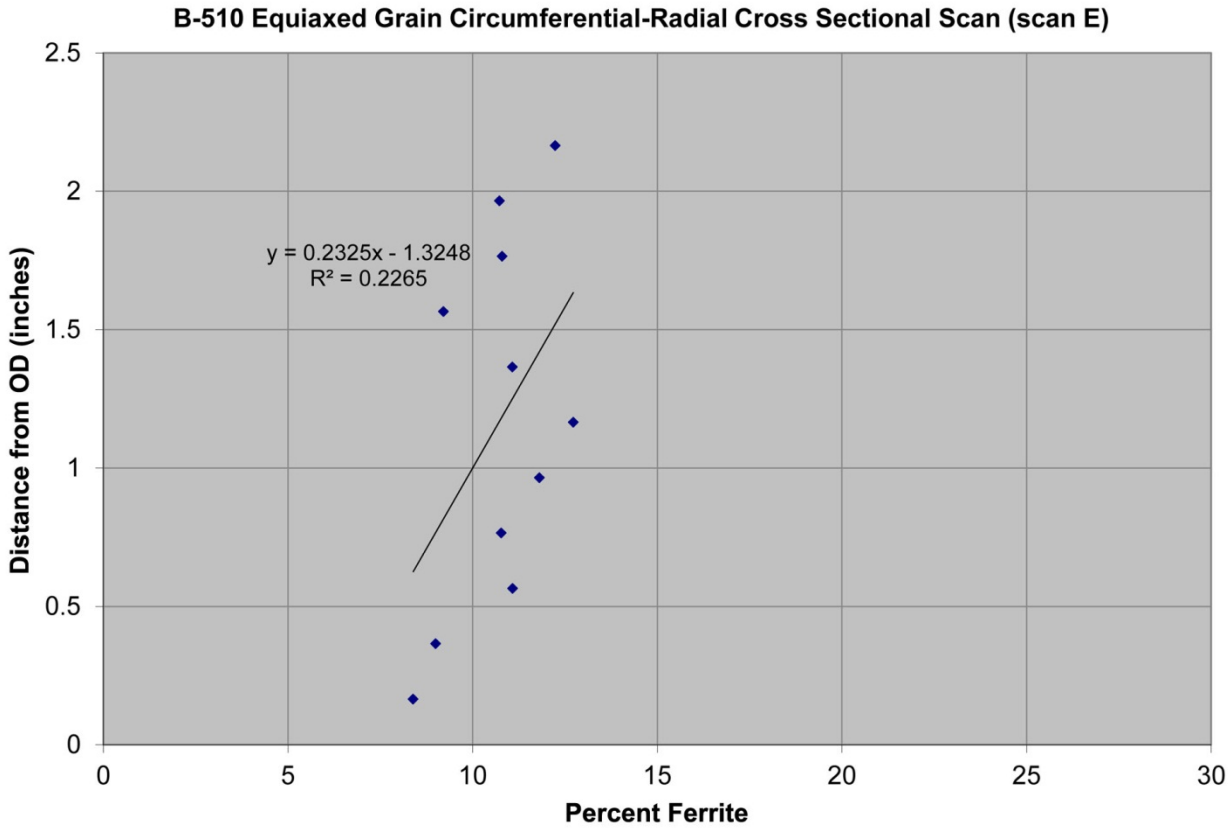

Figure A.7. Measured Ferrite Content along the Circumferential-Radial Cross Section for Specimen B-510, Equiaxed Side, Presented as a Function of Distance from the OD Surface

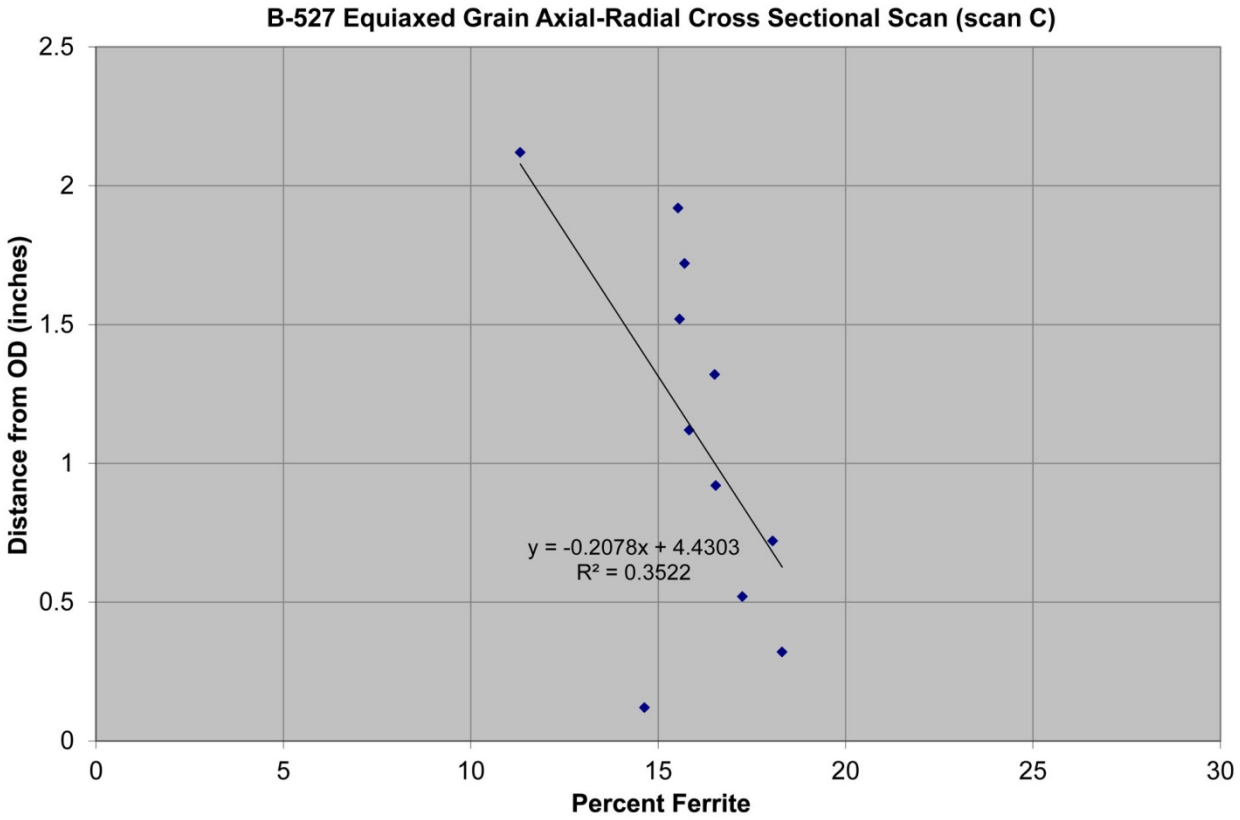

Figure A.8. Measured Ferrite Content along the Axial-Radial Cross Section for Specimen B-527, Equiaxed Side, Presented as a Function of Distance from the OD Surface

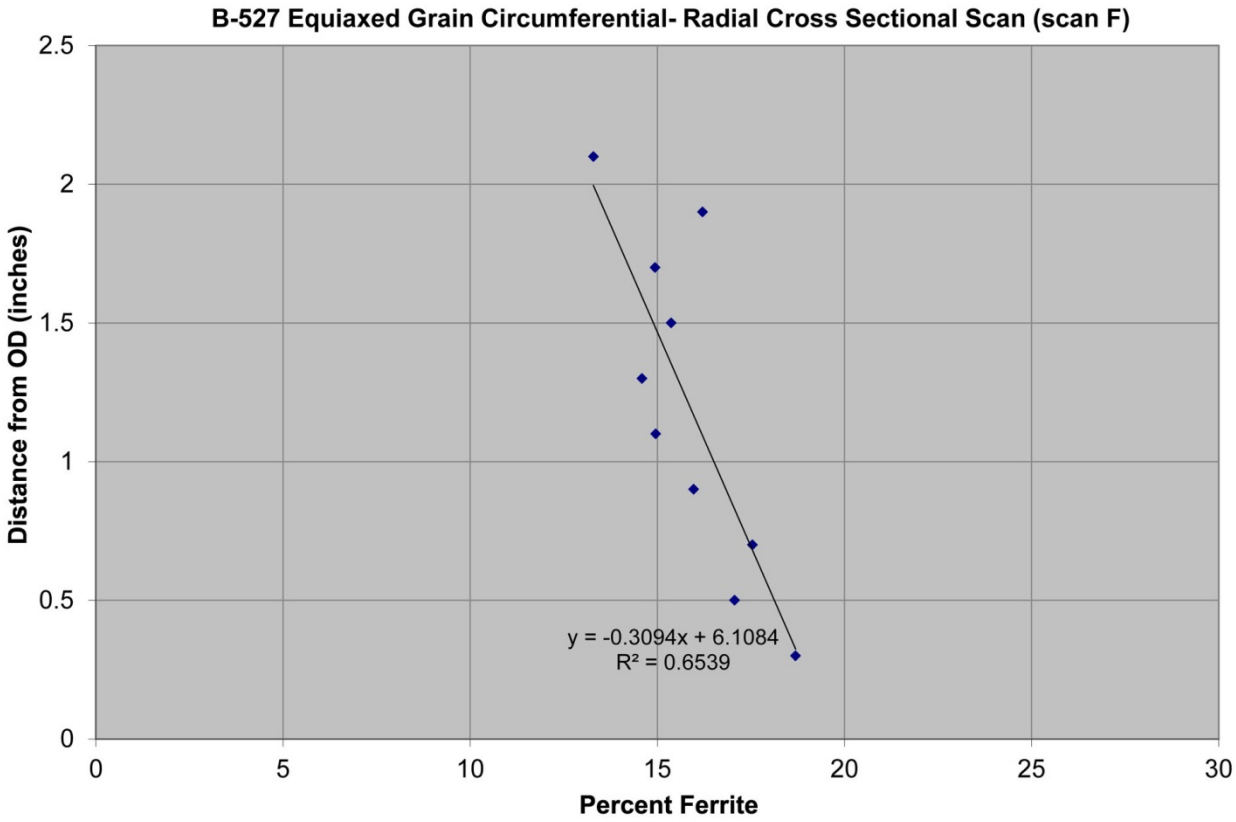

Figure A.9. Measured Ferrite Content along the Circumferential-Radial Cross Section for Specimen B-527, Equiaxed Side, Presented as a Function of Distance from the OD Surface

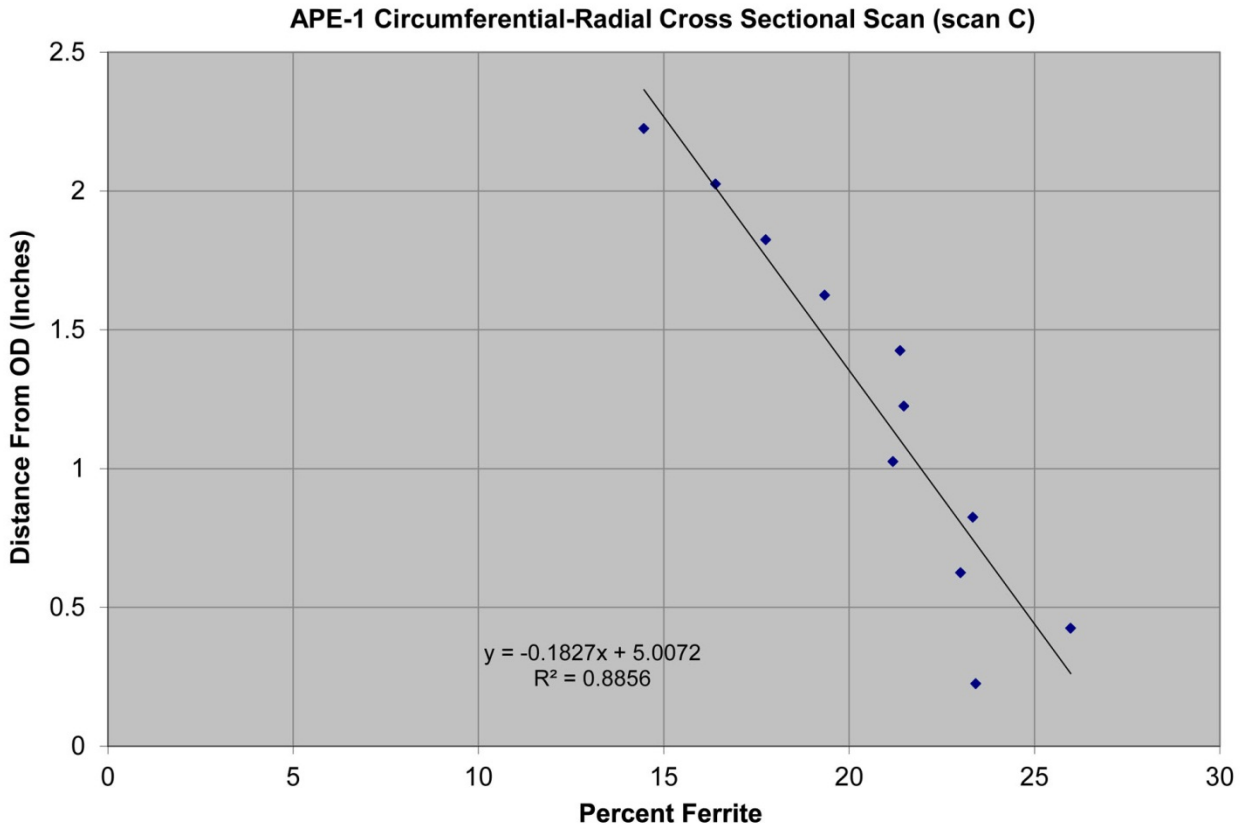

Figure A.10. Measured Ferrite Content along the Circumferential-Radial Cross Section for Specimen APE-1 Presented as a Function of Distance from the OD Surface

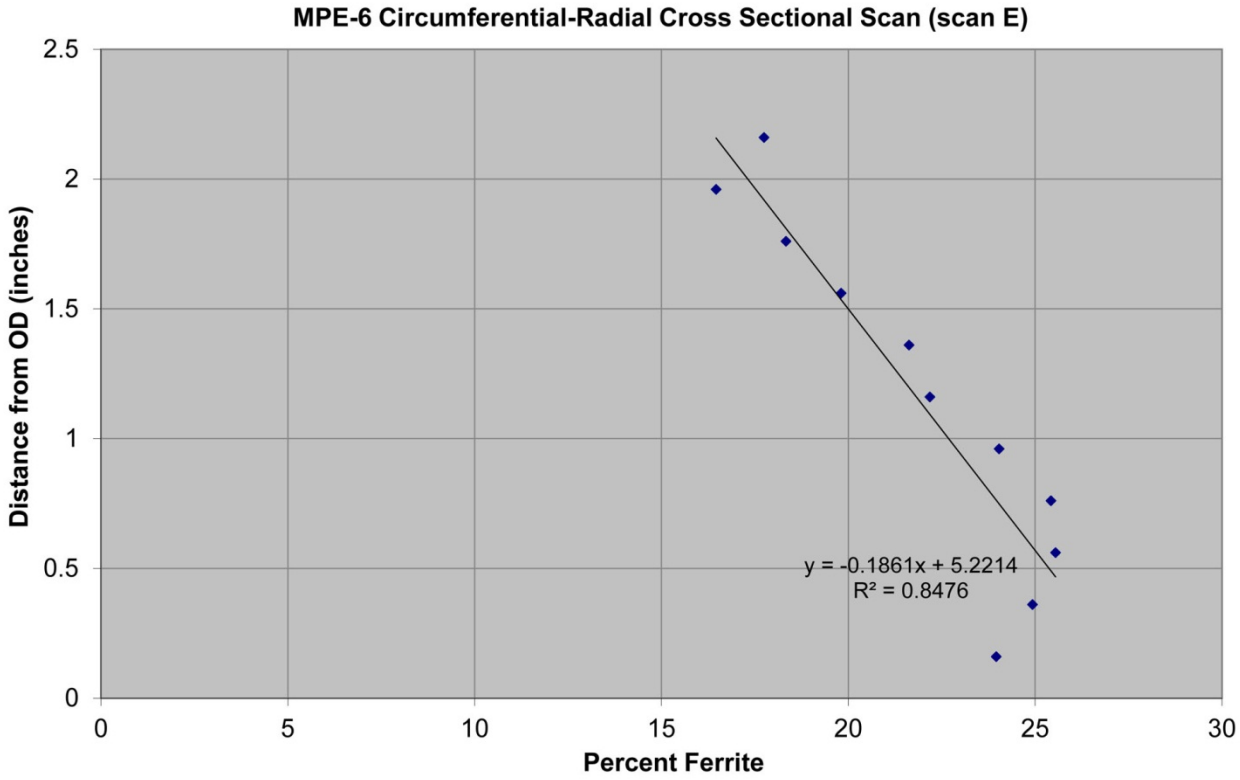

Figure A.11. Measured Ferrite Content along the Circumferential-Radial Cross Section for Specimen MPE-6 Presented as a Function of Distance from the OD Surface

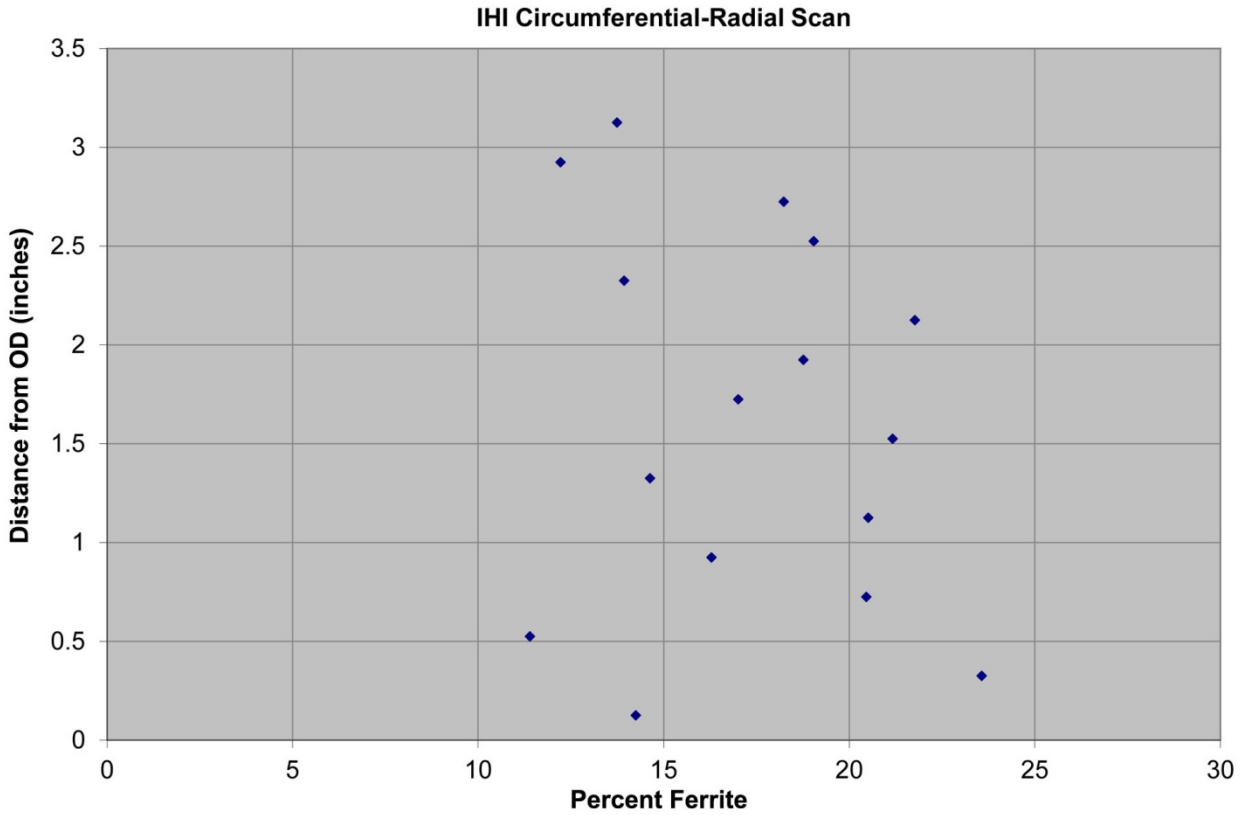

Figure A.12. Measured Ferrite Content along the Circumferential-Radial Cross Section for the IHI Southwest Ring Specimen Presented as a Function of Distance from the OD Surface

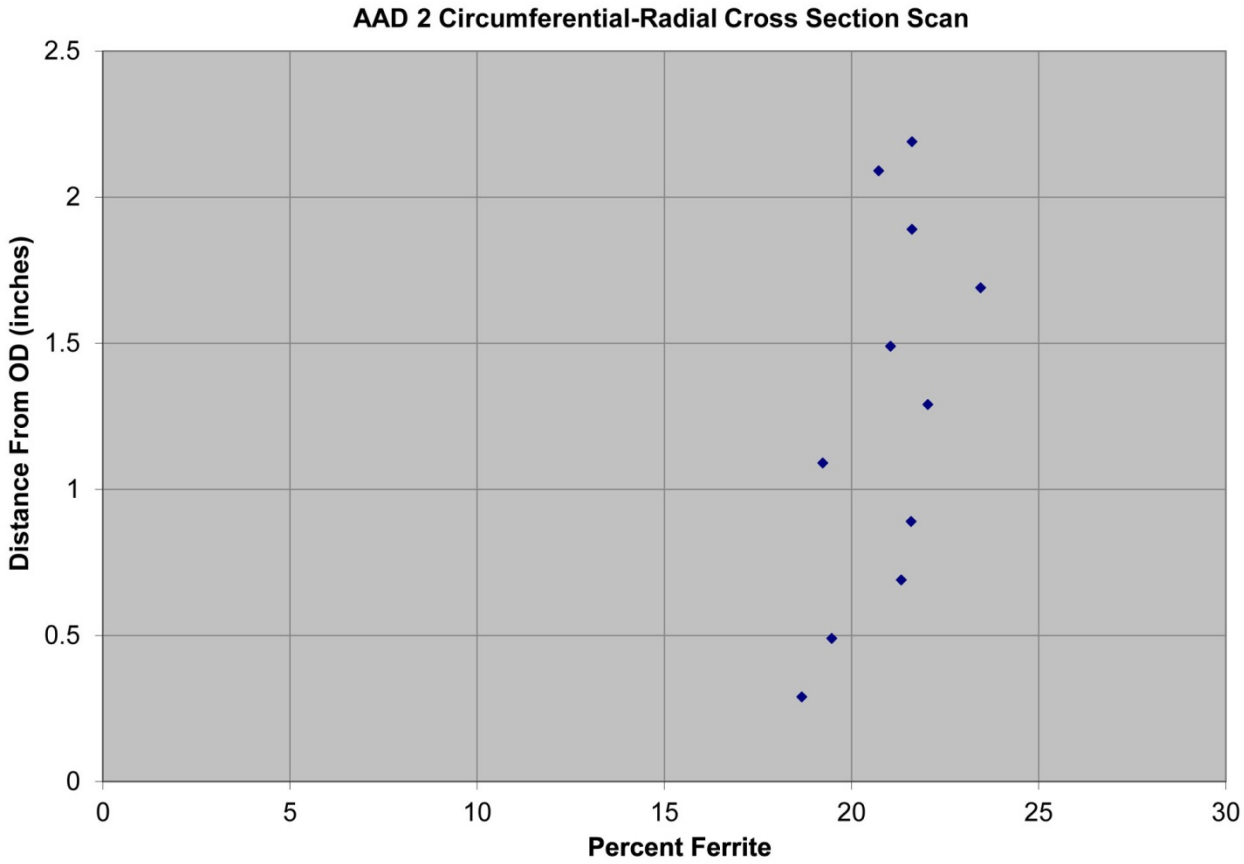

Figure A.13. Measured Ferrite Content along the Circumferential-Radial Cross Section for the AAD-2 Specimen Presented as a Function of Distance from the OD Surface

Appendix B

Calculated and Measured Ferrite Content in CASS Specimens

Appendix B

Calculated and Measured Ferrite Content in CASS Specimens

Appendix B contains plots of the calculated ferrite content (using the XRF measurements) and measured ferrite content (using the Feritscope) from the specimens examined in this study. The data are presented as a function of circumferential position (Figures B.1–B.16) as well as axial positions (Figures B.17–B.32). For example, the data presented for an axial position are values for locations at an equal distance from the weld center line (W_{CL}) around the circumference. In addition, a comparison of the mean ferrite content (calculated vs. measured) on the OD and ID surfaces is also presented (Figures B.33 and B.34).

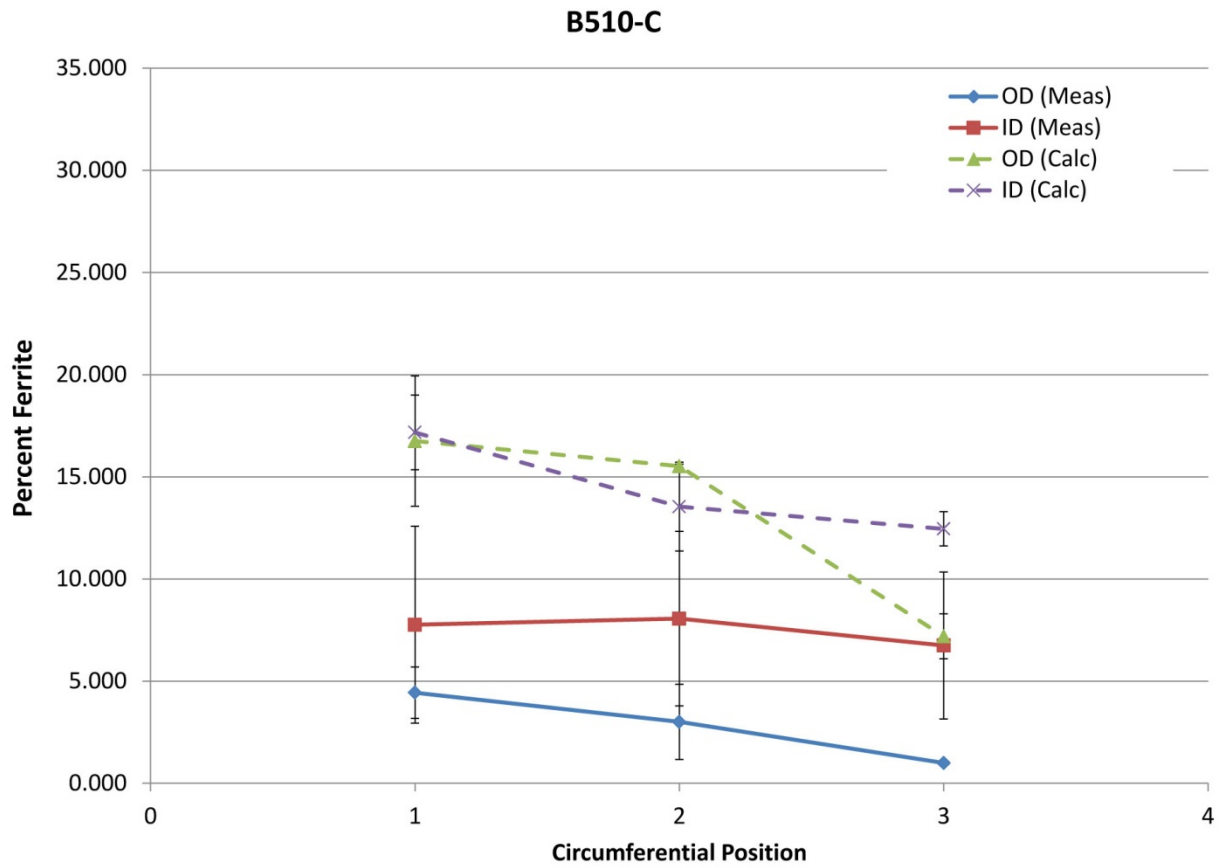

Figure B.1. Calculated Ferrite Concentrations Derived from XRF Measurements and Measured Ferrite Concentrations are Plotted with Respect to Circumferential Position on Specimen B510-C. Data are averaged over axial locations and the error bars represent one standard deviation. Measured ferrite concentrations exclude data within the weld.

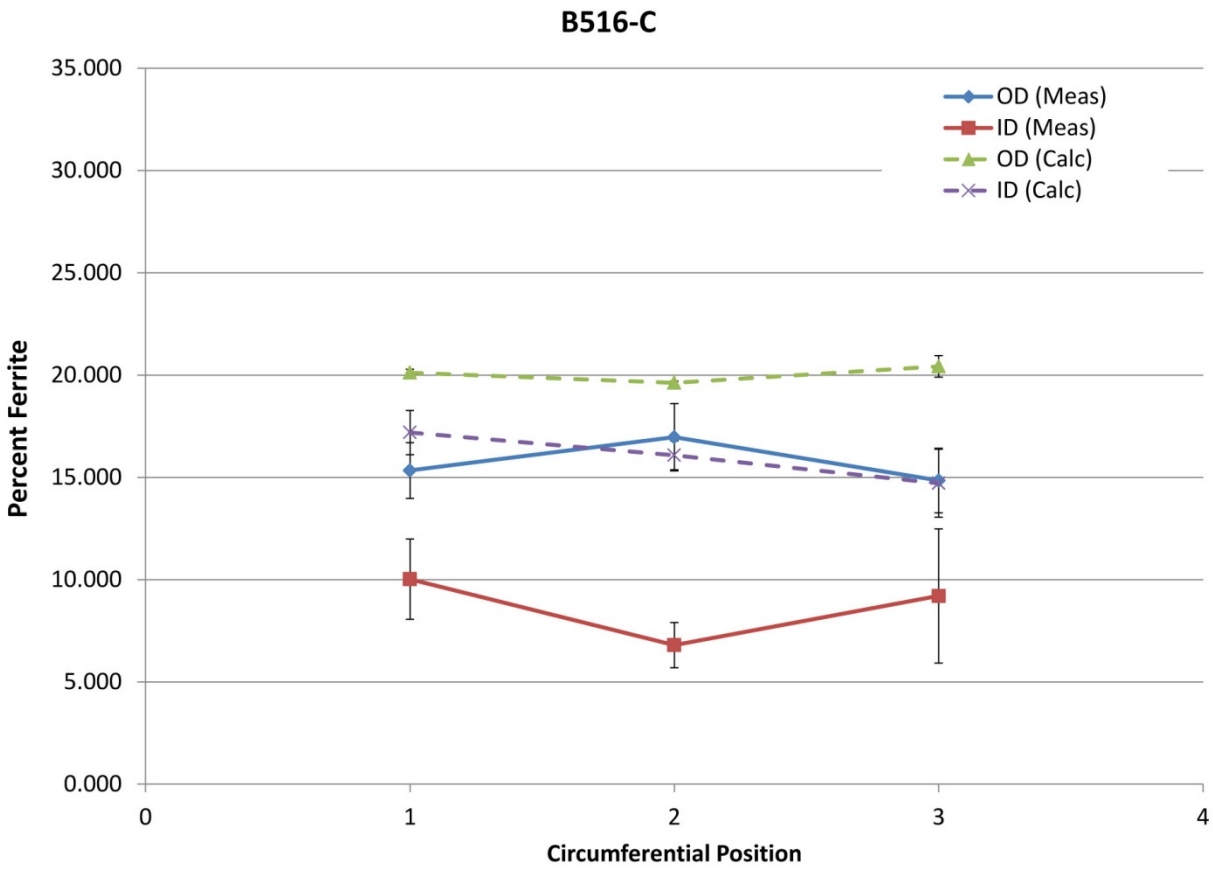

Figure B.2. Calculated Ferrite Concentrations Derived from XRF Measurements and Measured Ferrite Concentrations are Plotted with Respect to Circumferential Position on Specimen B516-C. Data are averaged over axial locations and the error bars represent one standard deviation. Measured ferrite concentrations exclude data within the weld.

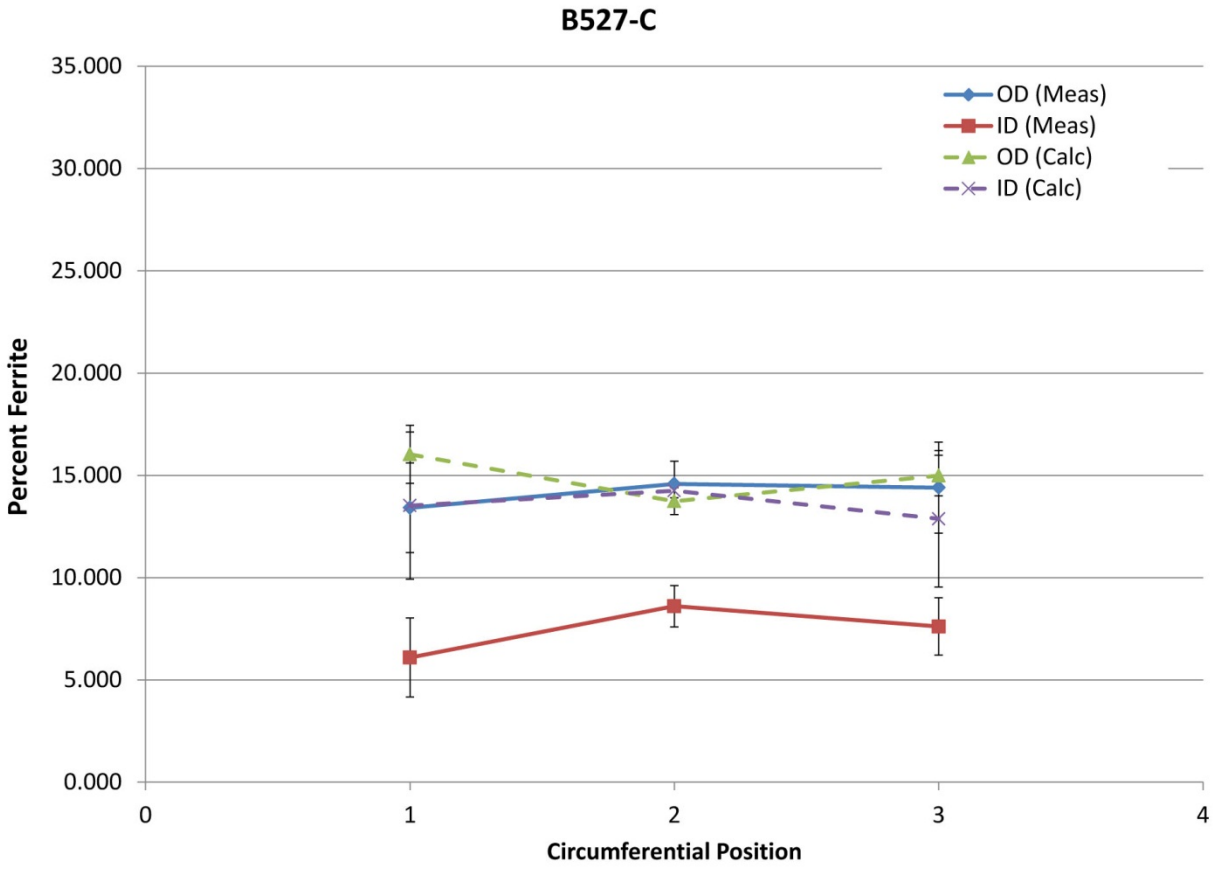

Figure B.3. Calculated Ferrite Concentrations Derived from XRF Measurements and Measured Ferrite Concentrations are Plotted with Respect to Circumferential Position on Specimen B527-C. Data are averaged over axial locations and the error bars represent one standard deviation. Measured ferrite concentrations exclude data within the weld.

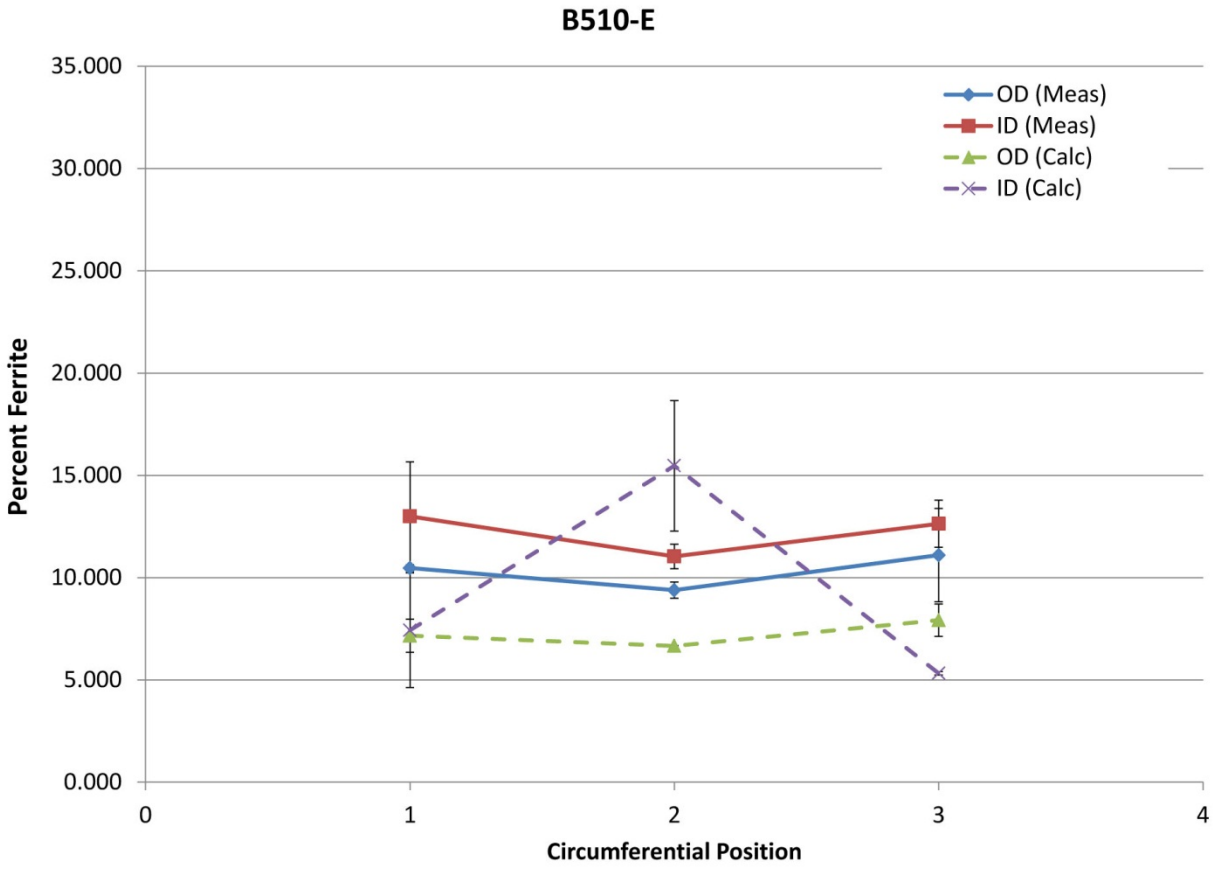

Figure B.4. Calculated Ferrite Concentrations Derived from XRF Measurements and Measured Ferrite Concentrations are Plotted with Respect to Circumferential Position on Specimen B510-E. Data are averaged over axial locations and the error bars represent one standard deviation. Measured ferrite concentrations exclude data within the weld.

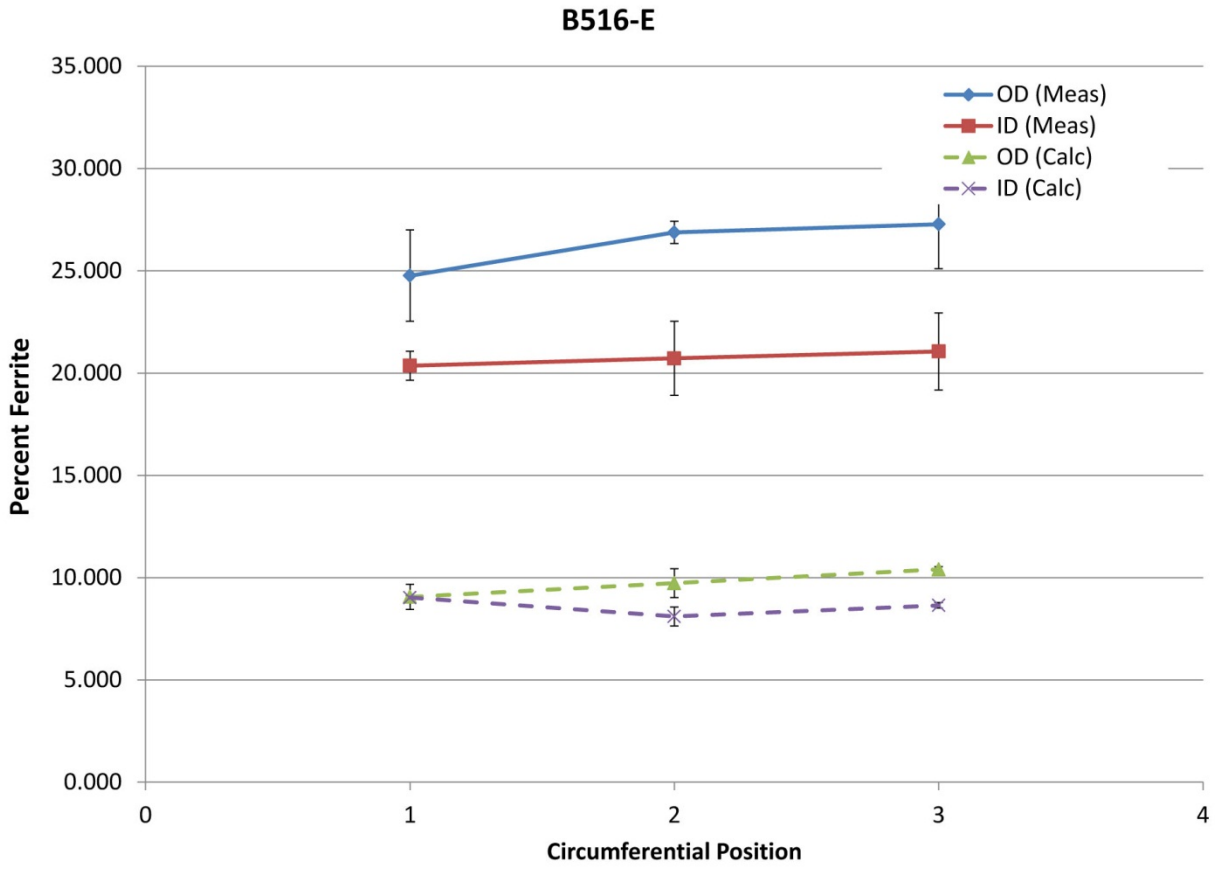

Figure B.5. Calculated Ferrite Concentrations Derived from XRF Measurements and Measured Ferrite Concentrations are Plotted with Respect to Circumferential Position on Specimen B516-E. Data are averaged over axial locations and the error bars represent one standard deviation. Measured ferrite concentrations exclude data within the weld.

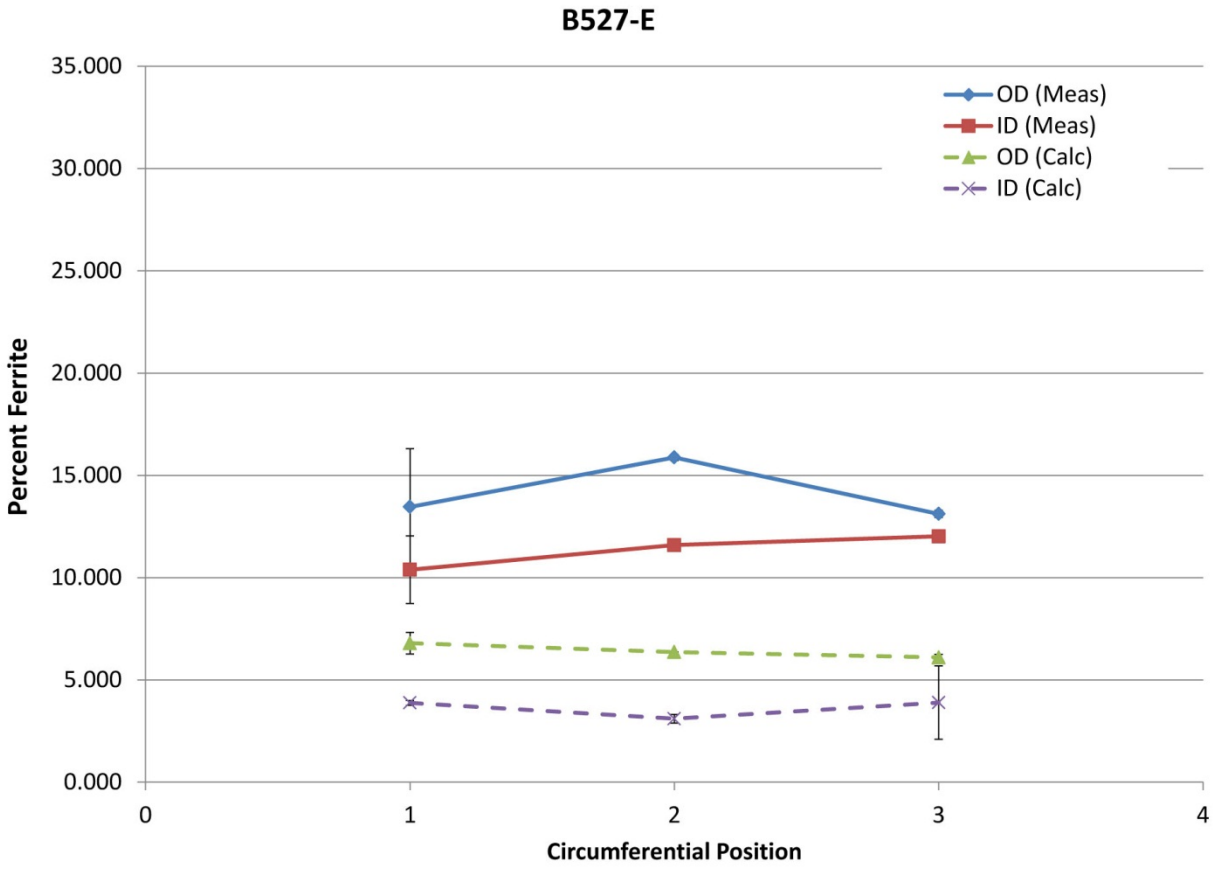

Figure B.6. Calculated Ferrite Concentrations Derived from XRF Measurements and Measured Ferrite Concentrations are Plotted with Respect to Circumferential Position on Specimen B527-E. Data are averaged over axial locations and the error bars represent one standard deviation. Measured ferrite concentrations exclude data within the weld.

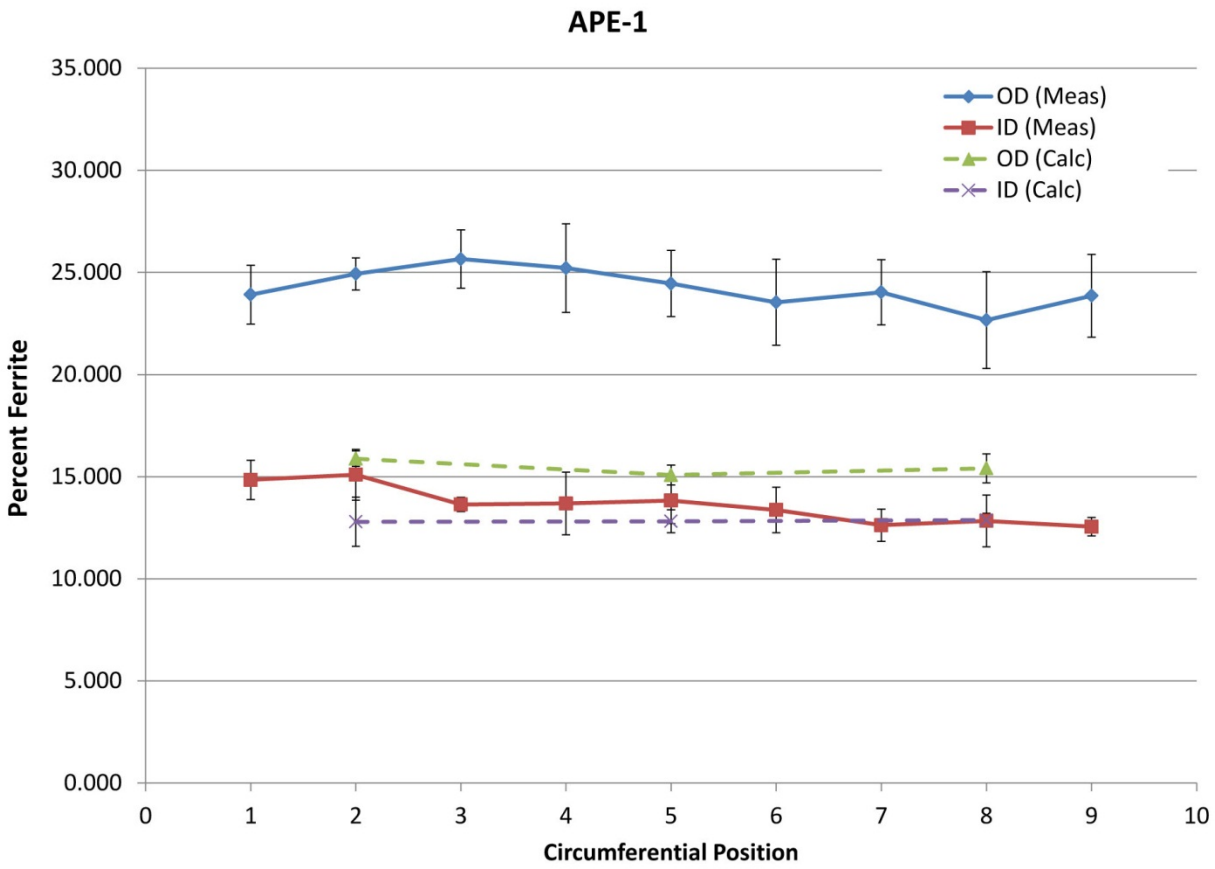

Figure B.7. Calculated Ferrite Concentrations Derived from XRF Measurements and Measured Ferrite Concentrations are Plotted with Respect to Circumferential Position on Specimen APE-1. Data are averaged over axial locations and the error bars represent one standard deviation. Measured ferrite concentrations exclude data within the weld.

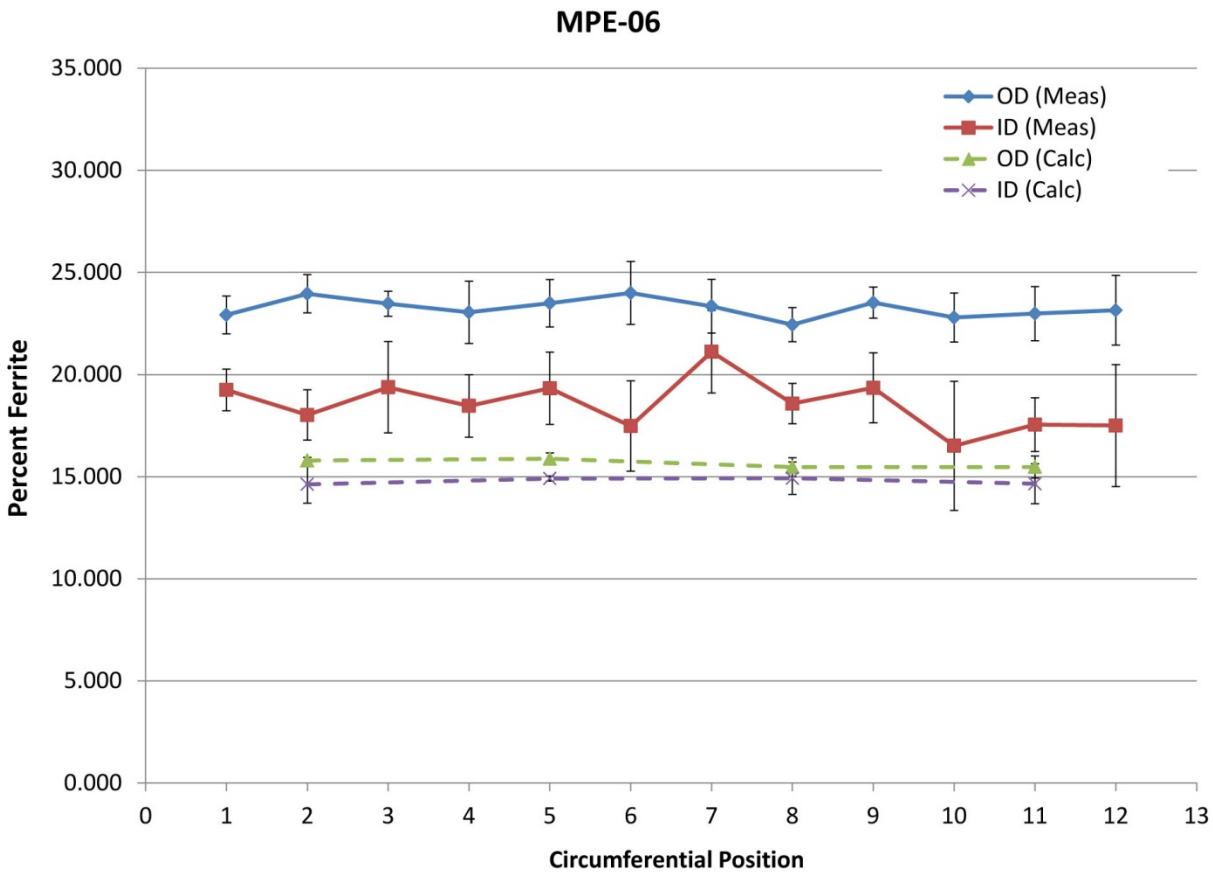

Figure B.8. Calculated Ferrite Concentrations Derived from XRF Measurements and Measured Ferrite Concentrations are Plotted with Respect to Circumferential Position on Specimen MPE-6. Data are averaged over axial locations and the error bars represent one standard deviation. Measured ferrite concentrations exclude data within the weld.

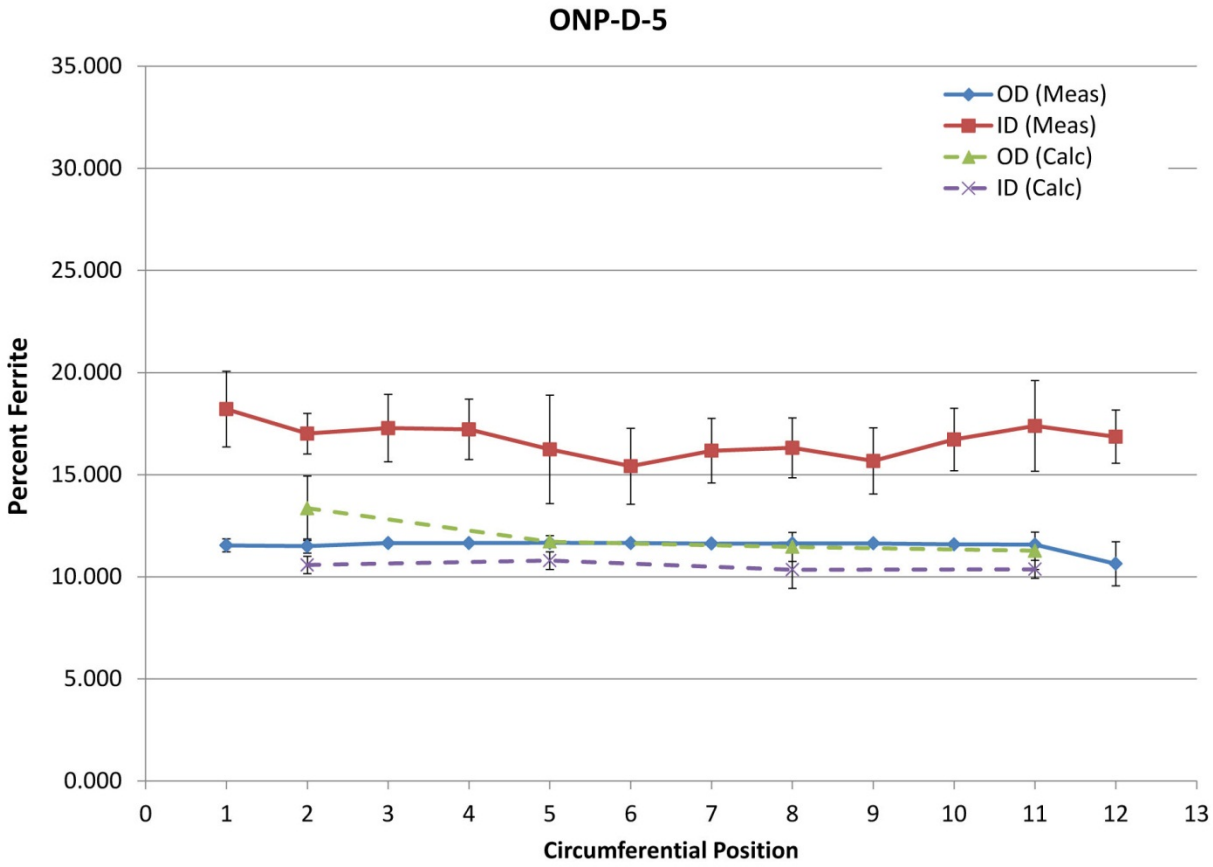

Figure B.9. Calculated Ferrite Concentrations Derived from XRF Measurements and Measured Ferrite Concentrations are Plotted with Respect to Circumferential Position on Specimen ONP-D-5. Data are averaged over axial locations and the error bars represent one standard deviation. Measured ferrite concentrations exclude data within the weld.

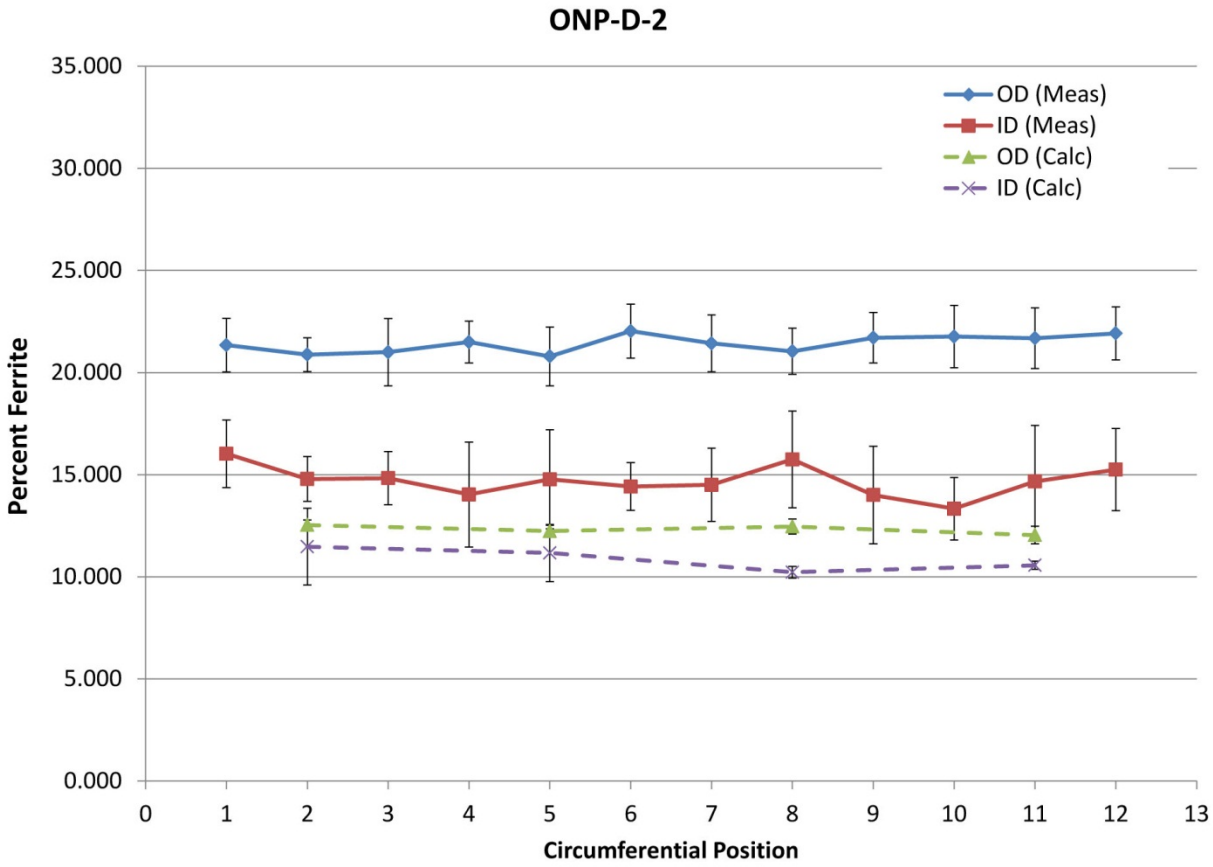

Figure B.10. Calculated Ferrite Concentrations Derived from XRF Measurements and Measured Ferrite Concentrations are Plotted with Respect to Circumferential Position on Specimen ONP-D-2. Data are averaged over axial locations and the error bars represent one standard deviation. Measured ferrite concentrations exclude data within the weld.

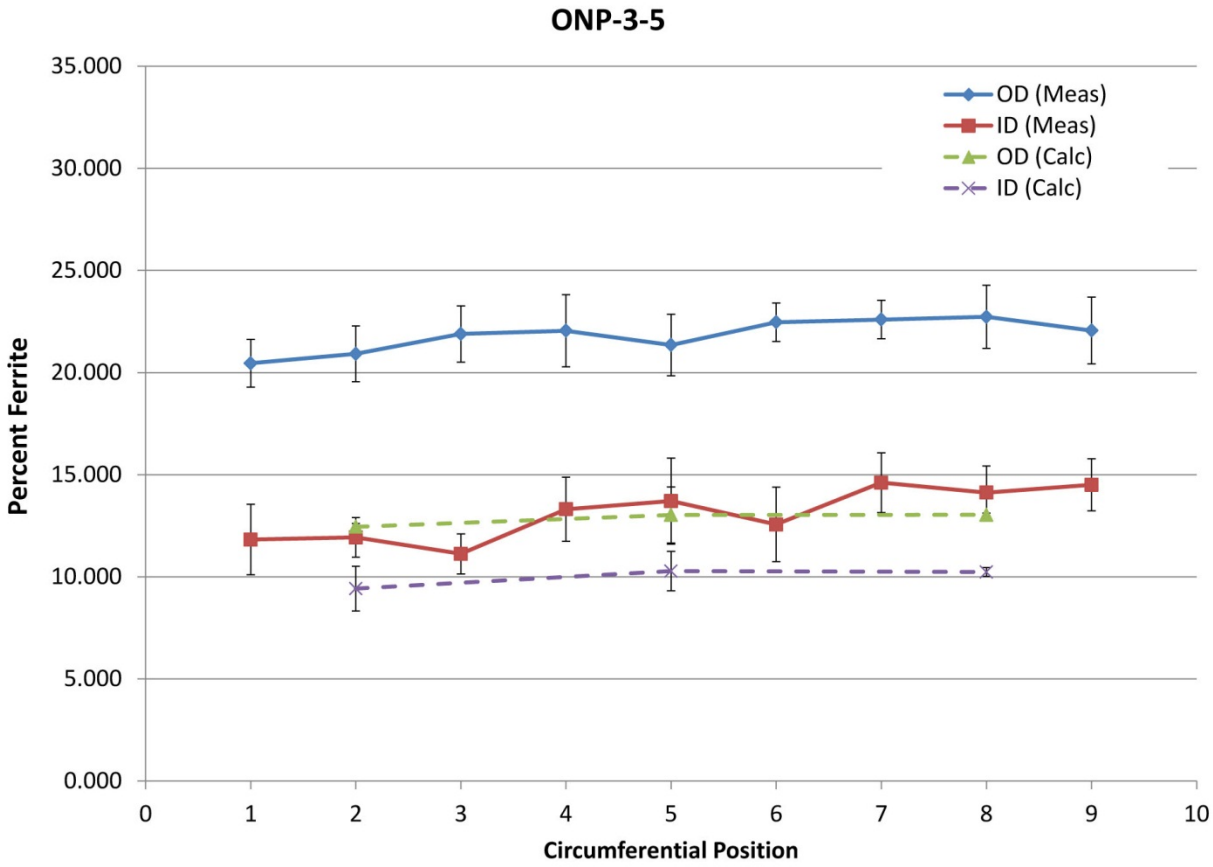

Figure B.11. Calculated Ferrite Concentrations Derived from XRF Measurements and Measured Ferrite Concentrations are Plotted with Respect to Circumferential Position on Specimen ONP-3-5. Data are averaged over axial locations and the error bars represent one standard deviation. Measured ferrite concentrations exclude data within the weld.

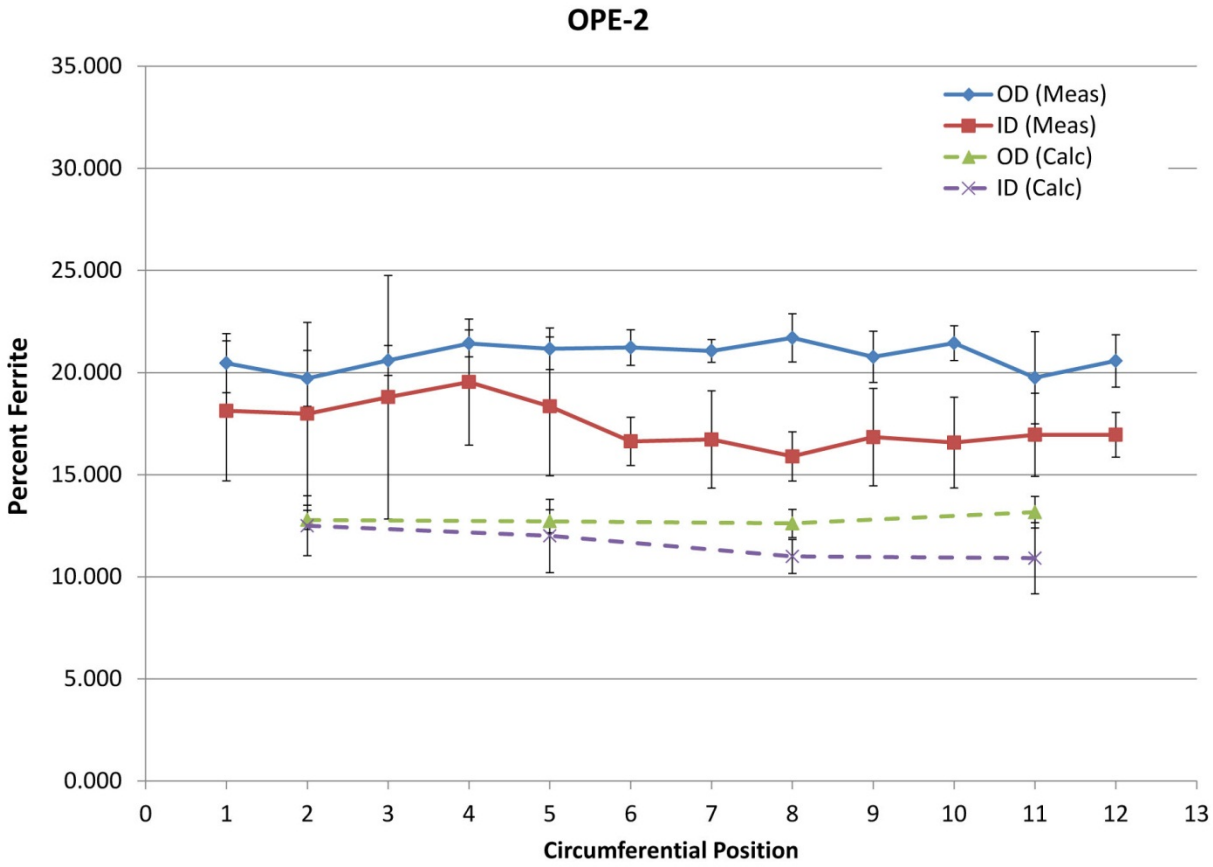

Figure B.12. Calculated Ferrite Concentrations Derived from XRF Measurements and Measured Ferrite Concentrations are Plotted with Respect to Circumferential Position on Specimen OPE-2. Data are averaged over axial locations and the error bars represent one standard deviation. Measured ferrite concentrations exclude data within the weld.

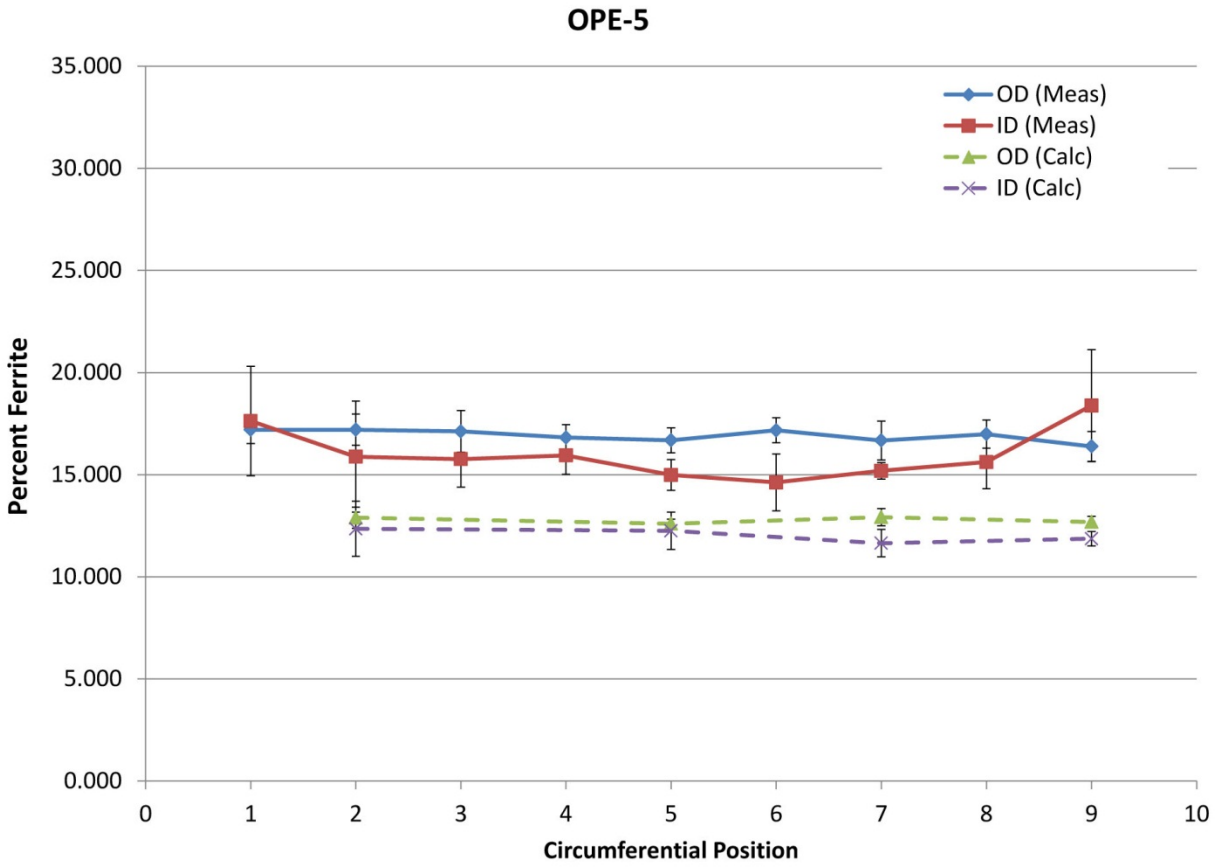

Figure B.13. Calculated Ferrite Concentrations Derived from XRF Measurements and Measured Ferrite Concentrations are Plotted with Respect to Circumferential Position on Specimen OPE-5. Data are averaged over axial locations and the error bars represent one standard deviation. Measured ferrite concentrations exclude data within the weld.

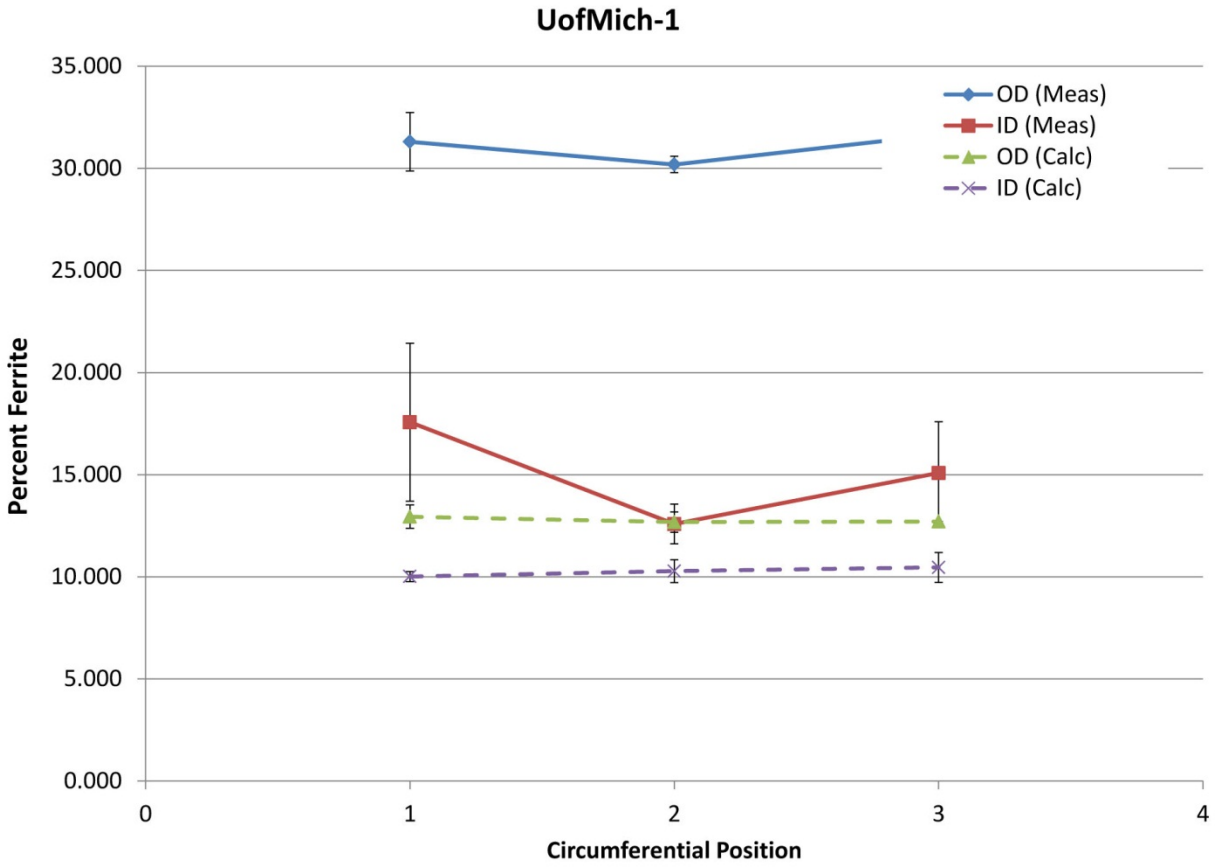

Figure B.14. Calculated Ferrite Concentrations Derived from XRF Measurements and Measured Ferrite Concentrations are Plotted with Respect to Circumferential Position on Specimen UofMich-1. Data are averaged over axial locations and the error bars represent one standard deviation. Measured ferrite concentrations exclude data within the weld.

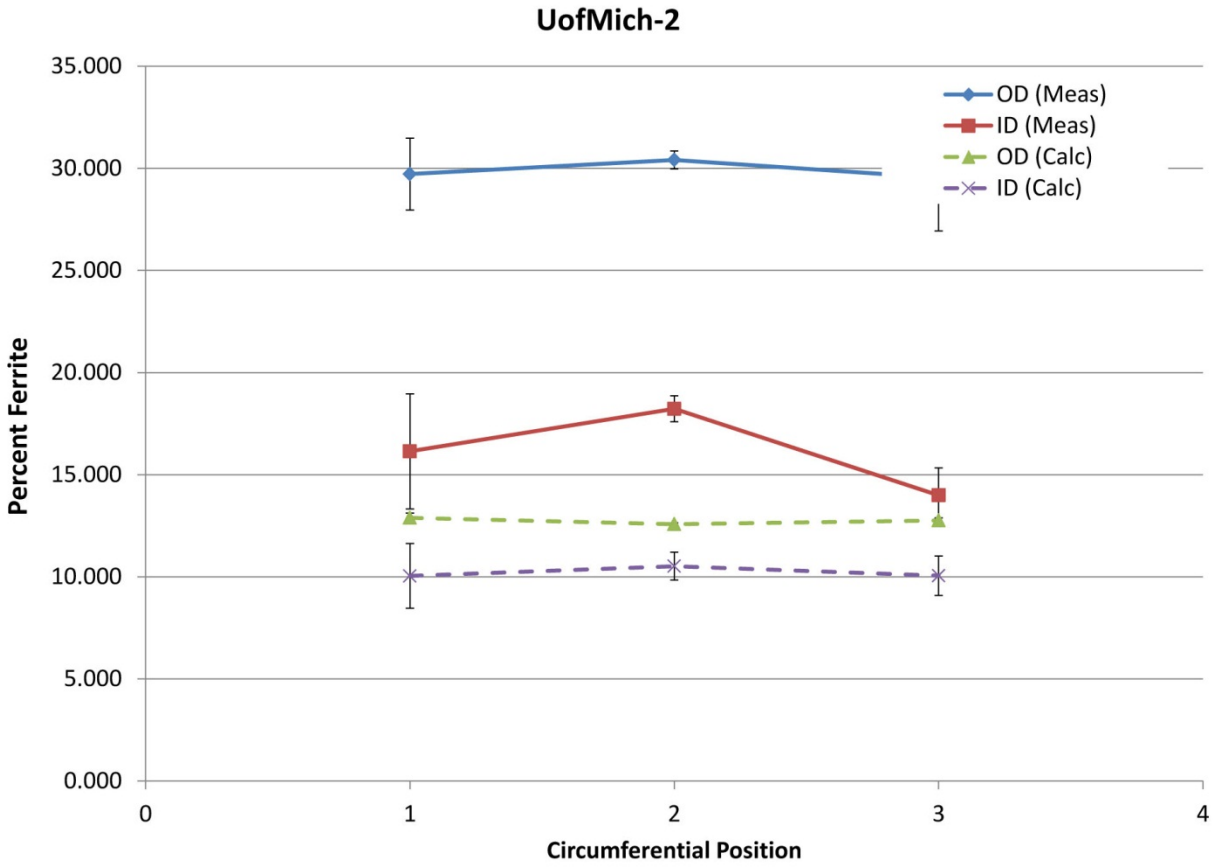

Figure B.15. Calculated Ferrite Concentrations Derived from XRF Measurements and Measured Ferrite Concentrations are Plotted with Respect to Circumferential Position on Specimen UofMich-2. Data are averaged over axial locations and the error bars represent one standard deviation. Measured ferrite concentrations exclude data within the weld.

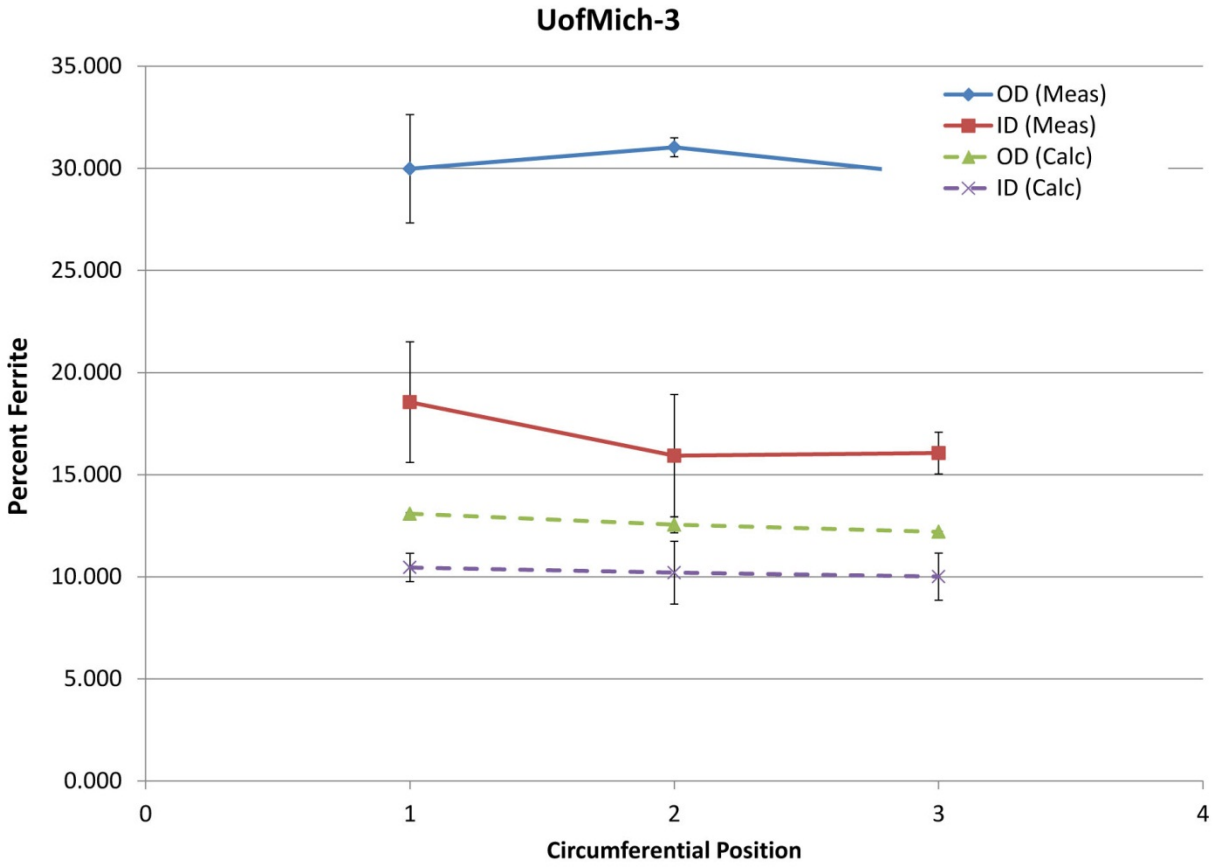

Figure B.16. Calculated Ferrite Concentrations Derived from XRF Measurements and Measured Ferrite Concentrations are Plotted with Respect to Circumferential Position on Specimen UofMich-3. Data are averaged over axial locations and the error bars represent one standard deviation. Measured ferrite concentrations exclude data within the weld.

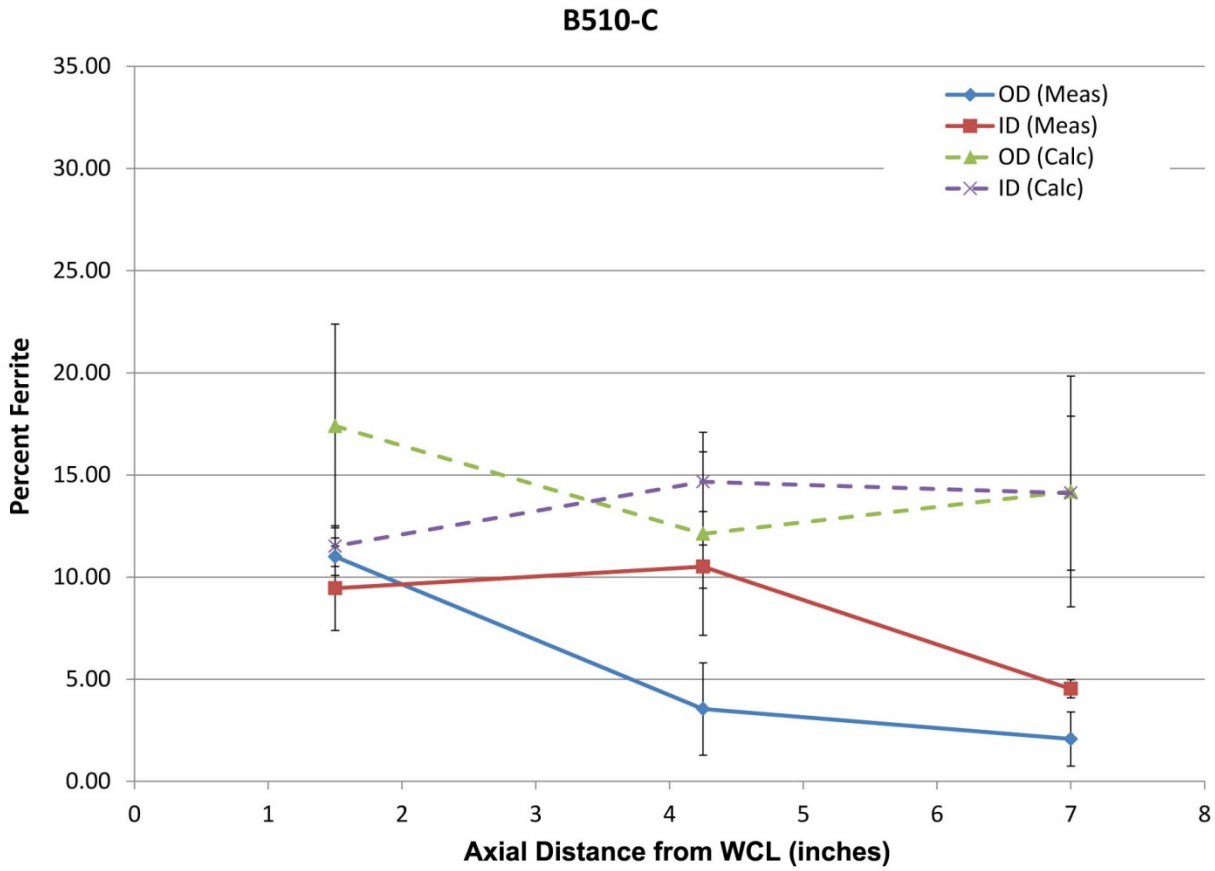

Figure B.17. Calculated Ferrite Concentrations Derived from XRF Measurements and Measured Ferrite Concentrations are Plotted with Respect to Distance from the W_{CL} on Specimen B510-C. Data are averaged over circumferential locations and the error bars represent one standard deviation.

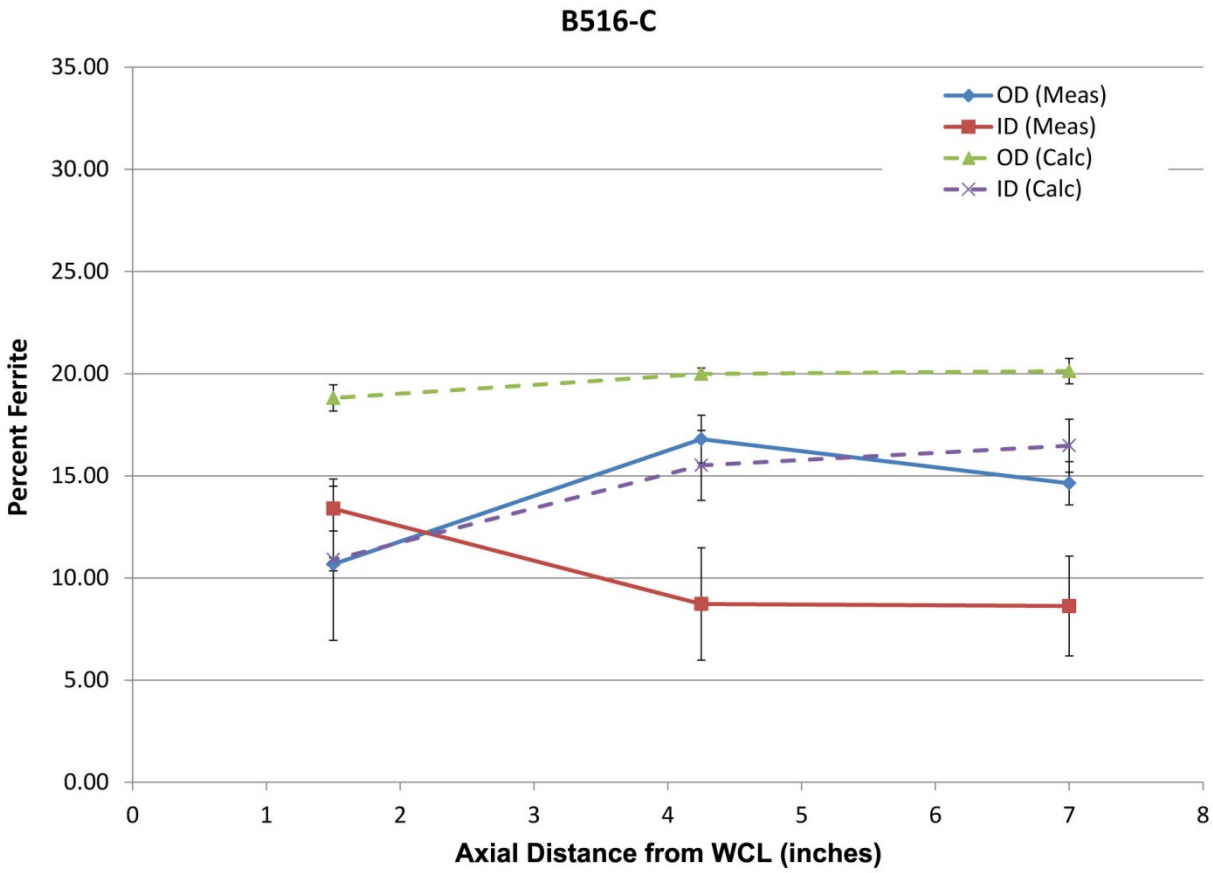

Figure B.18. Calculated Ferrite Concentrations Derived from XRF Measurements and Measured Ferrite Concentrations are Plotted with Respect to Distance from the W_{CL} on Specimen B516-C. Data are averaged over circumferential locations and the error bars represent one standard deviation.

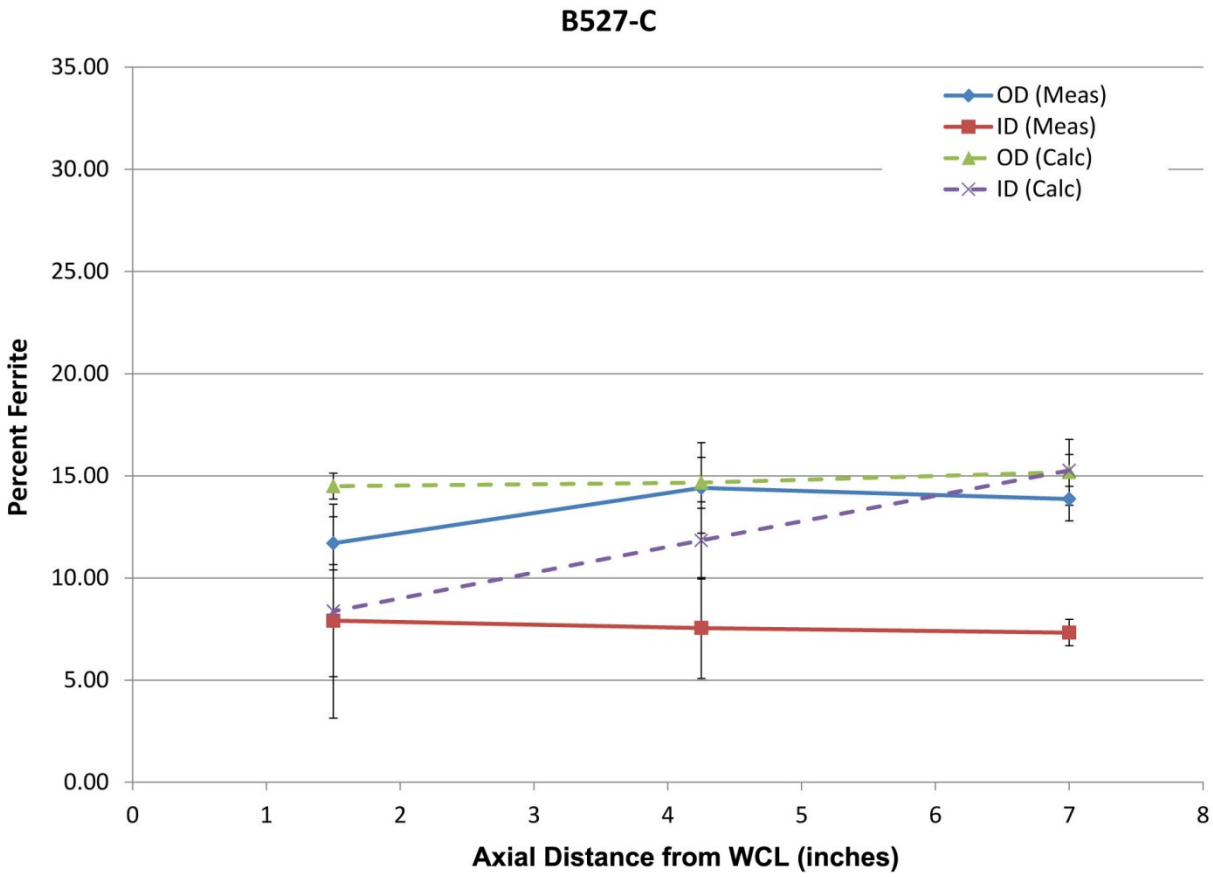

Figure B.19. Calculated Ferrite Concentrations Derived from XRF Measurements and Measured Ferrite Concentrations are Plotted with Respect to Distance from the W_{CL} on Specimen B527-C. Data are averaged over circumferential locations and the error bars represent one standard deviation.

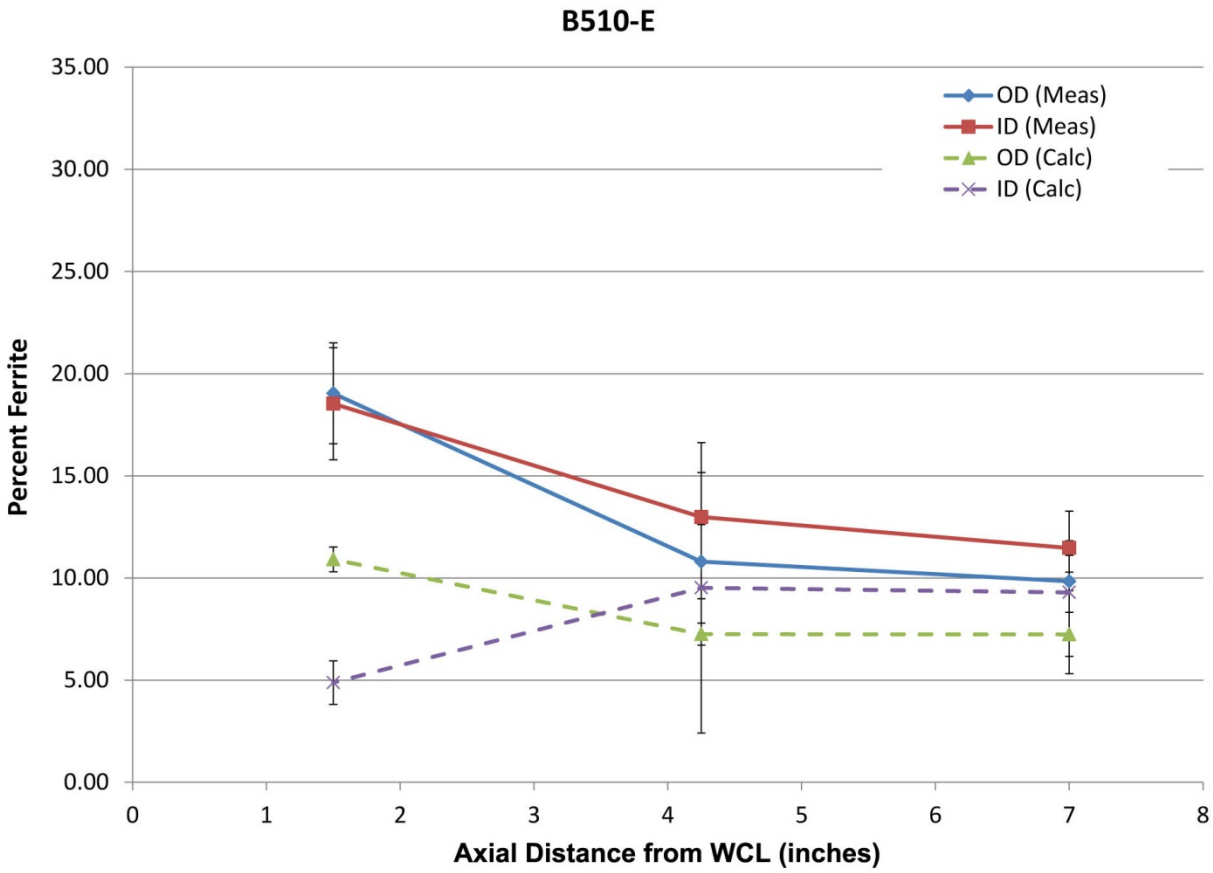

Figure B.20. Calculated Ferrite Concentrations Derived from XRF Measurements and Measured Ferrite Concentrations are Plotted with Respect to Distance from the W_{CL} on Specimen B510-E. Data are averaged over circumferential locations and the error bars represent one standard deviation.

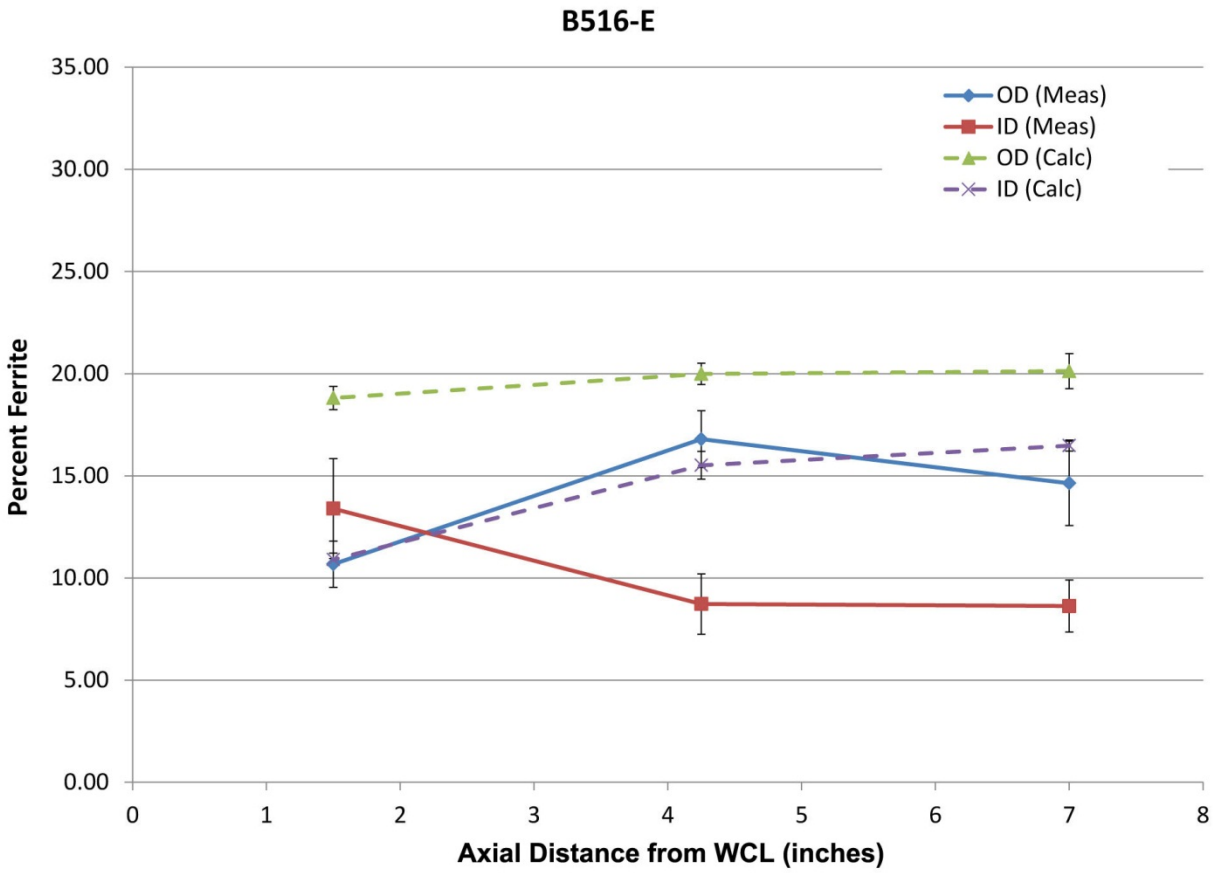

Figure B.21. Calculated Ferrite Concentrations Derived from XRF Measurements and Measured Ferrite Concentrations are Plotted with Respect to Distance from the W_{CL} on Specimen B516-E. Data are averaged over circumferential locations and the error bars represent one standard deviation.

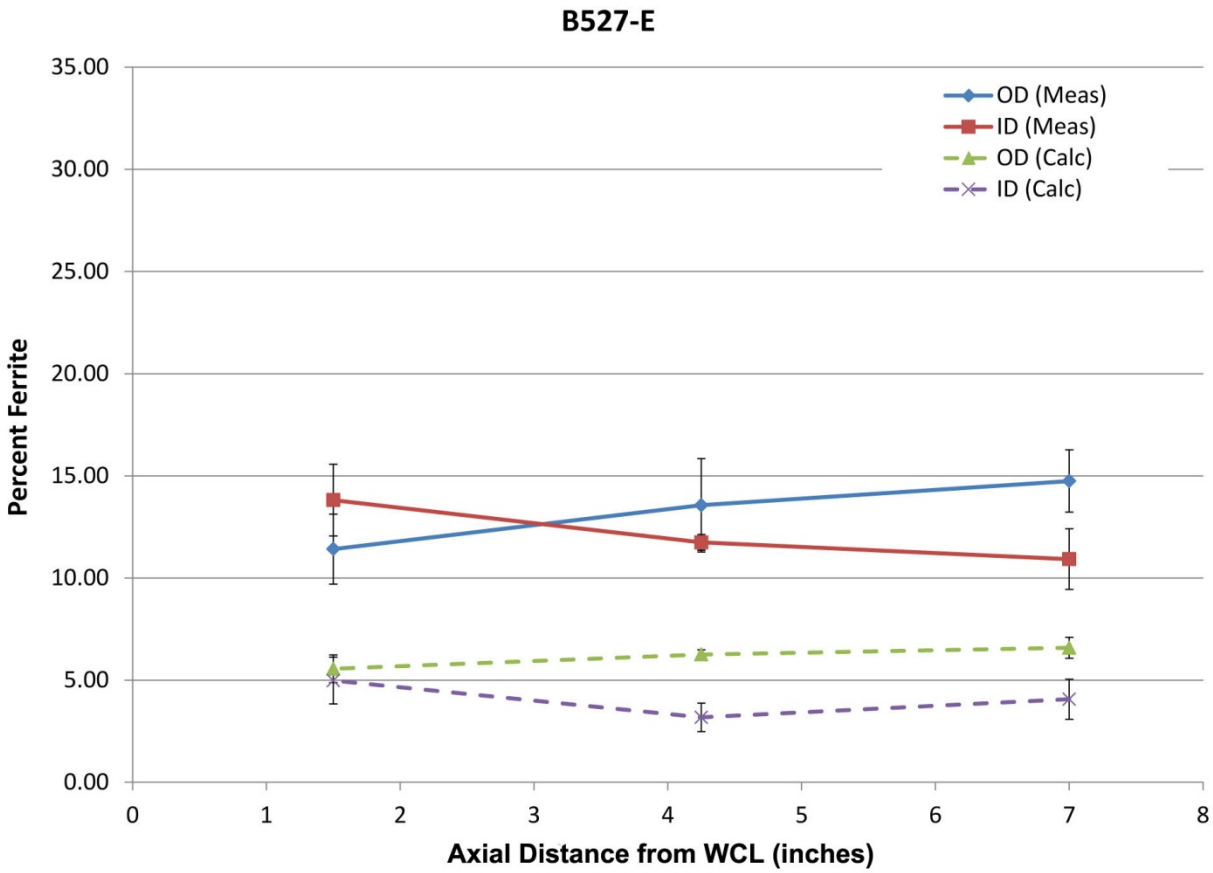

Figure B.22. Calculated Ferrite Concentrations Derived from XRF Measurements and Measured Ferrite Concentrations are Plotted with Respect to Distance from the W_{CL} on Specimen B527-E. Data are averaged over circumferential locations and the error bars represent one standard deviation.

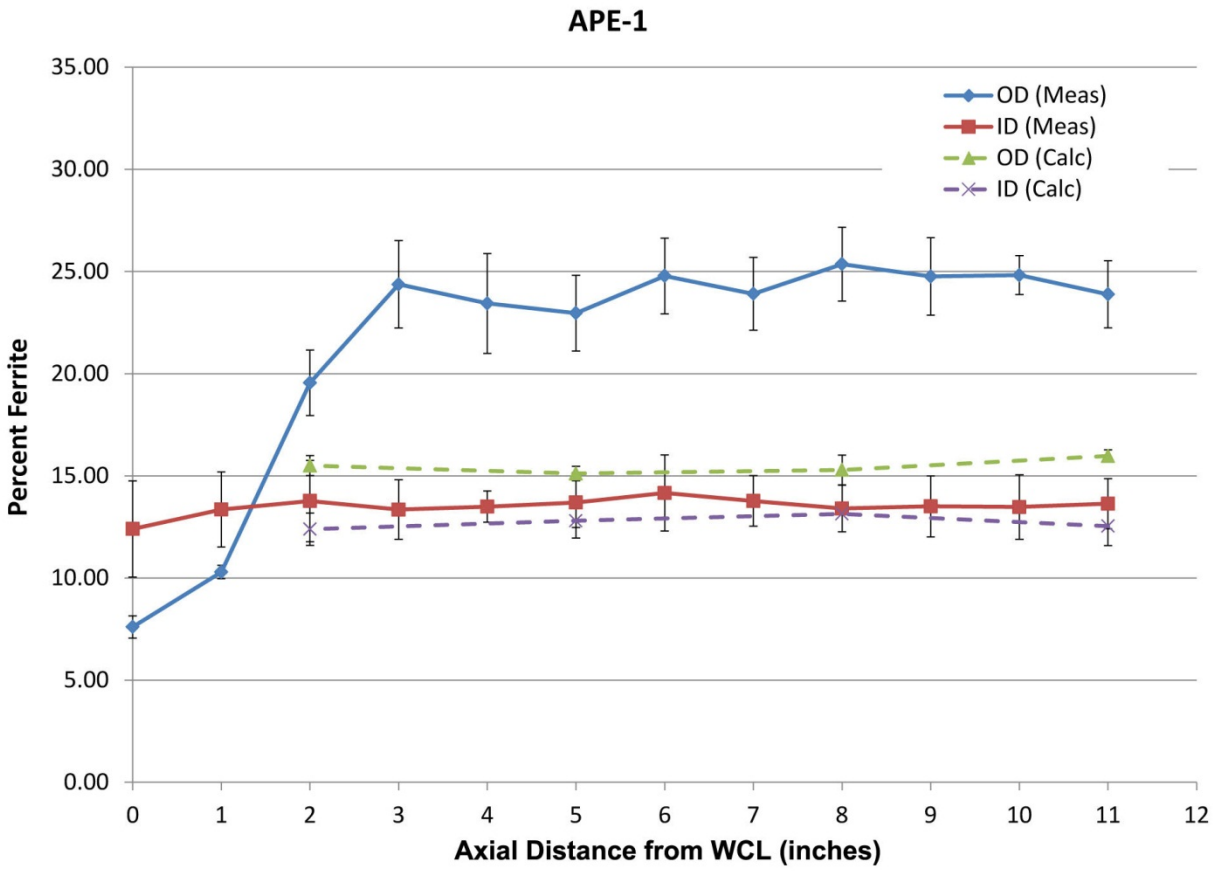

Figure B.23. Calculated Ferrite Concentrations Derived from XRF Measurements and Measured Ferrite Concentrations are Plotted with Respect to Distance from the W_{CL} on Specimen APE-1. Data are averaged over circumferential locations and the error bars represent one standard deviation.

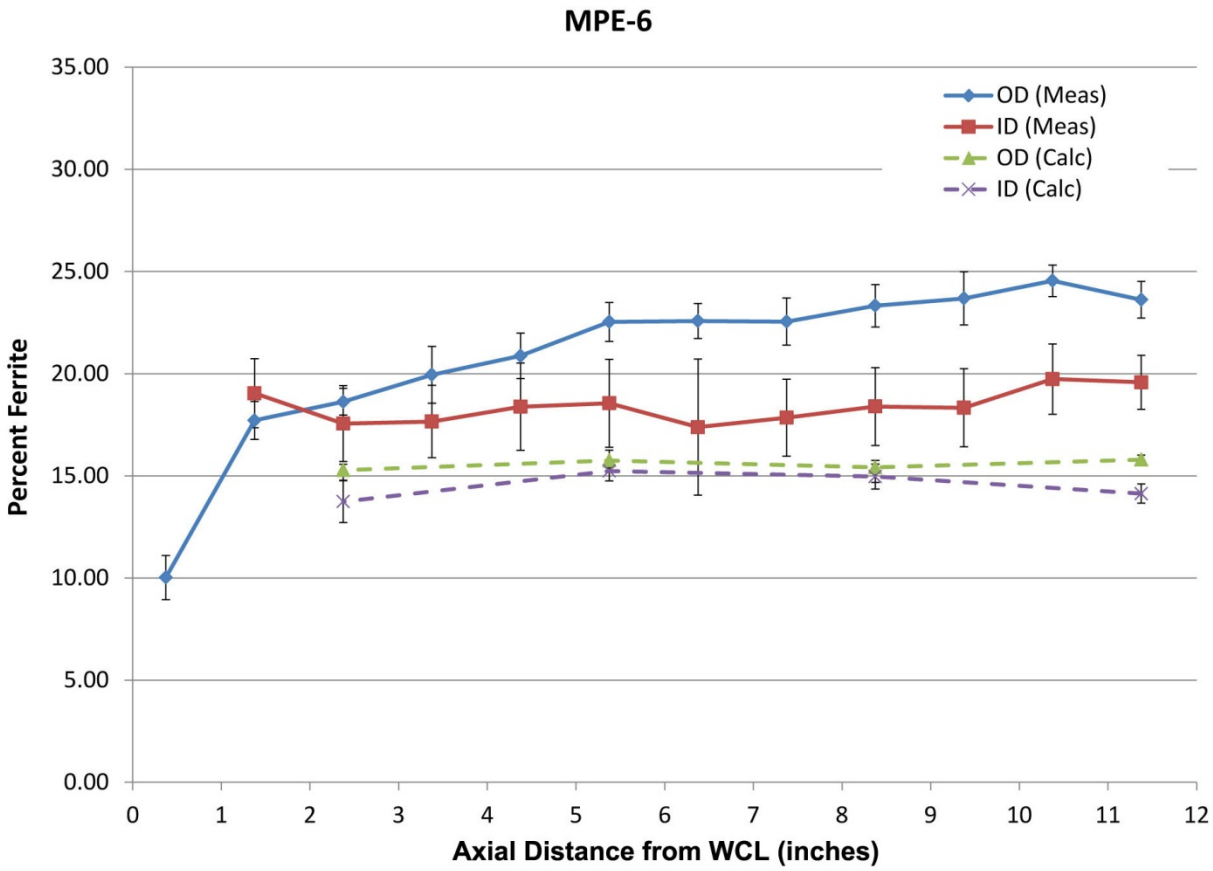

Figure B.24. Calculated Ferrite Concentrations Derived from XRF Measurements and Measured Ferrite Concentrations are Plotted with Respect to Distance from the W_{CL} on Specimen MPE-6. Data are averaged over circumferential locations and the error bars represent one standard deviation.

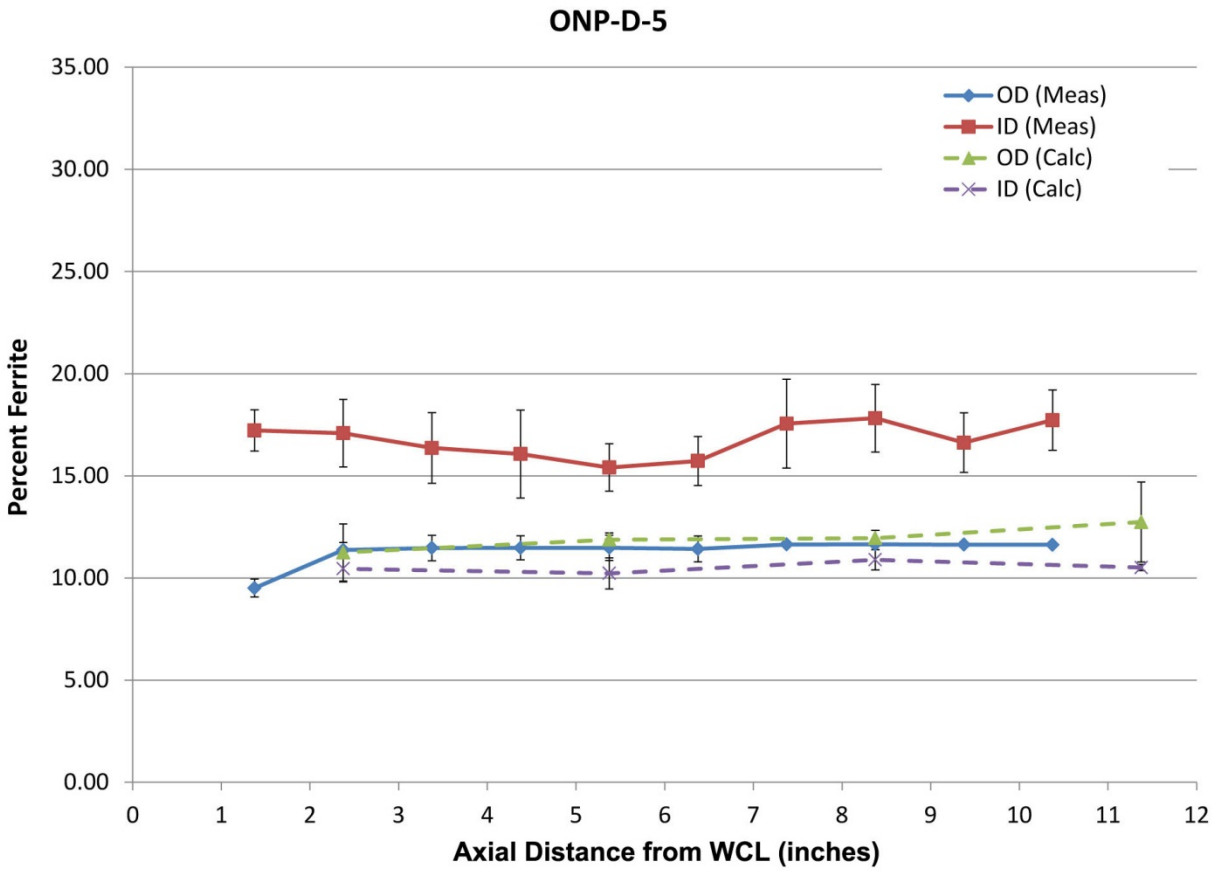

Figure B.25. Calculated Ferrite Concentrations Derived from XRF Measurements and Measured Ferrite Concentrations are Plotted with Respect to Distance from the W_{CL} on Specimen ONP-D-5. Data are averaged over circumferential locations and the error bars represent one standard deviation.

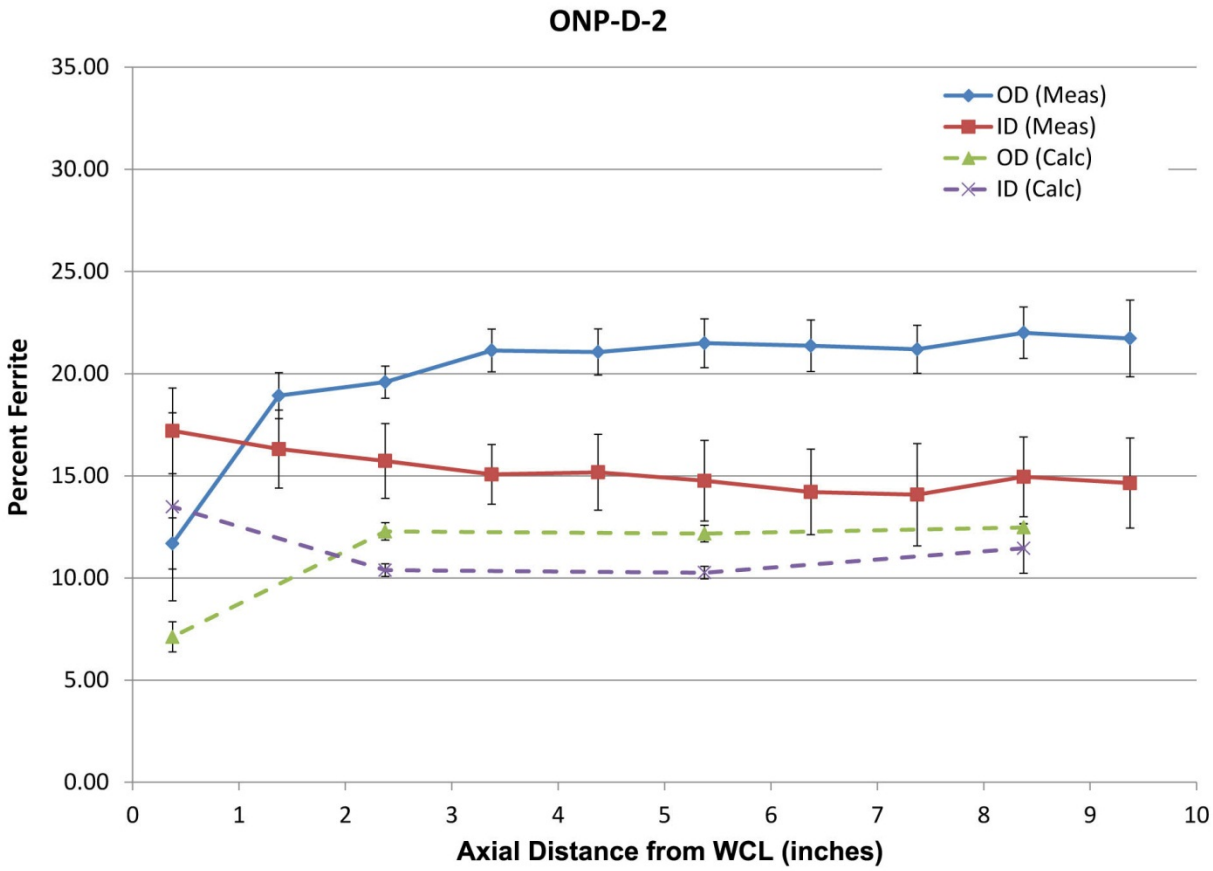

Figure B.26. Calculated Ferrite Concentrations Derived from XRF Measurements and Measured Ferrite Concentrations are Plotted with Respect to Distance from the W_{CL} on Specimen ONP-D-2. Data are averaged over circumferential locations and the error bars represent one standard deviation.

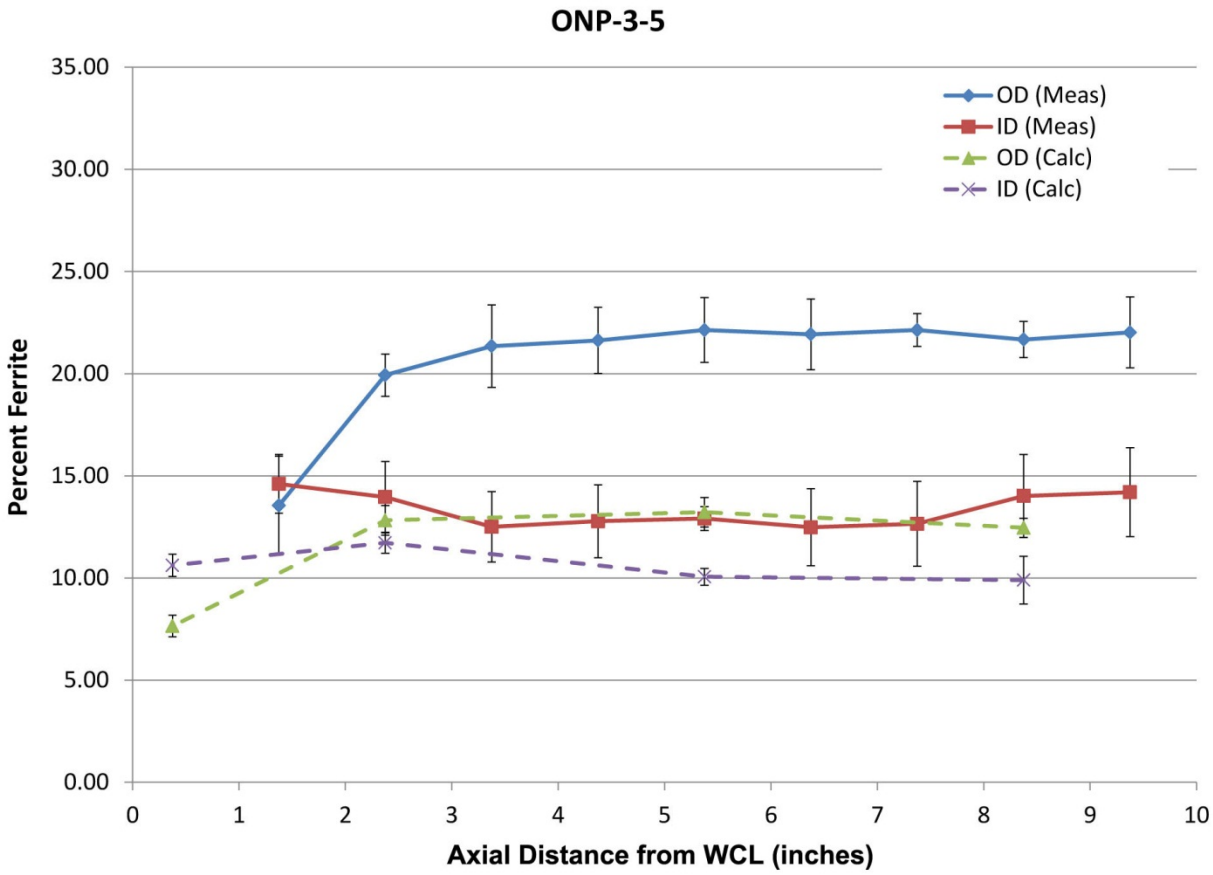

Figure B.27. Calculated Ferrite Concentrations Derived from XRF Measurements and Measured Ferrite Concentrations are Plotted with Respect to Distance from the W_{CL} on Specimen ONP-3-5. Data are averaged over circumferential locations and the error bars represent one standard deviation.

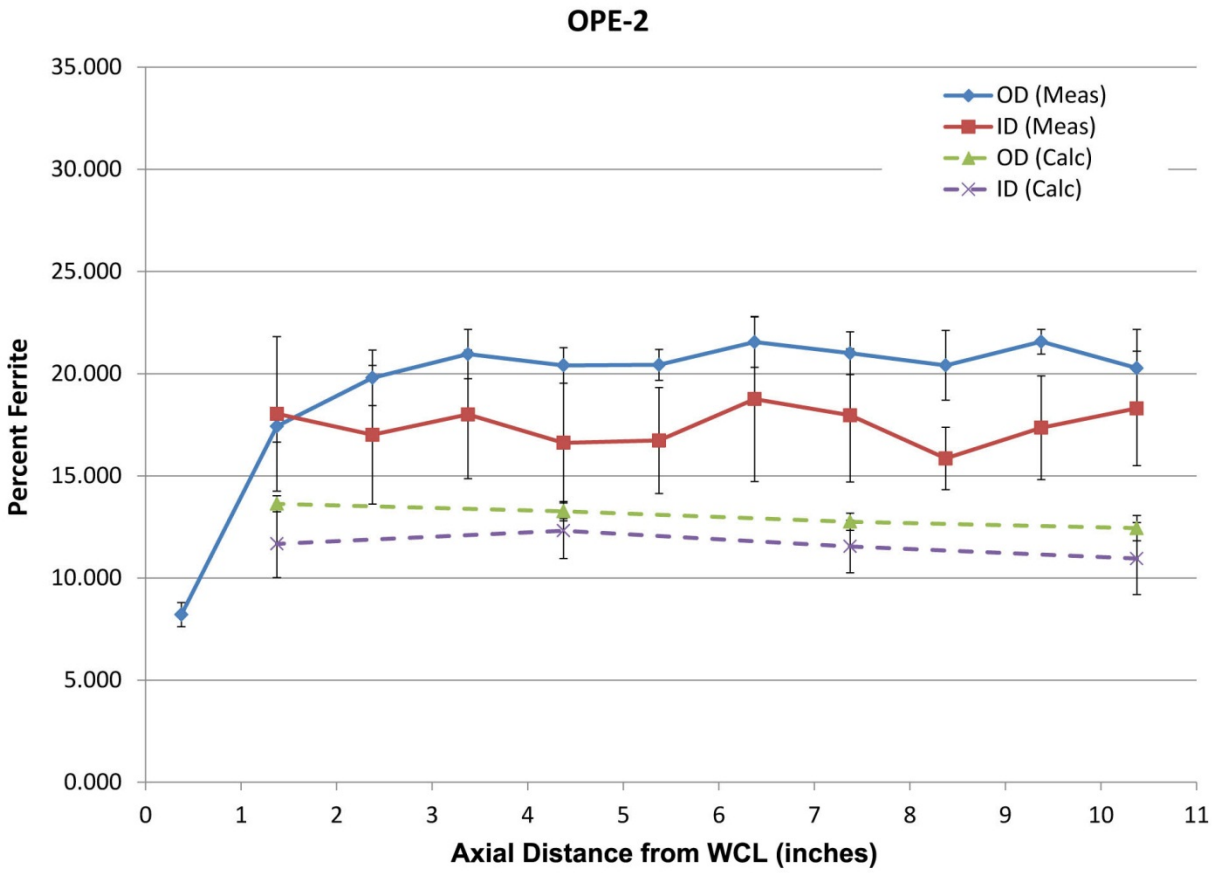

Figure B.28. Calculated Ferrite Concentrations Derived from XRF Measurements and Measured Ferrite Concentrations are Plotted with Respect to Distance from the W_{CL} on Specimen OPE-2. Data are averaged over circumferential locations and the error bars represent one standard deviation.

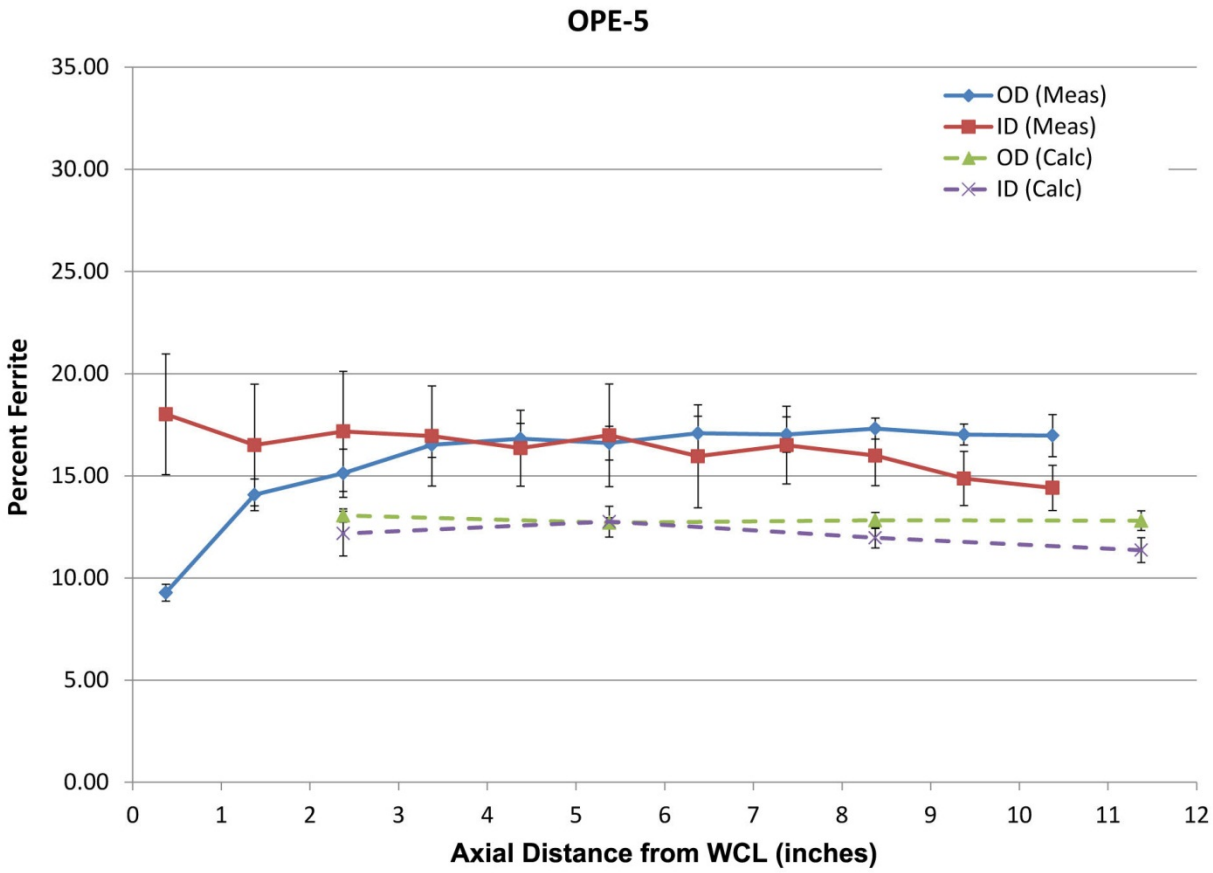

Figure B.29. Calculated Ferrite Concentrations Derived from XRF Measurements and Measured Ferrite Concentrations are Plotted with Respect to Distance from the W_{CL} on Specimen OPE-5. Data are averaged over circumferential locations and the error bars represent one standard deviation.

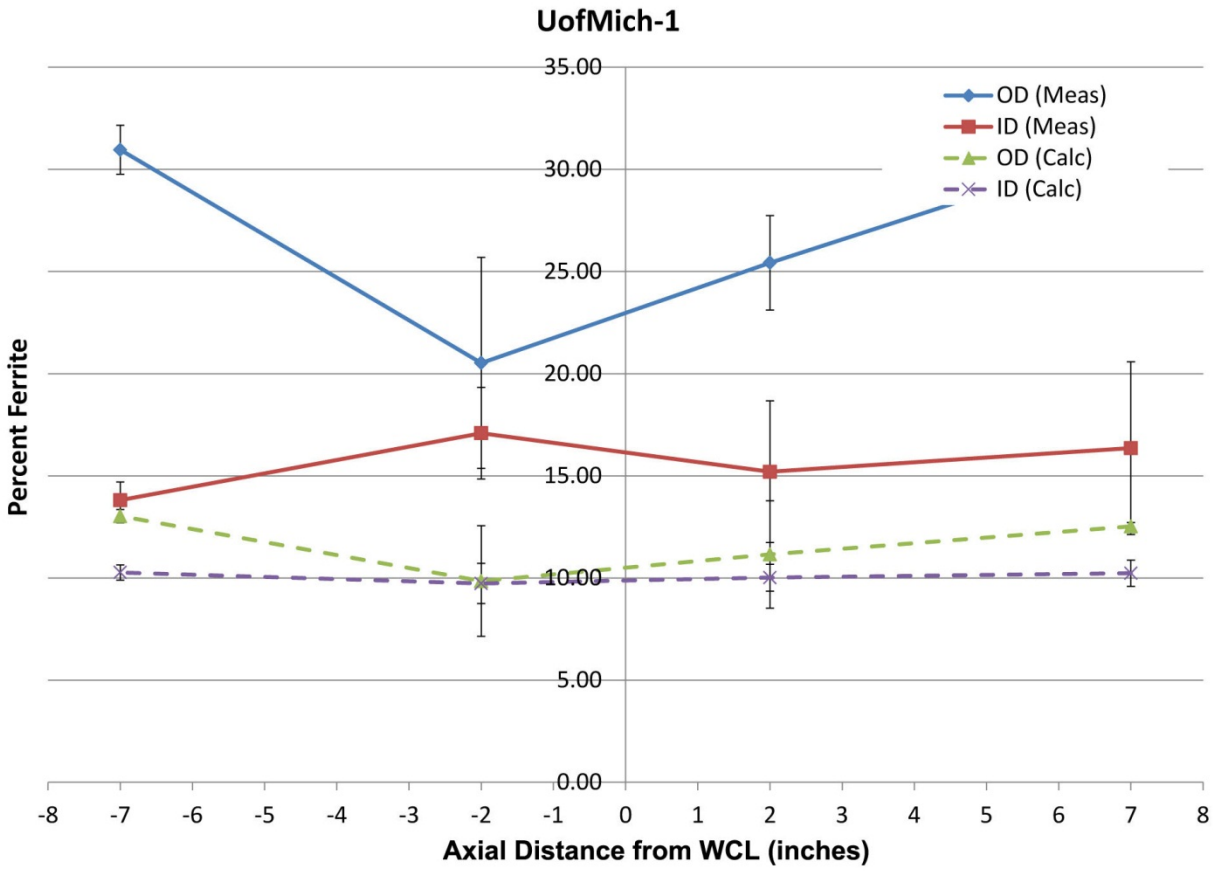

Figure B.30. Calculated Ferrite Concentrations Derived from XRF Measurements and Measured Ferrite Concentrations are Plotted with Respect to Distance from the W_{CL} on Specimen UofMich-1. Data are averaged over circumferential locations and the error bars represent one standard deviation.

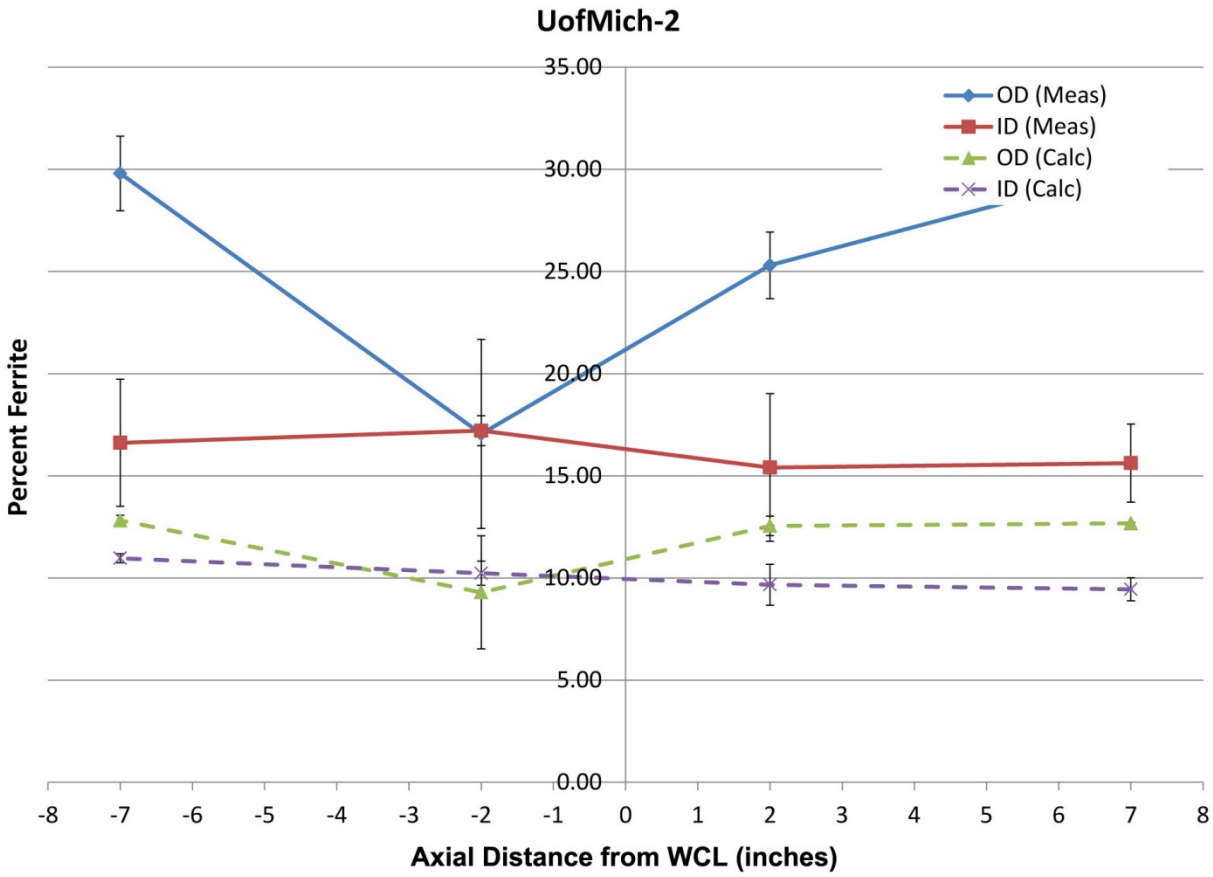

Figure B.31. Calculated Ferrite Concentrations Derived from XRF Measurements and Measured Ferrite Concentrations are Plotted with Respect to Distance from the W_{CL} on Specimen UofMich-2. Data are averaged over circumferential locations and the error bars represent one standard deviation.

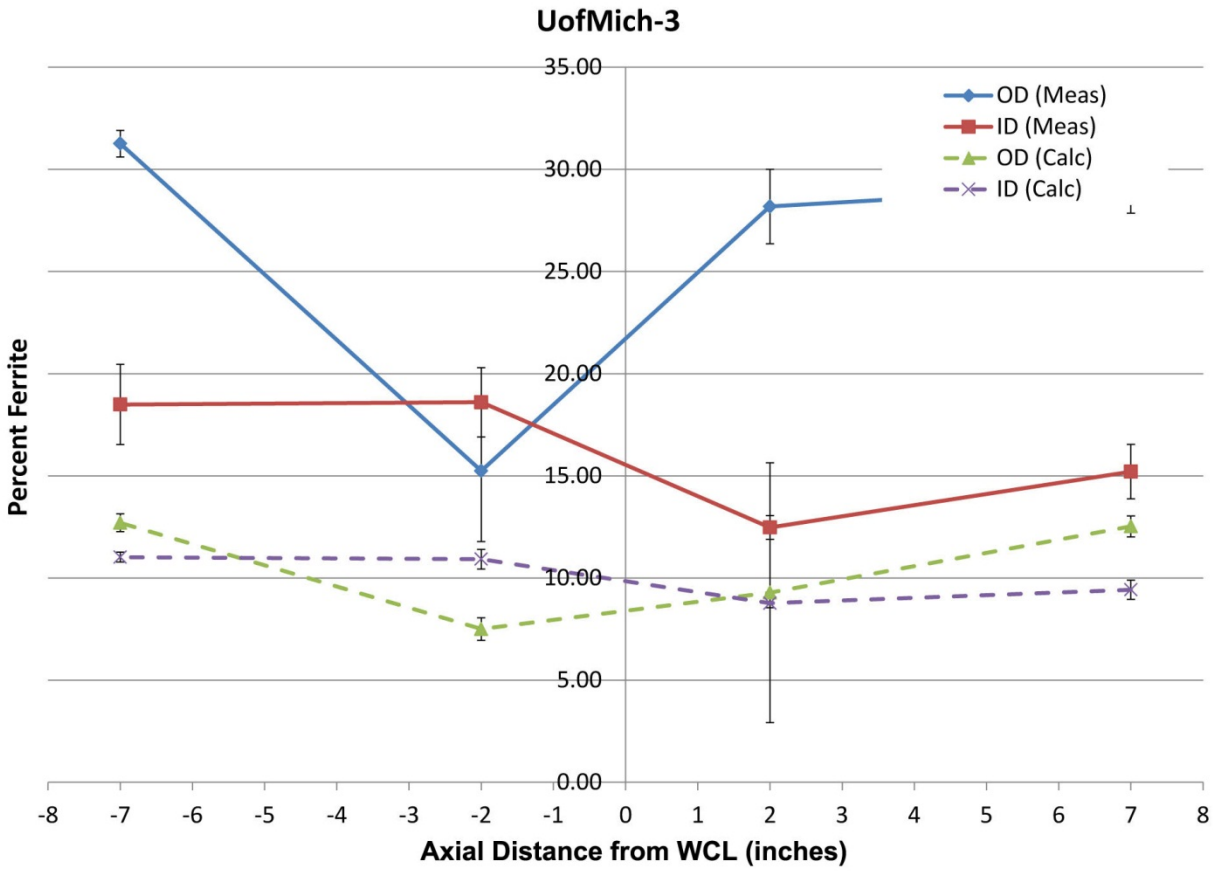

Figure B.32. Calculated Ferrite Concentrations Derived from XRF Measurements and Measured Ferrite Concentrations are Plotted with Respect to Distance from the W_{CL} on Specimen UofMich-3. Data are averaged over circumferential locations and the error bars represent one standard deviation.

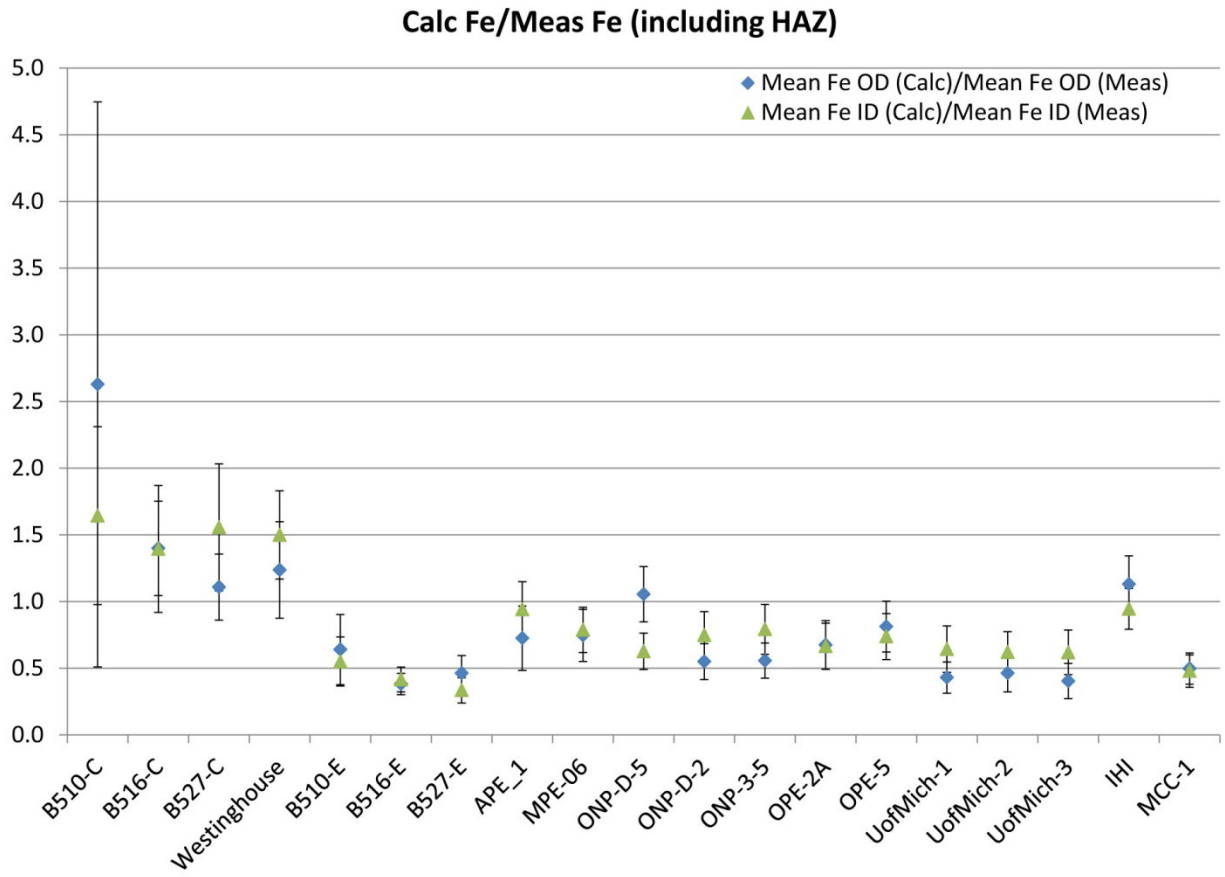

Figure B.33. Calculated and Measured Ferrite Concentrations are Compared for Each Specimen by Calculating the Ratio of the Mean Calculated Ferrite Concentration to the Mean Measured Ferrite Concentration. Error bars represent one standard deviation.

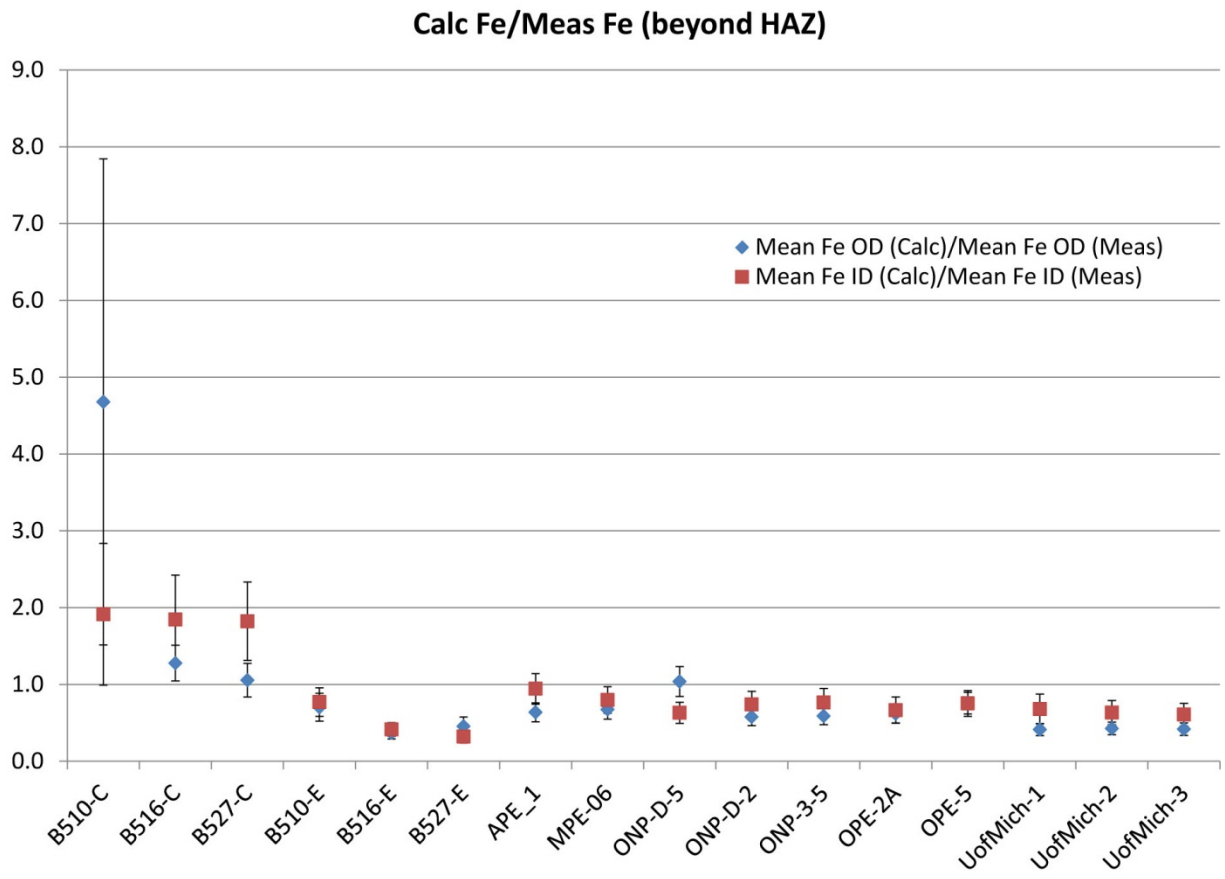

Figure B.34. Calculated and Measured Ferrite Concentrations are Compared for Each Specimen by Calculating the Ratio of the Mean Calculated Ferrite Concentration to the Mean Measured Ferrite Concentration. Error bars represent one standard deviation. Ferrite measurements within the weld are excluded in this plot.

Appendix C

XRF-measured Elemental Content in CASS Specimens

Appendix C

XRF-measured Elemental Content in CASS Specimens

Appendix C compares the elemental content (in mass percent) of different elements for each of the specimens examined in this study. Each plot presents the mean and standard deviation of a single element (such as manganese in Figure C.1) in each of the specimens, using XRF measurements on the OD and ID surfaces.

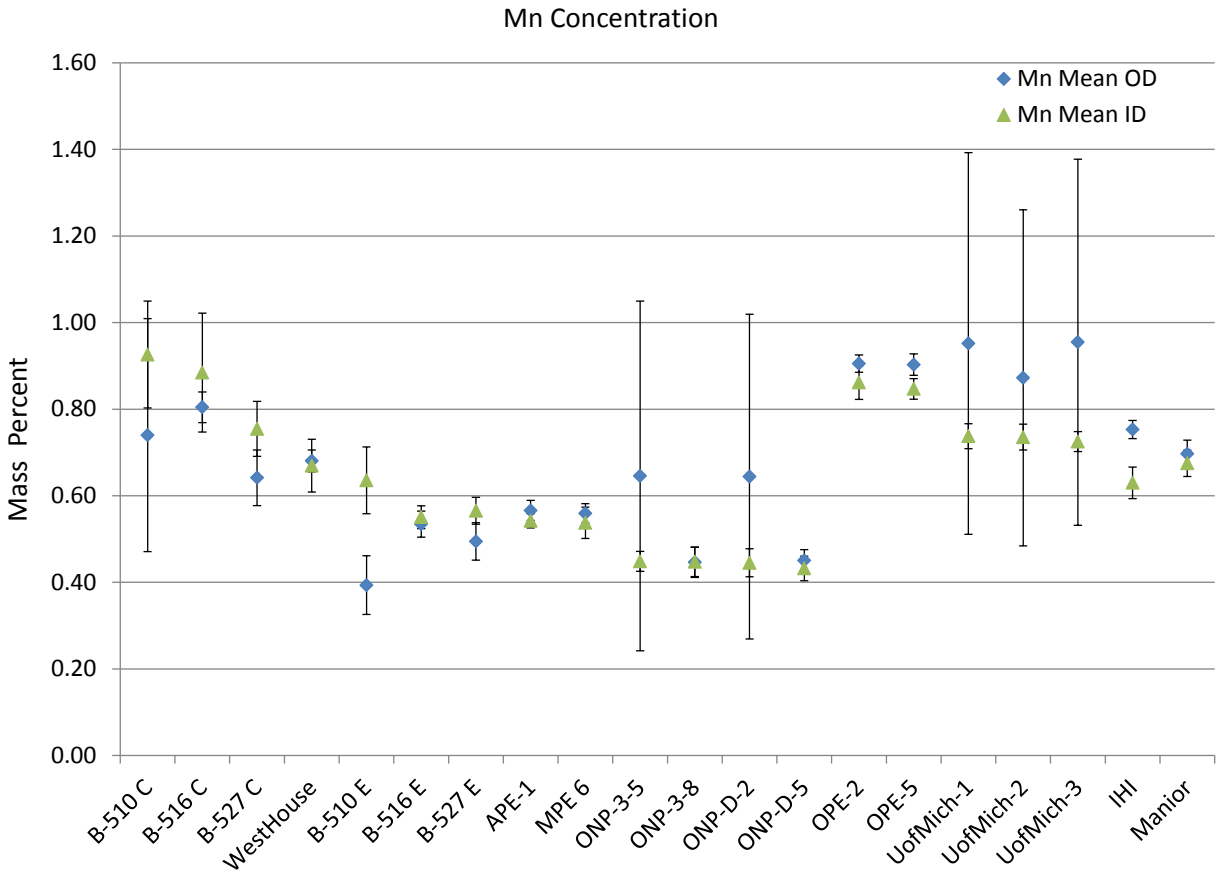

Figure C.1. Mean Mn Concentration Obtained from XRF Measurements are Plotted for OD and ID Surfaces of Each Specimen. Error bars represent one standard deviation.

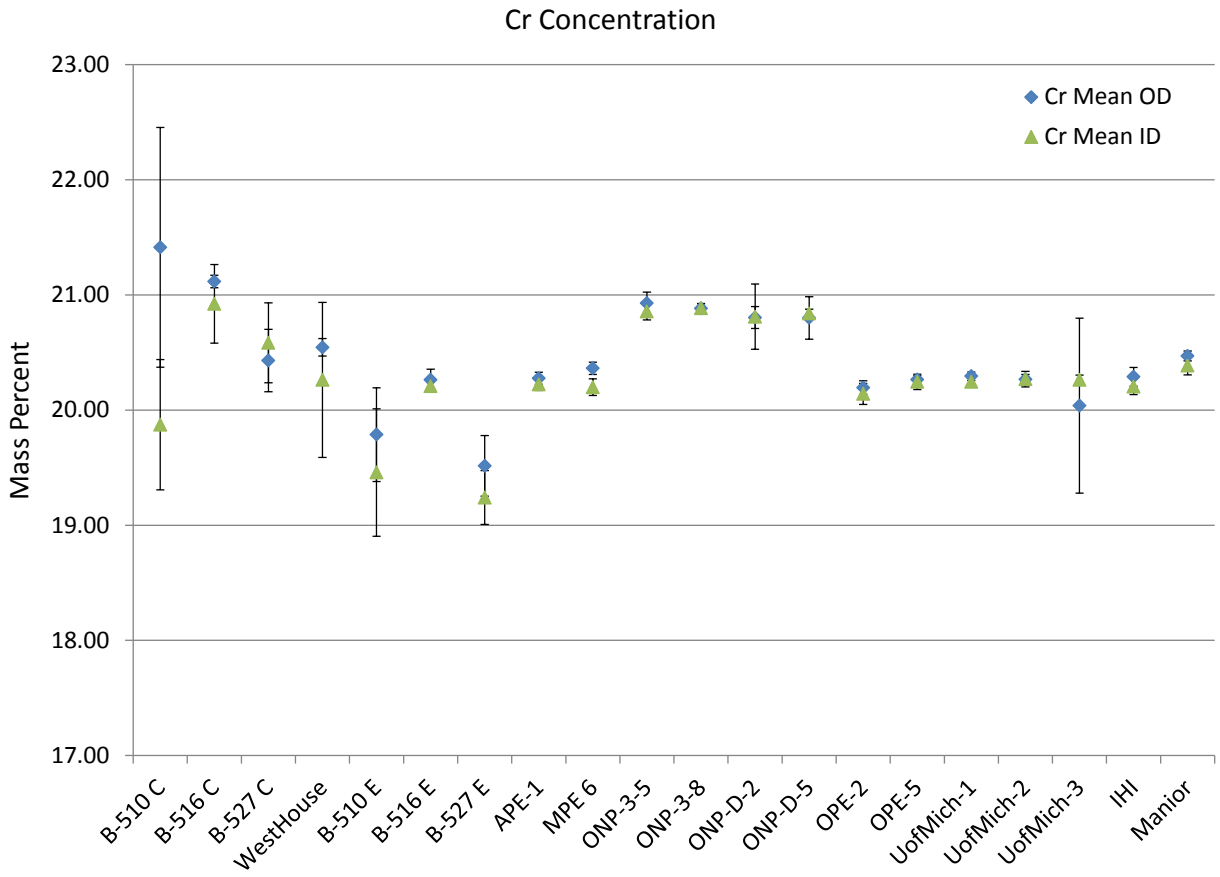

Figure C.2. Mean Cr Concentration Obtained from XRF Measurements are Plotted for OD and ID Surfaces of Each Specimen. Error bars represent one standard deviation.

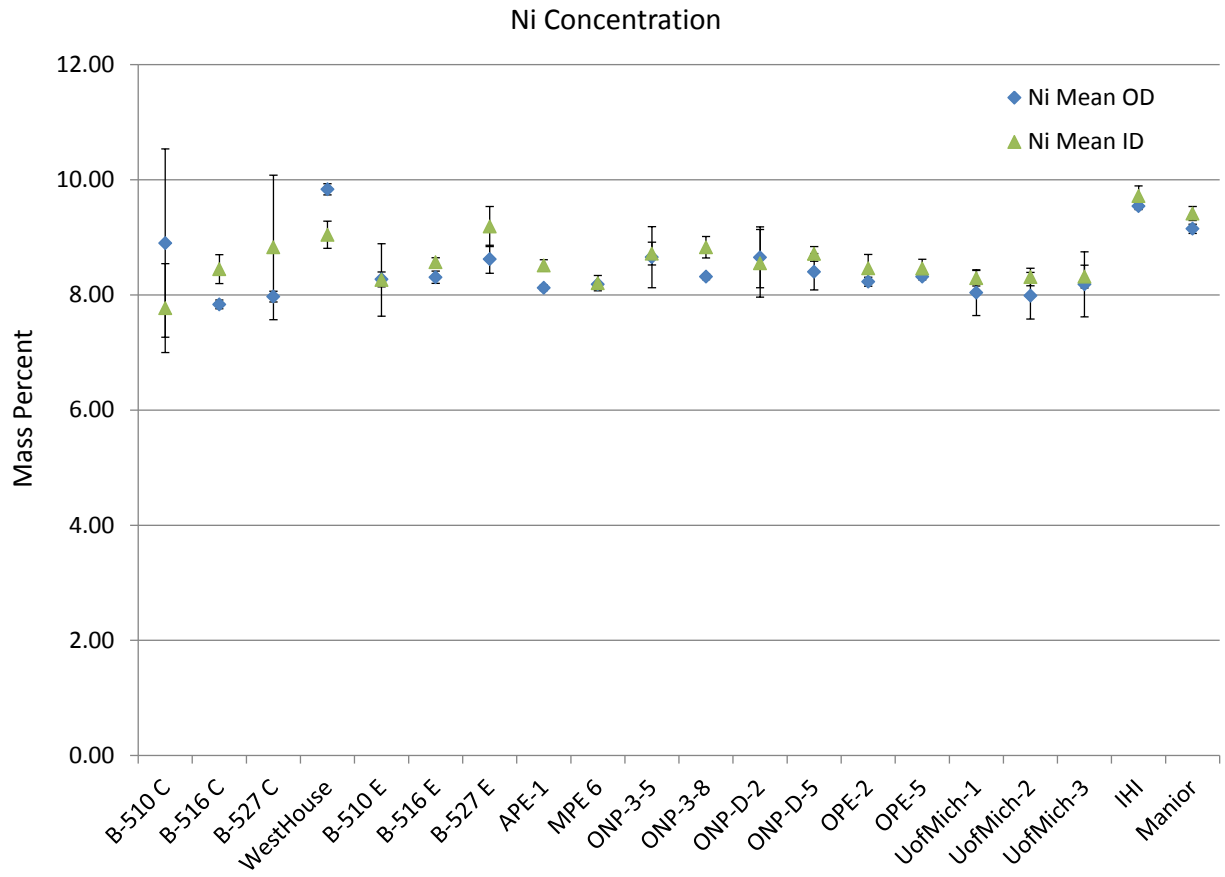

Figure C.3. Mean Ni Concentration Obtained from XRF Measurements are Plotted for OD and ID Surfaces of Each Specimen. Error bars represent one standard deviation.

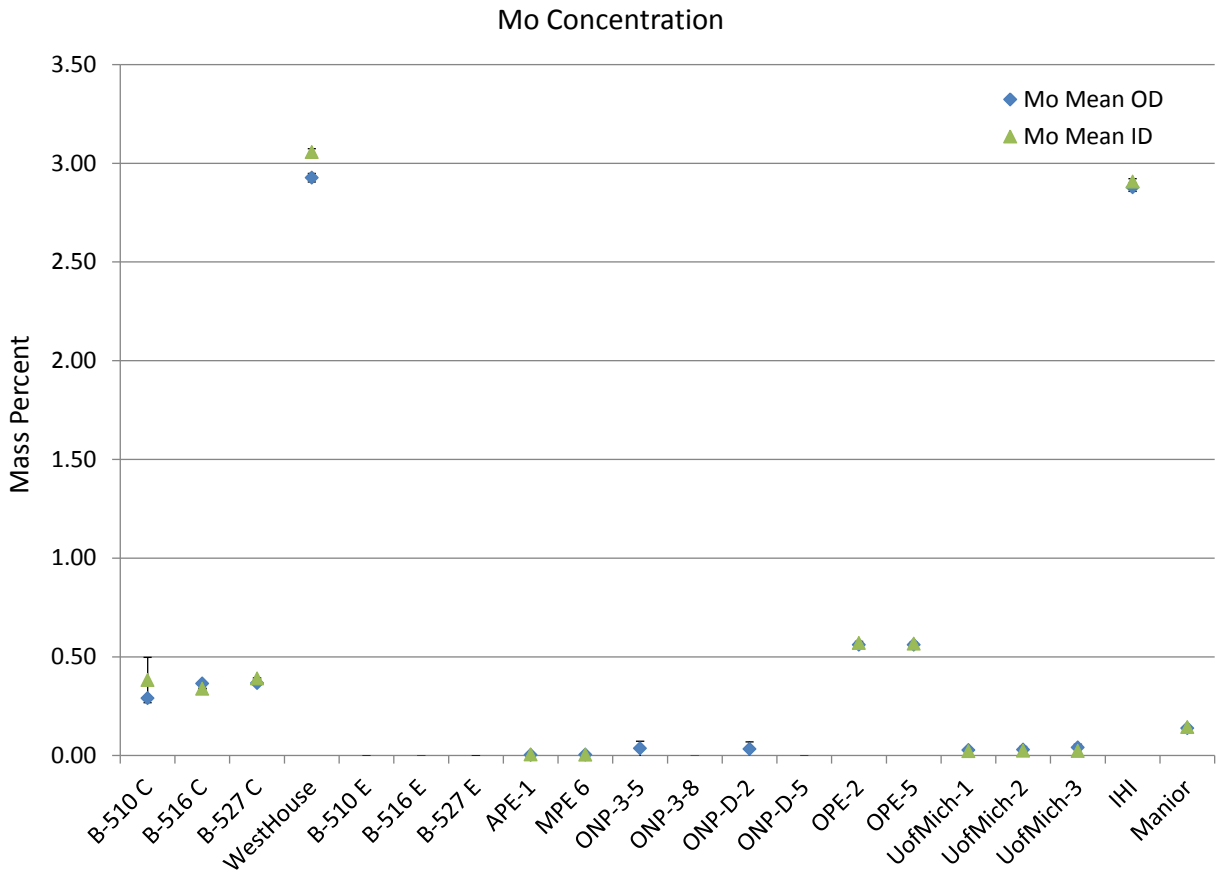

Figure C.4. Mean Mo Concentration Obtained from XRF Measurements are Plotted for OD and ID Surfaces of Each Specimen. Error bars represent one standard deviation.

Pacific Northwest
NATIONAL LABORATORY

Proudly Operated by **Battelle** *Since 1965*

902 Battelle Boulevard
P.O. Box 999
Richland, WA 99352
1-888-375-PNNL (7665)

www.pnnl.gov

Prepared for the U.S. Nuclear Regulatory Commission
under a Related Services Agreement with the U.S. Department of Energy
CONTRACT DE-AC05-76RL01830

U.S. DEPARTMENT OF
ENERGY